



---

SOME STUDIES ON MATHEMATICAL MORPHOLOGY IN  
REMOTELY SENSED DATA ANALYSIS

---

A thesis submitted to Indian Statistical Institute  
in partial fulfilment of the thesis requirements for the degree of  
**Doctor of Philosophy in Computer Science**

*Author:* Geetika Barman

Systems Science and Informatics Unit  
Indian Statistical Institute  
Bangalore -560059

*Supervisor:* Prof. B. S. Daya Sagar

Systems Science and Informatics Unit  
Indian Statistical Institute  
Bangalore -560059

July, 2023



This thesis is lovingly dedicated to my parents, *Late Lohit Barman* and *Mrs Deepti Barman*, my first teachers and torchbearers, who illuminated my path with their wisdom and love.



## *Acknowledgments*

My thesis has become a reality with the kind support and help of many individuals. I want to express my sincere appreciation and admiration to everyone who has helped me tremendously throughout my PhD work.

I would like to express my profound gratitude to my PhD supervisor **Prof. B.S. Daya Sagar** for his unwavering guidance, patience, and support throughout the course of this research. Your insightful feedback pushed me to sharpen my thinking and brought my work to a higher level. I also want to express my gratitude to my colleagues **Sampreeti Soor, Athira, Aditya Challa, and Sravan Danda**, and for the enormously helpful discussions we had over the years.

I am thankful to **CCSD faculty members** for enlightening me with the knowledge that I have gained during my coursework. I would also like to thank all the **members of CCSD-RFAC and CCSD PhD/DSc committees** for providing me continuous support and suggestions during my PhD.

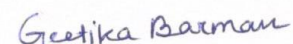
I am obliged to **Indian Statistical Institute** for providing **fellowship** to pursue my PhD.

I am blessed with a circle of incredibly supportive friends, who have been my lifeline through this process. Their unwavering belief in me, constant encouragement, and shared moments of levity have been fundamental in keeping my motivation high. I could not have navigated the challenges of this journey without you.

I extend my heartfelt gratitude to my family, my mother, my siblings, and my in-laws, for your unfailing love, understanding, and encouragement when it was most needed. Your faith in me has been a constant source of strength.

Finally, a special thanks to my spouse **Abhijit** for his unwavering faith in me, his sacrifices, and his love and companionship that carried me through this journey.

This thesis is a testament not just to my efforts, but also to the collective encouragement, support, and belief of all these wonderful people around me.



Geetika Barman



## **Abstract**

The application of Mathematical Morphology (MM) techniques has proven to be beneficial in the extraction of shape-based and texture-based features during remote sensing image analysis. The characteristics of these techniques, such as non-linear adaptability and comprehensive lattice structure, make them useful for contextual spatial feature analysis. Despite the advancements, there are still persistent challenges, including the curse of dimensionality, maintaining spatial correlation, and the adaptability of morphological operators in higher dimensions. The focus of this thesis is to explore the potential of MM-based methods to analyse spatial features in addressing these challenges, specifically in the context of spatial-contextual feature analysis of hyperspectral images and Digital Elevation Models. This thesis explores the power of morphological distance in capturing spatial relationships and proposes a modified definition called "Dilation Distance" to address the "Dimensionality Curse" in hyperspectral images. By employing dilation-based distances, spatially separated objects can be identified, reducing redundancy and enhancing efficiency. Experimental trials demonstrate the superiority of the proposed approach. Additionally, the thesis introduces a new approach

using morphological interpolation for terrain surface interpolation, preserving geometric structure while providing a smooth surface. The extension of conventional univariate morphological tools to hyperspectral images in a multivariate way is also explored, ensuring the concurrent application of operators while preserving the multivariate nature of the data. To achieve that a vector ordering strategy is proposed. Overall, these techniques have a profound impact on the progress of mathematical morphology in remotely sensed image analysis, offering valuable insights.



## List of Publications

- A. Challa, G. Barman, S. Danda and B. S. D. Sagar, "Band Selection Using Dilation Distances", in *IEEE Geoscience and Remote Sensing Letters*, vol. 19, pp. 1-5, 2022, doi:10.1109/LGRS.2021.3057117.
- G. Barman, B. S. D. Sagar, "Generation of High Spatial Resolution Terrestrial Surface from Low Spatial Resolution Elevation Contour Maps via Hierarchical Computation of Median Elevation Regions" in *IEEE Transactions on Geoscience and Remote Sensing*, vol. 61, pp. 1-11, 2023, Art no. 4508811, doi: 10.1109/TGRS.2023.3335120.
- G. Barman, A. Kakati, S. L. Lim and B. S. Daya Sagar, "Interpolation of Subsurface Isopach Maps Using Mathematical Morphology," *OCEANS 2022 - Chennai*, 2022, pp. 1-5, doi:10.1109/OCEANSCennai45887.2022.9775480.
- G. Barman and B. S. Daya Sagar, "A New Approach to Compute Vector Based Morphological Features for Classification of Hyperspectral Image," 2023 *IEEE India Geoscience and Remote Sensing Symposium (InGARSS)*, Bangalore, India, 2023, pp. 1-4,

doi:10.1109/InGARSS59135.2023.10490362.

# Contents

<b>List of Figures</b>	<b>v</b>
<b>List of Tables</b>	<b>ix</b>
<b>1 Introduction</b>	<b>1</b>
1.1 Remote Sensing Imaging . . . . .	2
1.1.1 Hyperspectral Image and Digital Eleva- tion Model . . . . .	3
1.2 Challenges in Processing Remotely Sensed Data	5
1.3 Mathematical Morphology in Processing Spatial Features . . . . .	10
1.4 Objective and Contribution . . . . .	14
1.5 Thesis outline . . . . .	18
<b>2 Theoretical Background</b>	<b>21</b>
2.1 Mathematical Morphological Operator . . . . .	21
2.1.1 Structuring Elements . . . . .	22

2.1.2	Binary Dilation and Erosion . . . . .	23
2.1.3	Grayscale Dilation and Erosion . . . . .	25
2.1.4	Opening and Closing . . . . .	27
2.1.5	Closing and Opening by Reconstruction	28
2.1.6	Morphological Profile . . . . .	30
2.2	Evaluation Metric Used . . . . .	31
2.2.1	Overall Classification Accuracy . . . . .	32
2.2.2	Average Classification Accuracy . . . . .	32
2.2.3	Kappa Coefficient . . . . .	33
2.2.4	Root Mean Square Error . . . . .	33
2.2.5	Mean Absolute Percentage Error . . . . .	34
2.2.6	Jaccard Similarity Coefficient . . . . .	35

### **3 Dilation Distance and Its Application in Hyper-spectral Image 37**

3.1	Introduction . . . . .	37
3.1.1	Band Selection Versus Feature Extraction	38
3.1.2	Why Dilation Distance? . . . . .	39
3.2	Review Of Terminology . . . . .	42
3.3	Dilation Distance . . . . .	46
3.4	Complexity Analysis . . . . .	49

3.4.1	Selection of a Subset of Bands Using Spectral Clustering . . . . .	50
3.5	Experimental Result . . . . .	52
3.5.1	Dataset Used . . . . .	52
3.5.2	Result Analysis . . . . .	53
3.6	Conclusion and Future Work . . . . .	60
<b>4</b>	<b>Terrain Surface Generation via Hierarchical Median Set Based Interpolation</b>	<b>63</b>
4.1	Introduction . . . . .	63
4.2	Some Background Concept . . . . .	69
4.2.1	Contour Lines . . . . .	69
4.2.2	Hausdorff Erosion Distance and Hausdorff Dilation Distance . . . . .	70
4.2.3	Median Set Computation . . . . .	72
4.2.4	Threshold Decomposition . . . . .	74
4.3	Methodology . . . . .	75
4.3.1	Intermediate Contour Generation . . . . .	77
4.3.2	Extraction of Threshold Elevation Regions . . . . .	80
4.3.3	Spatial Relationship between TERs . . . . .	86

4.3.4	Intermediate Contour Computation using Median Set . . . . .	88
4.3.5	Complexity Analysis . . . . .	93
4.4	Results and Discussion . . . . .	94
4.4.1	Case study on Mt. Washington, NH . . . . .	95
4.4.2	Validation of the Method . . . . .	98
4.5	Conclusion . . . . .	109
<b>5</b>	<b>Adapting Morphological Operators for Multivariate Data Processing</b>	<b>113</b>
5.1	Introduction . . . . .	113
5.2	Mathematical Morphology in Multivariate Data	116
5.3	Related Work . . . . .	118
5.4	Proposed Vector Ordering . . . . .	122
5.5	Result and Analysis . . . . .	131
5.6	Conclusion . . . . .	143
<b>6</b>	<b>Conclusions and Future Work</b>	<b>145</b>

# List of Figures

1-1	A generic example of hyperspectral image . . . .	4
2-1	Example of commonly used structuring element, the left image is disk SE of radius 1 with its origin and the right image is 3x3 square SE with its given origin. . . . .	23
2-2	Example of binary dilation and erosion with input image on left and output image at the right-most side, the image in middle is disk SE of radius 1. . . . .	25
2-3	Illustrating dilation operation on grayscale Image	27
3-1	Illustration of the band selection using dilation distances on synthetic data . . . . .	40
3-2	Illustration of how dilation distance captures the spatial distance over co-relation . . . . .	46

3-3	Illustration of the definition of dilation distance for different levels . . . . .	49
3-4	False color composite and ground truth of Pavia University . . . . .	53
3-5	False color composite and ground truth of Indian Pine Dataset . . . . .	54
3-6	Illustration of band selection by dilation distance using Indian pine and Pavia dataset . . . . .	56
3-7	Accuracy versus the number of bands . . . . .	57
4-1	A Sequential Representation of the Methodology to generate intermediate contours from successive contours from a contour map. . . . .	80
4-2	Example of nested contours and their corresponding TERs . . . . .	85
4-3	Intermediate contour generation example in toy data . . . . .	89
4-4	Surface generated for both zone using the proposed method . . . . .	98
4-5	Error analysis of the method using RMSE, MAPE and Jaccard Index . . . . .	101



4-6	(a) Set of test contours of contour interval 40 meters obtained from Zone A; (b) overlapping of interpolated 1st level intermediate contours (blue color) and original contours (red color) . . .	102
4-7	Error analysis of the method using RMSE, MAPE and Jaccard Index . . . . .	105
5-1	Plot of band priority versus average intensity for each class . . . . .	134
5-2	Comparative effects of dilation and erosion operations on multi-channel and mono channel data	138
5-3	Classification accuracy vs. the number of opening and closing cycles (as discussed in Eq.2.14) used to compute MP. . . . .	139
5-4	Comparative analysis of the classification map obtained from SVM classification . . . . .	142



# List of Tables

3.1	Evaluation Using SVM for 30 Bands. Note: OCA is considered *** indicated the results are not available. . . . .	59
4.1	Hausdorff Distance values for "Zone A" and "Zone B" . . . . .	106
4.2	Result of Applying Different Methods . . . . .	108
5.1	Classification metrics for proposed method . . . . .	140
5.2	Comparative analysis of classification accuracy . . . . .	143



# Chapter 1

## Introduction

Remote sensing data analysis is crucial for understanding earth's surface dynamics [1]. Mathematical morphology enables spatial analysis, extracting features, reducing noise, detecting objects, and analyzing patterns. By applying morphological operators, such as erosion, dilation, opening, and closing, remote sensing data can be processed for land cover, urban growth, ecology, and environmental monitoring. This thesis explores mathematical morphology's applications in spatial analysis of remote sensing data, emphasizing two byproducts of remote sensing imaging systems namely hyperspectral image data [2] and Digital Elevation Models (DEMs) [3, 4]. It enhances our understanding of the spatial features of the earth's surface data.

## **1.1 Remote Sensing Imaging**

In the early 1960s, the term "remote sensing" was coined to describe the process of collecting and measuring data on objects and phenomena without physical contact. It involves using sensors on aircraft or satellites to measure electromagnetic energy emitted or scattered from the earth's surface. This energy exists across various wavelengths in the electromagnetic spectrum. The incident energy from the surface, originating from sources like the Sun, passes through the Earth's atmosphere and interacts with the surface by absorption, scattering, and reflection. The reflected and scattered components eventually reach the sensor after traveling back through the atmosphere. The sensor measures the radiance in different spectral components, focusing on specific bands of the electromagnetic spectrum [1, 5–9]. The measured data is converted into digital or analog format and transmitted to the earth's receiving stations for processing and error correction [10]. Digital image processing techniques are applied to extract information from digital images, while visual interpretation techniques are used for analog data. The interpreted data is then separated and transformed into various layers of thematic maps; additionally, tabular data are also

extracted from quantitative measures [11–13].

### 1.1.1 Hyperspectral Image and Digital Elevation Model

Hyperspectral Images (HSI) [14] and Digital Elevation Models (DEMs) [15] are vital derived products of remote sensing data that offer valuable insight into the surface of the earth. HSI has revolutionized remote sensing by capturing a wide range of spectral bands across the electromagnetic spectrum, allowing for detailed analysis and interpretation of the earth's surface. On the other hand, DEMs represent the topography and elevation of the terrain, enabling a three-dimensional understanding of the earth's surface.

HSI data consists of numerous narrow and contiguous spectral bands, allowing for precise identification and characterization of objects based on their unique spectral signatures. With its ability to acquire hundreds of spectral bands, HSI provides an unprecedented level of spectral detail. This abundance of spectral information enables the identification and characterization of materials based on their unique spectral signatures, which leads to applications in environmental monitoring, land cover classification, mineral exploration, agriculture, and urban

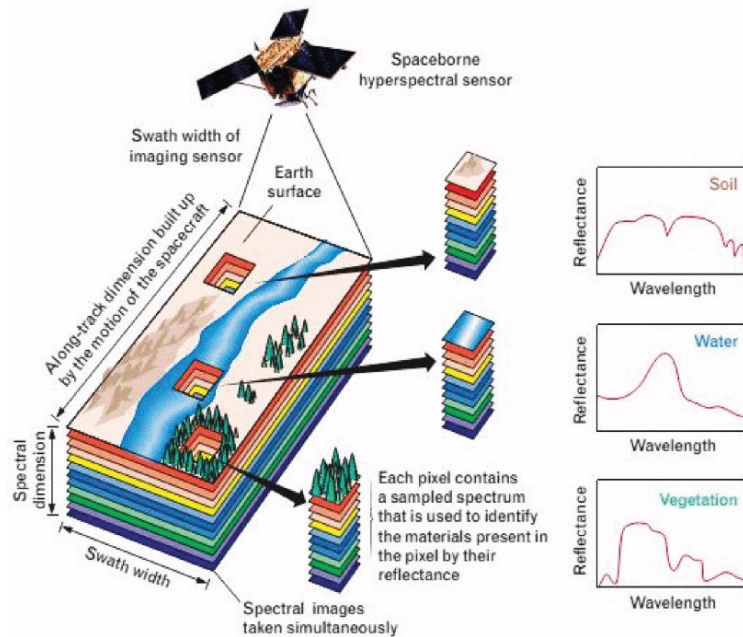


Figure 1-1: An example hyperspectral image where a generic scheme of HSI mapping of soil, vegetation, and water is shown. Soil, water, and vegetation have different spectral signatures captured at different wavelengths [16]

planning. Fig.1-1 is shown as an example hyperspectral image where a generic scheme of HSI mapping of soil, vegetation, and water is shown. Soil, water, and vegetation have different spectral signatures captured at different wavelengths. The unique spectrum is shown for a single pixel in Fig.1-1.

DEMs, on the other hand, provide crucial information about the terrain, offering a detailed representation of the earth's surface elevation [15, 17]. DEMs play a pivotal role in geospatial analysis, hydrological modeling [18], and landform characterization [19]. They enable the visualization of topographic



features [15] such as mountains, valleys, rivers, and slopes. This elevation information helps to assess flood risks, determine drainage patterns, analyze terrain ruggedness, and identify suitable locations for infrastructure development. However, hyperspectral images contain vast amounts of spectral information, necessitating advanced algorithms for data analysis and feature extraction [20, 21]. Handling high dimensionality and large datasets requires efficient storage and computational resources [22]. DEM processing involves managing extensive elevation data, performing terrain correction, and addressing data gaps. Challenges include data fusion, accuracy [23], and managing computational demands [24] etc. Satellite data processing entails addressing atmospheric effects, geometric distortions, and data calibration for reliable analysis. Integrating data from various sensors and platforms is crucial. Various challenges in processing this data at the digital image level will be discussed in the next section.

## **1.2 Challenges in Processing Remotely Sensed Data**

Conventionally, due to direct application to images, low-resolution remotely sensed images are processed using pixel-based ap-

proaches. In such approaches, only the spectral signatures of pixels are taken into account, not any spatial characteristics of the image. Although the analysis results were satisfactory, currently with an increase in geometrical resolution and spectral resolution, due to the high correlation between neighboring pixels, such approaches fail to perform better [25]. However, the spatial information captured in earth observation data greatly aids in the comprehension of earth data, as it characterizes the spectral signature in a complementary manner to the spectral signature of earth objects [25, 26] [26–30].

The study and analysis of spatial information can significantly contribute to understanding the scene in high-resolution remote sensing data. It is possible to code spatial information as relationships between adjacent pixels, spatial patterns (such as texture), spatial characteristics of regions (such as geometrical, morphological, and textural measures), structural relationships in objects, and relational links between scene elements. In short, the knowledge derived from the characteristics extracted from the spatial domain can be said to be spatial information [25, 27]. Although spectral analysis-based approaches are straightforward to apply in images, we cannot say the same

for the approaches that extract and exploit spatial information. The challenges and importance of retrieving spatial information from earth observation data are shown in [31, 32].

There are different ways to extract spatial information from remote sensing data depending on the objective and purpose of processing, and this information can then be further processed to help better understand the data. With a wide range of abstraction levels and semantic levels, spatial domain-related features are not limited and are not simple to extract. Such approaches where spatial information is incorporated with spectral information for a better understanding of the image is known as "spatial-contextual" [33, 34] processing, which indicates the relationship between the pixels in a neighborhood with a target pixel [35]. These spatio-contextual image classification methods can be categorized into three groups: texture extraction, Markov Random Fields (MRF) modeling, and image segmentation and object-based image analysis [33, 36, 37]

Applications of texture extraction in remote sensing image processing date back to the 1970s [38, 39], and several studies have shown that the inclusion of texture metrics can enhance understanding while reducing spectral confusion between spec-

trally similar classes [40]. Four categories can be made up of the most common texture extraction techniques: 1) structural, 2) statistical, 3) model-based, and 4) transform [41–43]. Through analyzing pre-defined primitives and the spatial configurations of these primitives, structural approaches [39] make an effort to examine image textures. Utilizing primitives and their placement guidelines, one can specify the texture of an image.

Another group of methods for extracting texture involves using models, such as fractal models [44], auto-regressive models [45], and MRF models [46]. Moreover, the transform methods, which include Fourier and Gabor transforms, as well as Wavelet transforms [47]. Wavelet transformations outperform Fourier and Gabor [47]. Wavelet transforms outperform Fourier and Gabor transforms because they operate at multiple spatial resolutions and offer a wide range of wavelet functions that can be chosen to enhance remote sensing image processing tasks. Texture information can be integrated into both the pre-processing (e.g., as an extra variable) and post-processing (e.g. image filtering) stages of image processing [48]. Numerous studies have demonstrated that incorporating texture information into remote sensing image classification can improve accuracy

and better discriminate between land cover types. According to Moser et al., [49], MRFs are capable of examining the global and local characteristics of a remote sensing image and quantifying the spatial auto-correlation among pixels using a rigorous mathematical approach. MRFs have thus been used to address a variety of issues with remote sensing image analysis, such as classification, change detection, sub-pixel analysis, and segmentation [50–52]. Kettig and Landgrebe [53] introduced an image segmentation application to remote sensing, and further refined the work with the development of the ECHO classifier. In the case of remote sensing image segmentation, algorithms have been devised to incorporate spatio-contextual information. These algorithms encompass region-growing methods [54, 55], watershed methods [56], and hierarchical algorithms [57]. By considering spatial relationships and context between image regions, these techniques aim to improve the accuracy and effectiveness of image analysis processes.

### **1.3 Mathematical Morphology in Processing Spatial Features**

In the mid-1960s, Mathematical Morphology (MM) emerged as a field of image analysis. From its inception, it encompassed both theoretical findings and investigations into the connections between geometrical textures and the physical properties of the objects being studied. This field originates from the exploration of binary porous media, such as sandstone. These media consist of two distinct phases: the matrix and the embedded pores. Matheron [58] and Serra [59,60] introduced a formalism in 1967 to analyze binary images, wherein the matrix represents the set of object points and the pores represent the complementary set. To extract or suppress specific structures within image objects, a structuring element is defined and carefully selected in terms of shape and size. This element is then applied across the image, acting as a probe. Morphological operations rely on set operations like union, intersection, complement, and translation, evaluating the compatibility of the structuring element with the image objects at various positions.

The evolution of Mathematical Morphology (MM) from its roots in binary image processing to its current status as a

versatile tool for handling complex image structures has been remarkable. Initially introduced by Matheron [58] and Serra [59, 60], the original MM framework focused on fundamental operations such as binary dilation and erosion, deeply rooted in the geometric measure theory of Minkowski and Hadwiger [61, 62]. However, with the increasing need to process grayscale images, the framework underwent significant extensions. The most notable generalization is the utilization of the complete lattice by Serra [63]. Sternberg extended mathematical morphology principles from two to three dimensions and introduced grayscale mathematical morphology [64]. Ronse [65] and Heijman [66] demonstrated that extending morphological operations to complete lattices is essential for mathematically applying these operators to grayscale images. For a detailed discussion, the reader can refer to [67, 68]. Also, the introduction of fuzzy set theory [69] led to the development of fuzzy MM [68, 70–74], which was subsequently extended to L-fuzzy MM [75], where  $L$  denotes an arbitrary complete lattice, further broadening the scope of grayscale MM. These studies have contributed foundational principles, including those based on complete lattices and fuzzy sets, offering a comprehensive un-

derstanding of morphological operations.

Destival [76] was among the early researchers who acknowledged the value of mathematical morphology in extracting objects with specific shapes, like roads, river networks, and village outlines. Another study [77] focused on the development of a directional morphological filter to reduce acquisition stripes in satellite images. In a separate work, Martel et. al. [78] demonstrated that mathematical morphology could serve as a viable alternative to harmonic analysis when determining certain factors. Characteristic features of functions defined on the earth's surface are explored in various studies. One example is the detection of gravity anomalies using directional morphological filters. In [79], binary morphological operations and polygon fill techniques are employed for land masking and coastline correction in AVHRR images. Another study [80] successfully extracted built-up areas on SPOT-P images by employing resampled morphological gradient, achieving accuracy comparable to manual photo interpretation. In [81], opening and closing operations are utilized to remove noise, and small ice floes, and to smoothen boundaries in Landsat TM Antarctic scenes, significantly improving the segmentation and classification of complex



scenes.

Infrared ocean images employ alternating sequential filters to extract closed circulation areas (vortices) [82, 82]. Aerial photographs differentiate tree species using granulometry with different structuring elements [83]. Landforms like domes and deflation areas are mapped from panchromatic SPOT images using morphological top-hat filters [83, 84]. In addition, morphological clustering in a feature space proves effective for satellite images, outperforming supervised methods [85, 86]. Further advancements include geodesic filtering and marker-controlled segmentation for multispectral images [87].

Morphological operators also have demonstrated their suitability for processing Digital Elevation Models (DEMs). The initial application focused on extracting catchment basins and watersheds [88] (also covered in [89] and [90] with a fast algorithm utilizing first-in-first-out queue data structures). Geodesic interpolation is introduced in [91] to generate DEMs from digitized elevation contour lines (further enhancements are discussed in [92] based on generalized geodesy principles [92]). Efficient methods for extracting drainage networks from DEMs using fast fill holes and lower complete transformations are elab-

orated in [93]. An overview of these applications can be found in [94, 95].

## **1.4 Objective and Contribution**

The literature indicates that as the resolution of data increases, it becomes crucial to incorporate spatial features to obtain a better understanding of the scene. Mathematical morphology (MM) has emerged as a powerful tool for extracting spatial features while preserving geometric information [59, 60, 96, 97]. In the field of remotely sensed image analysis, MM has been recognized for its potential in various applications, including image filtering, image segmentation, and image recognition, as identified by Soille and Pesaresi in their research [95].

This thesis focuses on three interrelated challenges, all converging to elevate the understanding of spatial relationships in remotely sensed data, with a special focus on spatial analysis of HSI and DEMs. Each problem contributes to the unified goal of enhancing spatial analysis methodologies through the use of mathematical morphology (MM) based methods. The first problem (Chapter 3), centers on the introduction and analysis of the property of MM grayscale operators to capture the spa-

tial relationships between two spatial fields, which leads to the proposal of the Dilation Distance method. It also showcases the utility of reducing the dimensionality of hyperspectral images, providing a methodical approach to understanding spatial features across different bands. Expanding the scope, our investigation extends to mathematical morphology-based interpolation techniques using binary MM operators (Chapter 4), specifically addressing ordered sets derived from topographic maps. Many times, the variable-specific information mapped from the specific bands of the high spatial resolution hyperspectral images needs to be draped on high-resolution DEMs. However, the DEMs of low spatial resolution exhibit aliasing effects, which in turn are not suitable for draping the variable-specific information mapped from remotely sensed satellite data such as multispectral and hyperspectral images. To fill that gap, we proposed and demonstrated the generation of fine-resolution contour-based DEMs from coarse-resolution DEMs. The proposed median-set-based interpolation technique demonstrates its efficacy in analyzing spatial relationships between ordered sets and in generating finer-resolution DEMs from available topographic maps. This contribution significantly advances our

ability to interpret and exploit spatial relationships among terrain elevation features using MM operators. The third problem (Chapter 5) responds to the demand for the applicability of MM-based methods in multiband images. To overcome the limitations of MM operations defined on 2D images, a vector ordering strategy is proposed. This strategy facilitates the definition of supremum and infimum for vector comparisons, leading to the introduction of multivariate MM operations. The objective is to extend MM operations directly to multiband images in a multivariate manner, addressing the evolving needs of remote sensing image analysis. With all these problems addressed in Chapters 3 to 5, this thesis offers a unified perspective and application of MM-based techniques on advancing spatial analysis in remotely sensed data. This thesis collectively contributes to a more comprehensive understanding of spatial relationships within the context of hyperspectral images and DEMs.

This thesis primarily focuses on exploring MM-based non-linear operator methods and analyzing the spatial features of remotely sensed data, with a particular emphasis on hyperspectral images and Digital Elevation Models (DEMs). The main objective of this thesis is to introduce a dilation-based distance

and discuss its properties. Additionally, it aims to demonstrate its application in capturing spatial distances across bands of multiband images, thereby reducing dimensionality. The thesis also investigates morphological-based interpolation techniques for ordered sets. It studies topographic maps as binary thresholded regions and explores the spatial relationship between two ordered sets through the use of Hausdorff distance. The proposed median-set-based interpolation technique performs well in the application of generating a Digital Elevation Model from a topographic map. Furthermore, the application of median set-based interpolation to DEMs can be considered to explore the spatial relationship among terrain elevation features. It is a significant contribution to this research. However, the MM operations are defined till now on 2D images by defining minimum and maximum in local neighborhoods. The demand for the applicability of MM-based methods in multiband images, such as HSI, motivates us to explore the MM operators directly on multiband images in a multivariate way. This leads to a proposal of a vector ordering strategy in this thesis to define supremum and infimum in comparing vectors, which in turn propose multivariate MM operations for HSI.

## 1.5 Thesis outline

This thesis is structured as six chapters. Chapters 3, 4, and 5 are contributing chapters of this thesis, whereas Chapters 1 and 2 discuss the introductory literature and background concepts of related theory.

- **Chapter 1:** This chapter primarily provides an overview of the inspiration and motivation that drove the research conducted for this thesis, including a review of related work. It encapsulates the theoretical basis that underpins the proposed study's motivations.
- **Chapter 2:** This chapter offers comprehensive explanations of the terms and notations associated with initial Mathematical Morphological operators, along with some relevant methods employed in the processing of remote sensing imagery.
- **Chapter 3:** This chapter discusses the proposed mathematical morphological method, "Dilation Distance", and its application in hyperspectral image classification, specifically in experiments involving dimensionality reduction of hyperspectral image. This chapter is taken from the arti-

cle:

A. Challa, G. Barman, S. Danda, and B. S. D. Sagar, "Band Selection Using Dilation Distances," in *IEEE Geoscience and Remote Sensing Letters*, vol. 19, pp. 1-5, 2022, doi: 10.1109/LGRS.2021.3057117.

- **Chapter 4:** This chapter covers the utilization of mathematical morphological interpolation for spatial information extraction and enhancement of the resolution of the Digital Elevation Model, which is generated from topographic maps (contour maps). In this chapter, a median-set-based interpolation method is proposed for DEM generation from topographic maps. This chapter is taken from the articles:

G. Barman, A. Kakati, S. L. Lim, and B. S. Daya Sagar, "Interpolation of Subsurface Isopach Maps Using Mathematical Morphology," *OCEANS 2022 - Chennai*, 2022, pp. 1-5, doi: 10.1109/OCEANSCennai45887.2022.9775480.

G. Barman, B. S. D. Sagar, "Generation of High Spatial Resolution Terrestrial Surface from Low Spatial Resolution Elevation Contour Maps via Hierarchical Computation of

Median Elevation Regions," *IEEE Transactions on Geoscience and Remote Sensing*, vol. 61, pp. 1-11, 2023, Art no. 4508811, doi: 10.1109/TGRS.2023.3335120.

- **Chapter 5:** This chapter discusses the extension of the fundamental mathematical morphological operators, dilation and erosion, to higher dimensions in multiband images. It also covers their application in hyperspectral image classification. Here, a vector ordering strategy is defined to use multivariate MM operators on HSI. This chapter is taken from the article:

G. Barman and B. S. Daya Sagar, "A New Approach to Compute Vector Based Morphological Features for Classification of Hyperspectral Image," 2023 *IEEE India Geoscience and Remote Sensing Symposium (InGARSS)*, Bangalore, India, 2023, pp. 1-4, doi: 10.1109/InGARSS59135.2023.10490362.

- **Chapter 6:** This chapter summarizes the contribution of the thesis and provides a concluding remark and future work.



# Chapter 2

## Theoretical Background

This chapter will revisit some fundamental MM operators and some image analysis concepts that are necessary for the proposed frameworks in this thesis.

### 2.1 Mathematical Morphological Operator

In this section, we will review the essential mathematical morphological concepts required for the suggested framework. Since we are working with digital images, in this thesis we restrict our attention to digital framework only. The morphological operators are also defined in discrete space. The basic MM operators, namely dilation and erosion, will be discussed in the context of both binary images and grayscale images. For a more in-depth theoretical understanding, readers can further go through ref-

erences [3, 60, 66, 95, 97–99].

### 2.1.1 Structuring Elements

Unlike point image transformations, mathematical morphology (MM) operations involve neighborhood image transformations. In these operations, the value of an output pixel is a function of its neighboring pixel's values. The neighborhood itself is determined by a separate set of pixels referred to as the Structuring Element (SE) with a defined origin [60, 96, 99]. The structural element (SE) serves as a tool to analyze the morphology of an object. Typically, the SE has a basic geometric shape such as a disk or square, and its size, like a 3x3 window, is adjusted based on the object's geometry being processed. For grayscale image transformation, a SE can take any value. SE is referred to as a "Flat SE" if it consists of a collection of pixels without any assigned values; otherwise, if it takes any integer value, it is referred to as a "Non-Flat SE." However, in the context of the thesis, only "Flat SE" is discussed. In mathematical terms, for a set  $E \subset \mathbb{R}^2$  or  $E \subset \mathbb{Z}^2$ , a flat SE is defined as follows:

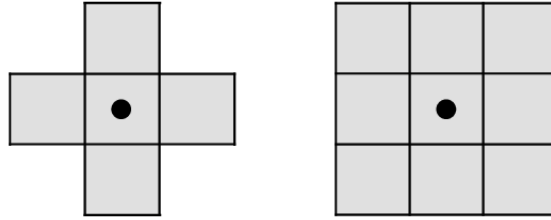


Figure 2-1: Example of commonly used structuring element, the left image is disk SE of radius 1 with its origin and the right image is 3x3 square SE with its given origin.

$$f(x) = \begin{cases} 0, & x \in E \\ -\infty, & x \notin E \end{cases}$$

Throughout this thesis, we shall only consider SE as a flat SE and a disk of radius 1. If it is used as other shape and size other than a disk of radius 1, it is mentioned in that specific chapter. Two commonly used SEs are shown in Fig.2-1. Even if the example is shown with the same origin point, the origin may be any pixel.

### 2.1.2 Binary Dilation and Erosion

In Mathematical Morphology, a binary image can be defined as a mapping function  $f : E \rightarrow \{0, 1\}$ , where  $E$  represents the "Image plane" or the domain in which the image is defined. This domain, also referred to as the "Definition Domain", is typically a subset of either the discrete space  $\mathbb{Z}^2$  or the contin-

uous space  $\mathbb{R}^2$ .

The dilation of a set  $Y$  by SE  $B$  is denoted by  $\delta_B(Y)$  and is defined as the locus of points  $y$  such that  $B$  hits  $Y$  when its origin coincides with  $y$  [66, 96, 99]:

$$\delta_B(Y) = Y \oplus B = \left\{ y \mid \hat{B}_y \cap Y \neq \phi \right\} = \bigcup_{b \in B} Y_b \quad (2.1)$$

where  $Y_b$  is the translation of  $Y$  along the vector  $b$  and  $\hat{B}$  is the transposition of  $B$  with respect to its origin, that is,  $\hat{B} = \{b \mid -b \in B\}$ .

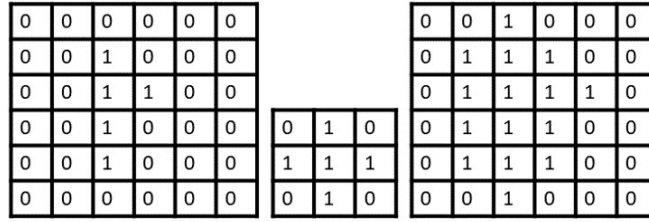
Similar to dilation, erosion of set  $Y$  by SE  $B$  is denoted by  $\varepsilon_B(Y)$  and is defined as the locus of points  $y$ , such that  $B$  is included in  $Y$ , when its origin is placed at  $y$  [60, 66, 96, 99]:

$$\varepsilon_B(Y) = Y \ominus B = \{y \mid B_y \subseteq Y\} = \bigcap_{b \in B} Y_{-b} \quad (2.2)$$

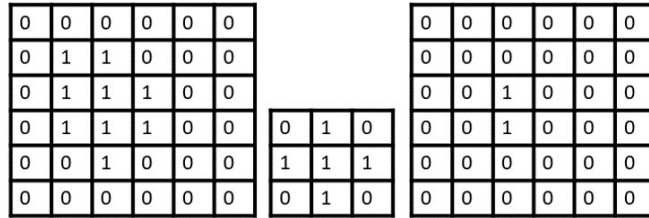
where  $B_y$  is the translation of  $B$  by vector  $y$  and  $Y_{-b}$  denotes the translation of  $Y$  by  $-b$ .

If SE is symmetric to its origin, then both erosion and dilation are equivalent to Minkowski subtraction and Minkowski addition respectively. An example of binary dilation and binary

erosion is shown in Fig.2-2.



(a) Binary Dilation



(b) Binary Erosion

Figure 2-2: Example of binary dilation and erosion with input image on left and output image at the rightmost side, the image in middle is disk SE of radius 1.

### 2.1.3 Grayscale Dilation and Erosion

Similar to binary morphological operations, in grayscale morphological transformations, images are considered as a mapping function  $f : E \rightarrow \bar{\mathbb{R}}$ , where  $\bar{\mathbb{R}}$  is  $\mathbb{R} \cup \{+\infty, -\infty\}$  or  $f : E \rightarrow \bar{\mathbb{Z}}$ , where  $\bar{\mathbb{Z}}$  is  $\mathbb{Z} \cup \{+\infty, -\infty\}$ . The dilation operator on a grayscale image  $f(x)$  by a structuring element  $g(x)$  is defined as [66, 96, 99]:

$$\delta_g(f)(x) = (f \oplus g)(x) = \sup_{y \in E} \{f(y) + g(x - y)\} \quad (2.3)$$

Similarly, the erosion operator on grayscale image  $f(x)$  by SE  $g(x)$  is defined as :

$$\varepsilon_g(f)(x) = (f \ominus g)(x) = \inf_{y \in E} \{f(y) - g(y - x)\} \quad (2.4)$$

where  $x$  and  $y$  are the pixel coordinates of the input image and SE respectively,  $g$  is the structuring element for a grayscale image and also can be defined as a structuring function defined on  $E$  and  $sup$  denotes supremum and  $inf$  denotes infimum. If  $g$  can take any values, it is referred to as a non-flat structuring element. If  $g$  takes values only in  $\{0, -\infty\}$  and has the value 0 on a finite subset, this is referred to as a flat structuring element. Therefore, flat structuring functions are functions of  $g(x)$  in the form:

$$g(x) = \begin{cases} 0, & x \in B \\ -\infty, & x \notin B \end{cases}$$

In this case, the definition of dilation by structuring element  $B$  can be written as:

$$\delta_g(f)(x) = \sup_{y \in \hat{B}_x} f(y) (= f \oplus B) \quad (2.5)$$

$B$  denotes the set where  $g$  takes the value 0 and  $\hat{B}_x =$

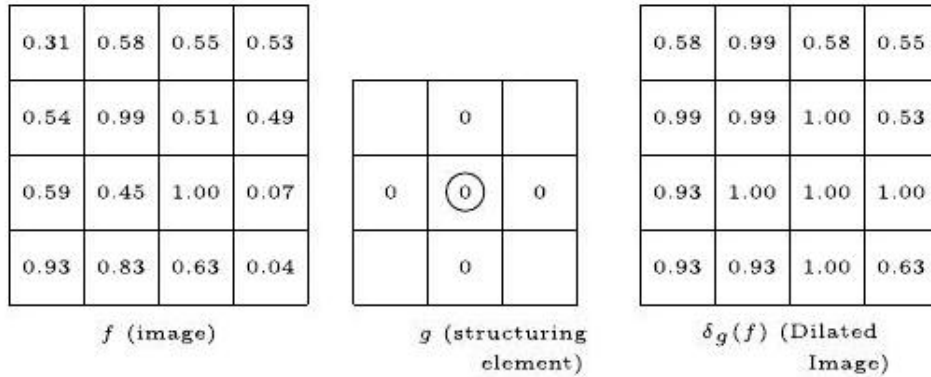


Figure 2-3: Illustrating grayscale dilation. On the left, we have a grayscale image. A flat structuring element is shown in the center. Pixels with 0 value are shown and all other pixels have a value  $\infty$ . The center is indicated with a circle around the value. The dilated image is obtained by placing the center of the structuring element at each position and taking the maximum. The final answer is shown in the right image.

$\{x - b | b \in B\}$ . The dilation is written as  $f \oplus B$  for this flat structuring element. A simple illustration is shown in Fig.2-3.

Similarly, the grayscale erosion on  $f(x)$  by structuring element  $B$  can be defined as:

$$\varepsilon_g(f)(x) = \inf_{y \in B_x} f(y) (= f \ominus B) \tag{2.6}$$

### 2.1.4 Opening and Closing

The sequential operation of erosion followed by dilation and dilation followed by erosion is known as morphological opening and closing, respectively. The morphological opening of an image, denoted by  $f$  using a structuring element  $B$ , is charac-

terized as the erosion of  $f$  using  $B$ , succeeded by the dilation of the eroded output with  $B$ . Here,  $B$  represents the structuring element. The morphological opening ( $\gamma_B(f)$ ) can be defined as:

$$\gamma_B(f) = \delta_B[\varepsilon(f)] \quad (2.7)$$

On the other hand, the morphological closing of  $f$  by  $B$  is defined as the dilation of  $f$  followed by the erosion of  $f$  by  $B$ . It is written as:

$$\Phi_B(f) = \varepsilon_B[\delta(f)] \quad (2.8)$$

### 2.1.5 Closing and Opening by Reconstruction

Morphological opening and closing operators [60] can profoundly impact images, particularly when the structuring element (SE) is large compared to the image structures. These operators can distort or entirely erase geometrical attributes of structures, which is disadvantageous when needing to extract object details post-filtering. Geodesic reconstruction-based morphological operators [59, 60] can adeptly manage images, resolving these issues by either removing or preserving image components based on their interaction with the structuring element (SE). If an image component is larger than the SE, it remains



unchanged; otherwise, it's merged with a brighter or darker neighboring region, depending on whether a closing or opening operation is applied. An opening by reconstruction of image  $f$  is performed in two separate phases and defined as [100]:

$$\gamma_R^\nu(f) = R_f^\delta[\varepsilon^{(\nu)}(f)] \quad (2.9)$$

where the first phase is  $\varepsilon^{(\nu)}$ , that is, the erosion of  $f$ , with SE of size  $\nu$ , indicating the size of the opening. It creates the marker image for the reconstruction operation. The second phase involves performing a reconstruction by dilation, denoted as  $R_f^\delta(\cdot)$ , of the marker image using the reference mask  $f$ . This operation is an iterative process that applies geodesic dilation (defined as the infimum of the elementary dilation and the mask image) on the marker image until idempotence is achieved (the idempotence condition is:  $\delta_f^n = \delta_f^{n+1}$ ):

$$R_f^\delta(\cdot) = \delta_f^n(\cdot) = \delta_f^1 \cdot \delta_f^1 \cdot \delta_f^1 \cdots \delta_f^1(\cdot) \quad (\text{n times}) \quad (2.10)$$

Similarly, closing by reconstruction  $\Phi_R^\nu(f)$  on image  $f$  is defined as the reconstruction by erosion of  $f$  from the dilation of

$f$  using a structuring element of size  $\nu$ :

$$\Phi_R^\nu(f) = R_f^\varepsilon[\delta^{(\nu)}(f)] \quad (2.11)$$

### 2.1.6 Morphological Profile

Morphological profiles were first proposed by Pesaresi and Benediktsson in their work [101], where it is delineated as a sequence of anti-granulometry followed by granulometry. These are executed by closing and opening by reconstruction transformations, respectively. The term "anti-granulometry" is denoted as closing profile  $\Pi_\Phi$ , while "granulometry" is referred to as opening profile  $\Pi_\gamma$ . The morphological opening  $n$  profile of an image  $f$  is a sequence of  $n$  openings applied to the original image  $f$  using a structuring element (SE) of size  $\alpha$ . It is defined as:

$$\Pi_\gamma(f) = \{\Pi_{\gamma\alpha}(f) : \gamma_R^\alpha(f), \alpha = 0, 1, \dots, n\} \quad (2.12)$$

Thus, morphological closing profile  $\Pi_\Phi(f)$  is defined as:

$$\Pi_\Phi(f) = \{\Pi_{\Phi\alpha}(f) : \Phi_R^\alpha(f), \alpha = 0, 1, \dots, n\} \quad (2.13)$$

Combining these, both closing and opening profiles of size  $n$ , morphological profile (MP) is obtained. The resulting MP is of

size  $2n - 1$ , because when  $\alpha = 0$  the opening and closing profiles are equal to the original image and thus they are considered only once. So, a morphological profile (MP) is defined as:

$$MP(f) = \begin{cases} \Pi_{\gamma\alpha}(f) & \text{for } \alpha = (n - 1 + \nu), \quad \forall \alpha \in [1, n] \\ \Pi_{\Phi\alpha}(f) & \text{for } \alpha = (\nu - n - 1), \quad \forall \alpha \in [n + 1, 2n + 1] \end{cases} \quad (2.14)$$

All these definitions and concepts are explained in detail in [100].

## 2.2 Evaluation Metric Used

Evaluation metrics are used to analyze proposed methods for remote sensing data, specifically hyperspectral images and digital elevation models (DEMs). The evaluation metrics help quantify the performance and effectiveness of the proposed methods across various datasets in this domain. This section provides details about the evaluation metrics used throughout the work.

### 2.2.1 Overall Classification Accuracy

Overall classification accuracy, in the context of multi-class classification, is a performance metric represented by the ratio of the number of correctly classified instances to the total number of instances:

$$\text{Accuracy} = (\text{Number of correctly classified instances}) / (\text{Total number of instances})$$

This formula quantifies the model's ability [102] to predict the correct class labels across all the classes present in the dataset. It provides a numerical measure of the model's overall predictive accuracy, where a higher accuracy value indicates a better-performing model [103] in correctly assigning class labels to instances.

### 2.2.2 Average Classification Accuracy

The average classification accuracy (ACA) is a metric used to evaluate the performance of a classification model. It calculates the average accuracy across all classes by dividing the sum of individual class accuracies by the total number of classes. ACA provides an overall measure of the model's accuracy in classifying instances [104–106].

### 2.2.3 Kappa Coefficient

The Kappa coefficient ( $\kappa$ ) in terms of classification [107] can be mathematically defined as [108]:

$$\kappa = \frac{P_0 - P_e}{1 - P_e}$$

Where:

$P_0$  represents the observed agreement, which is the proportion of instances where the classifiers or observers agree on the assigned class labels,  $P_e$  represents the expected agreement by chance. It is calculated based on the distribution of class labels and the probabilities of random agreement. The Kappa coefficient provides a standardized measure to evaluate the agreement between classifiers or observers in classification tasks [109–111], considering both observed and expected agreement and is particularly useful when comparing multiple classifiers or assessing the consistency of observers in assigning class labels.

### 2.2.4 Root Mean Square Error

In the context of digital elevation models (DEMs), it is expected that the elevations corresponding to the original con-

tour lines should ideally have values that are either equal to (through interpolation) or very close to (through approximation) the contour labels. The accuracy of this correspondence can be quantified using the root mean square error (RMSE) measurement [112,113]. The RMSE can be defined as:

$$RMSE = \sqrt{\frac{1}{N} \sum_{i=1}^N (u_i - w_i)^2}$$

where  $u_i$  is the estimated elevation values of the DEM from its adjacent contour elevation values at test point  $i$ ;  $w_i$  is the actual elevation value of the DEM at the test point  $i$  and  $N$  is the total number of test points.

### 2.2.5 Mean Absolute Percentage Error

The Mean Absolute Percentage Error (MAPE) [114,115] is a metric that quantifies the average absolute percentage errors (APE) between actual and estimated elevation values at point  $i$  from its neighboring contour elevation values. Let's denote the actual elevation value at test points  $i$  as  $w_i$  and the corresponding predicted elevation values from its adjacent elevation values as  $u_i$ . The MAPE can be defined as:

$$MAPE = \frac{1}{N} \sum_{t=1}^N \left| \frac{w_i - u_i}{w_i} \right|$$

### 2.2.6 Jaccard Similarity Coefficient

The Jaccard similarity coefficient, also known as the Jaccard index, is a measure used to compute the similarity between two sets, typically used to compare shapes [116]. We can define the shape as the set of points contained within it. In the context of the proposed framework mentioned in Chapter 4, this measure is utilized to assess the similarity between predicted contours and actual contours, where the shape of contours can be defined by the set of pixels contained within it.

Let  $S_{IS}$  and  $S_{GT}$  represent the predicted shape and ground truth shape of the contours, respectively. the Jaccard similarity coefficient is calculated as the ratio of the intersection of these two sets to the union of the sets The Jaccard Similarity coefficient is computed as:

$$J = \frac{|S_{IS} \cap S_{GT}|}{|S_{IS} \cup S_{GT}|}$$

This coefficient quantifies the intersection of the interpolated shape and the ground truth shape divided by the union of the

two shapes.



# Chapter 3

## Dilation Distance and Its Application in Hyperspectral Image

### 3.1 Introduction

Advances in imaging techniques now allow us to capture spectral reflectance at several bands [117]. The finer resolution in spectral dimension allows us to capture different kinds of ground objects used across various application domains [118]. However, this also leads to capturing a large volume of data, leading to difficulties in processing. It is estimated that the hyperspectral infrared images by NASA capture 5.2Tb/day [119]. Also, adjacent bands have a high correlation leading to vast redundancy in representing the information. Hence, band selection and feature extraction methods are used for efficient storage, retrieval, and processing. Both these techniques are

part of larger dimensionality reduction methods.

### **3.1.1 Band Selection Versus Feature Extraction**

Both band selection and feature extraction methods reduce the dimensionality of data. Band selection proceeds by selecting a subset of features. However, feature extraction transforms the features into low dimensions using certain criteria such as principal component analysis (PCA) [120], and minimum noise fraction (MNF) [121]. These transforms can be either linear or nonlinear and are usually complex. Hence, the spectral meaning of the features is usually lost in the process. On the other hand, band selection preserves the spectral meaning of bands. This further helps in the interpretation of the results. Hence, band selection is preferred over feature extraction in several applications. This is evidenced by the vast amount of literature recently [122–126]. A recent comprehensive review can be found in [127]. In this chapter, we propose a novel band selection method using the techniques from mathematical morphology (MM) [58, 60, 63]. We use the grayscale dilation operator to define dilation distances (dd) and use this as a criterion for band selection.

### 3.1.2 Why Dilation Distance?

The problem of band selection asks— to identify the subset of bands such that all objects in the image can be distinguished. Now, the two main properties of such objects are:

1. The pixels within these objects have similar spectral signatures.
2. Different objects are spatially separated. Several existing methods exploit the first property to identify a subset of bands.

However, to our knowledge, there does not exist any band selection method, which explicitly exploits the second property mentioned above for band selection. Dilation distance, as proposed in this chapter, captures the spatial distance. Using this dilation distance for band selection will allow us to exploit the second property, as mentioned above. This is illustrated using a synthetic example (Fig.3-1). For comparison, we consider band selection using correlation-based distance and optimal neighborhood reconstruction (ONR) [128]. Here we consider an RGB image (left image in Fig.3-1) with three objects identified by the colors red, green, and blue. Using this image, we construct a

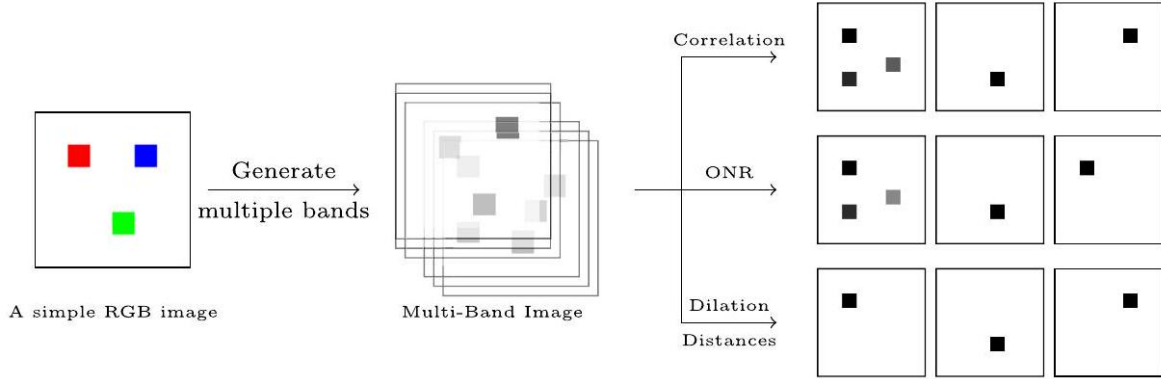


Figure 3-1: Figure illustrating the band selection using dilation distance. We start with an RGB image with three distinct objects represented by the three colors. We then generate several bands randomly to obtain a multiband image using Eq.3.1. The band selection procedures are applied to this multiband image. Observe that the dilation distance picks the bands such that each band represents a single object. On the other hand, the correlation-based band selection and ONR [128] do not exhibit this property.

multi-band image by considering several unit normed intensities in RGB denoted by  $\{a_0, a_1, a_2, \dots, a_{nz}\}$ , where  $nz$  denotes the number of bands. We produce several artificial bands by taking the dot product with different (random) unit normed vectors such as  $a_r$ , an example of which is given in Eq.3.1. Each of these dot products, with the RGB intensity of a pixel, will result in a grayscale image, which is taken to be a different band. For instance, the unit normed vector for  $r^{th}$  band may be denoted by:

$$a_r = \left( \frac{1}{\sqrt{6}}, \frac{2}{\sqrt{6}}, \frac{1}{\sqrt{6}} \right) \quad (3.1)$$

Accordingly, one can obtain the pixel values for the  $r^{th}$  band

by  $a_r$ . For example, for each unit normed vector  $a_r$ , calculate the dot product with the RGB values of each pixel. This will yield a new intensity value for each pixel, forming a new band. For a pixel with RGB values  $[R, G, B]$ , the intensity value of the pixel in the  $r^{th}$  band is:

$$\text{band}_r = R \cdot \frac{1}{\sqrt{6}} + G \cdot \frac{2}{\sqrt{6}} + B \cdot \frac{1}{\sqrt{6}}$$

$a_0, a_1, \dots, a_{nz}$  are random unit normed vectors similar to  $a_r$ . Several such bands are generated (middle image in Fig.3-1) using this approach. Using this multi-band image, we compare the top 3 bands selected by dilation distance (details of dilation distance are discussed in Section 3.3) with the ones obtained by correlation and ONR. The subset of bands is selected using the criterion

$$C(K) = \min_{b_i, b_j \in K} \text{distance}(b_i, b_j) \quad (3.2)$$

where  $K$  denotes the subset of bands and  $b_i, b_j$  are two separate bands within  $K$ , the distance can be either correlation, ONR, or dilation distance. The bands are obtained by maximizing the above criterion. These are shown on the right of the image in Fig.3-1. Observe that, as dictated by intuition, dilation dis-

tance picks the three bands that indicate each distinct object of red, green, and blue. However, bands selected using correlation distances and ONR do not have this property.

In this chapter, we formalize the notion of dilation-based distance and analyze their application to the band selection problem. In this chapter, we set up the notation and review the basic definitions required for the rest of the chapter. We define the dilation distance and explain the approach of band selection using dilation distance. Further, we compare the results on real hyperspectral data sets and illustrate several quantitative and qualitative results.

## **3.2 Review Of Terminology**

Let  $H$  denote the hyperspectral image with  $nz$  bands. Also, assume the size of each band is  $(nx, ny)$ . The bands of  $H$  are represented by  $\{f_1, f_2, \dots, f_{nz}\}$  where each  $f_i$  is a grayscale image. A grayscale image can be thought of as a function  $f : E \rightarrow \overline{\mathbb{R}}$ , where  $E$  denotes the domain of the image and  $\overline{\mathbb{R}}$  is  $\mathbb{R} \cup \{-\infty, \infty\}$  (completion of real space  $\mathbb{R}$ ).  $E$  is usually taken to be a subset of 2-D discrete space  $\mathbb{Z}^2$ , although it is common to use the 1-D discrete space  $\mathbb{Z}$  for illustrations. Based on the

definition given in Eq.2.3 and Eq.2.5 in Chapter 2, the dilation distance is defined as:

$$dd(f_i, f_j) = \min \{n \mid f_i \oplus nB \geq f_j\} \quad (3.3)$$

Recall that  $nB$  denotes a flat structuring element obtained by  $B \oplus B \oplus B \dots$  (n times)  $\dots \oplus B$ . This definition is adapted from the one mentioned in [129].  $B$  is considered to be the unit disk structuring element.

Remark: The term "dilation distance" (dd) used in Eq. 3.3 is not a traditional distance metric in the mathematical sense. Although we refer to it as distance, it is a dissimilarity measure related to the morphological dilation process. We use it to maintain consistency within the context. Also, the unit disk structuring element is conventionally used for dilation here. Using any other structuring element would distort the measure in a spatial direction, a property that is not recommended unless there is an explicit reason to do so. Hence, we consider only the unit disk structuring element.

The following properties of the dilation distance are noted:

1. It is possible that there does not exist any  $n$  such that  $f_i \oplus nB \geq f_j$ . In such cases,  $d(f_i, f_j)$  is taken to be  $\infty$ .

However, we have that if  $\sup \{f_i\} \geq \sup \{f_j\}$  and the domain is finite, then  $dd(f_i, f_j) < \infty$ , where  $\sup$  is denoted as supremum. Hence, for both  $dd(f_i, f_j)$  and  $dd(f_j, f_i)$  to be finite, we require  $\sup \{f_i\} = \sup \{f_j\}$ . In this work, we assume that the features (pixel intensity values of each band) are scaled to  $[0, 1]$  before computing the distance. Hence, we have  $\sup \{f_i\} = \sup \{f_j\}$ .

2. Observe that  $dd(f_i, f_i) = 0$  and  $dd(f_i, f_j) \geq 0$  for any  $i, j$ . However, it is not true that  $dd(f_i, f_j) = dd(f_j, f_i)$ , i.e., it is not symmetric. Also,  $dd(.,.)$  does not satisfy the triangle inequality in general. Hence, although we refer to  $dd$  as distance, it does not have the properties of the usual metric.
3. As we have already mentioned in the remark that  $dd$  is not a mathematical distance metric. So it does not follow the properties of the distance metric. One can define an equivalent dilation distance as  $\widehat{dd}$ , which is in terms of preserving its properties and also symmetric. Thus, the dilation distance  $\widehat{d}$

is defined as:



$$\widehat{dd}(f_i, f_j) = dd(f_i, f_j) + dd(f_j, f_i) \quad (3.4)$$

4. The most important property that is extensively used in this work is that dilation distance captures the spatial distance between bands. To illustrate this, we use 1-D images as shown in Fig.3-2. We consider the case of two pulse functions  $f_1, f_2$  as an example and compare them with correlation distances to observe the difference. In Case 1, the correlation distance is 0 and the dilation distance can be seen to be 3. However, when  $f_2$  is translated (in Case 2), the correlation is still 0, while the dilation distance increases to 6 and captures the difference. This intuitively shows that the dilation distance captures the spatial distance. Also, this implies that, when one selects the bands with the largest dilation distance, it implicitly selects the bands with the largest spatial distance between the objects the bands represent. This phenomenon is reflected in the toy example of Fig.3-1, where dilation distance-based band selection selects each band with a unique object.

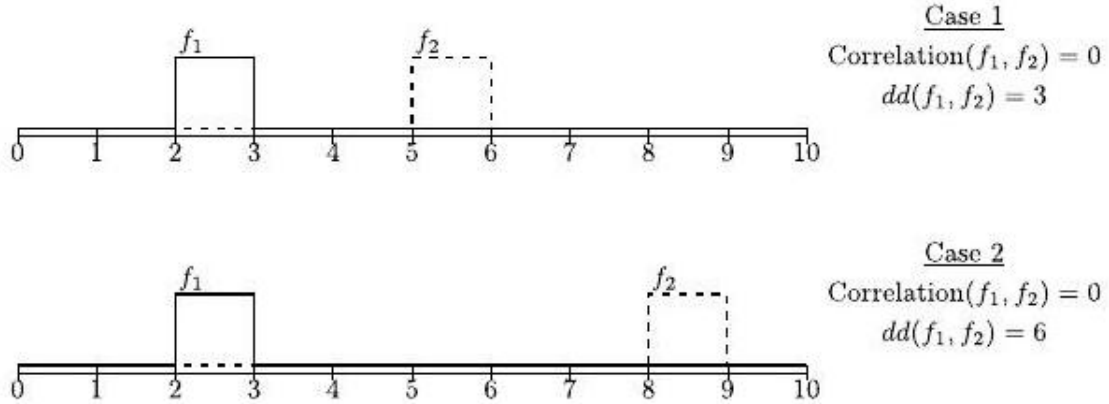


Figure 3-2: Figure illustrating that dilation distance captures the spatial distances. We consider pulse functions  $f_1$  and  $f_2$  as shown in the figure. In Case 1, we have that the dilation distance is 3 and the correlation is 0. When the pulse  $f_2$  is translated by 3 units, the correlation is still 0 while the dilation distance increases to 6. This intuitively shows why dilation distances can capture spatial distances. Thus, selecting the bands with the largest dilation distance will implicitly select the bands that have objects with the largest spatial distance between them.

### 3.3 Dilation Distance

While the dilation distance defined in Eq.3.3 captures the spatial distance between the pulses (Fig.3-2), in reality, we have signals with several peaks. To allow dilation distance to capture distance at different gray intensity levels (scales) of an image, it can be defined as:

$$dd_\lambda(f_i, f_j) = \min \{n \mid (f_i + \lambda \mathbf{1}) \oplus nB \geq f_j\} \quad (3.5)$$

where  $\mathbf{1}$  denotes a grayscale image with every pixel intensity

value of 1. Recall that, we have assumed  $f_i, f_j$  are scaled to be between  $[0, 1]$ .  $\lambda$  denotes the gray levels or pixel intensity levels (scale) at which one must compare  $f_i$  and  $f_j$ . By adjusting  $\lambda$  and introducing  $\mathbf{1}$ , we effectively allow the dilation distance to consider differences at different intensity levels, accommodating 1-D images with multiple peaks. The following properties are to be noted:

1. First, we have that at  $\lambda = 0$ ,  $dd_\lambda(.,.)$  corresponds to the definition of  $dd(.,.)$  in Eq.3.3.
2. Note that  $dd_{\lambda_1} \leq dd_{\lambda_2}$  if and only if  $\lambda_1 \geq \lambda_2$ . For example,  $dd_\lambda(.,.)$  decreases with  $\lambda$ . Here,  $\lambda_1$  and  $\lambda_2$  are two different values of  $\lambda$ .
3. As we have assumed that,  $f_i, f_j$  are scaled between  $[0, 1]$ , we have  $dd_1(f_i, f_j) = 0$ , because  $(f_i + \mathbf{1})$  will always be greater than or equal to  $f_j$ .

To generalize the dilation distance defined so far, we consider

$$\Delta(f_i, f_j) = \int_{\lambda=0}^1 dd_\lambda \approx \frac{1}{N} \sum_{i=0}^{N-1} (dd_{i/N}) \quad (3.6)$$

For example, we consider an average of  $dd_\lambda$  over all scales of  $\lambda$  to be the dilation distance. In practice, this is approximated

by the average over several levels, as shown in Eq.3.6. Here,  $N$  denotes the discretization parameter, the number of discrete  $\lambda$  values used to approximate the integral from 0 to 1. Specifically, the intensity interval  $[0, 1]$  is divided into  $N$  equally spaced steps/levels, and the average dilation distance is computed over these levels.

Fig.3-3 illustrates the above definitions. Consider the 1-D grayscale images  $f_1, f_2$  as shown in the figure. At scale  $\lambda = 0$ , the dilation distance would be the distance between the peaks  $d_1$ . For  $\lambda$  between  $(0, \lambda_1)$ , this value would not change. At  $\lambda_1$ , the distance drops to the next closest peak, and this distance would be equal to  $d_2$  as shown. Similarly, the next change would be when  $\lambda = \lambda_2 > \lambda_1$  when the distance would reduce to  $d_3$ . This is illustrated as a plot of  $dd_\lambda(f_1, f_2)$  versus  $\lambda$  on the right side of the Fig.3-3. The x-axis represents  $\lambda$  (intensity levels), and the y-axis represents the dilation distance. The quantity  $\Delta(f_i, f_j)$  is obtained as the area under this curve. Since this example is shown in the case of the 1-D image, it can be extended to 2-D images also. In the case of a 2-D image, if we visualize it as a 3-D surface (intensity value as 3rd dimension), the dilation distance vs  $\lambda$  curve can be seen as evaluating cross-sections of

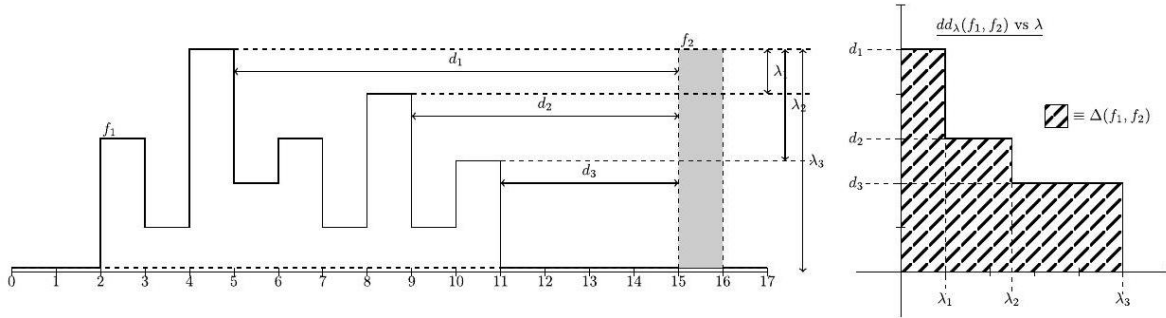


Figure 3-3: Figure illustrating the definitions of  $dd_\lambda(\cdot, \cdot)$  and  $\Delta(\cdot, \cdot)$ . On the left, we have two functions  $f_1$  and  $f_2$ . At scale  $\lambda = 0$ , the dilation distance between the peaks, is  $d_1$ . For all lambda between 0 and  $\lambda_1$ , this quantity would not change. At  $\lambda_1$ , the dilation distance would be the distance between the "closest" peaks, which gives  $d_2$ . The next change would be at  $\lambda_2$  when the distance further drops to  $d_3$ . Accordingly, one can plot  $dd_\lambda$  versus  $\lambda$  as shown on the right. The quantity  $\Delta(f_1, f_2)$  is obtained as the area under the curve.

this 3-D surface at different intensity levels  $\lambda$ .

Note that, as with  $dd(\cdot, \cdot)$ ,  $\Delta(\cdot, \cdot)$  is also non-symmetric. Hence, we consider

$$\widehat{\Delta}(f_i, f_j) = \Delta(f_i, f_j) + \Delta(f_j, f_i) \tag{3.7}$$

to be the dilation distance between the bands.

### 3.4 Complexity Analysis

The dilation operator typically has a time complexity of  $\mathcal{O}(n_p)$ , where  $n_p$  denotes the total number of pixels present in one grayscale band of  $H$ . The number of dilations required to get the distance between two bands using the disk structuring ele-

ment has a worst-case time complexity of  $\mathcal{O}(\sqrt{n_p})$ . If the set of bands is given by  $nz$ , then computing the dilation distance between all pairs will have a complexity of  $\mathcal{O}(|nz|^2)$ . Hence, the total complexity is obtained by  $\mathcal{O}\left(n_p^{3/2}|nz|^2\right)$ . However, this time complexity is based on single-thread processing and has a huge potential for parallelization. CUDA-based dilation operators [130] are comparatively very fast. Also, computing the distance between two different pairs is independent of each other and can be accomplished using independent processes that can easily be parallelized. Hence, given enough resources for parallel processing, the complexity could potentially be reduced to  $\mathcal{O}(\sqrt{n_p})$ . This is considered for future work.

### 3.4.1 Selection of a Subset of Bands Using Spectral Clustering

To select a subset of size  $K$ , we use spectral clustering [131–133]. Let  $V$  denote the set of vertices where each vertex corresponds to a single band of hyperspectral image  $H$ . Consider a complete graph, i.e., we assume all pairs of vertices are connected. Hence, the edge set is given by  $E = V \times V$ . We assume that the edge weight between two vertices corresponding to  $f_i$  and  $f_j$  is given by  $W_e(\{f_i, f_j\}) = \exp\left(-\beta * \widehat{\Delta}(f_i, f_j)\right)$ .

Then, we perform spectral clustering [133] on the graph  $G = (V, E, W_e)$ , to obtain  $K$  (required number of bands) clusters. Next, we identify the representative bands from each cluster as the bands that maximize the sum of similarities, that is

$$\arg \max_i \sum_j \exp \left( -\beta * \widehat{\Delta}(f_i, f_j) \right) \quad (3.8)$$

The value of  $\beta$  is identified empirically. We consider different values for  $\beta$  (here we use  $\{1, 3, 5, 10\}$ ) and use the optimal value for each case based on their effects on the clustering and subsequent classification performance of the selected bands.

To summarize the band selection using dilation distances,

1. First, compute the dilation distances between all pairs of bands using (Eq.3.7). This involves considering different intensity levels (scales) represented by  $\lambda$ .
2. Next, use the spectral clustering procedure (as described above) to identify the clusters of bands ( $K$ ). Each cluster will contain bands that are similar to each other in terms of their dilation distance, ensuring that the bands within a cluster have similar spectral characteristics.
3. Identify a representative band from each cluster by maxi-

mizing the sum of similarities, as described in Eq.3.8.

## 3.5 Experimental Result

### 3.5.1 Dataset Used

**University of Pavia:** The dataset used in our experiment is the Hyperspectral Image of Pavia University [134] acquired by ROSIS sensor. The size of the data is 610 by 610 pixels. However, some of the samples contain no information, so they are discarded. It has 103 spectral bands and 9 different classes. For illustrative purposes, Fig.3-4 shows the false color composition of Pavia University Data and its ground truth data with class details.

**Indian Pine Dataset:** The AVIRIS sensor collected a 145x145 pixel scene over Indiana's Indian Pines site [134], featuring 224 spectral bands within  $0.4\text{--}2.5 \times 10^{-6}$  meter wavelengths. This subset of a larger scene encompasses agriculture, forests, highways, a rail line, and sparse housing. Captured in June, early-stage crops like corn and soybeans covered less than 5% of the area. With non-mutually exclusive ground truth divided into 16 classes, some spectral bands were eliminated due to water absorption. The reduced 200-band data is accessible. for visu-



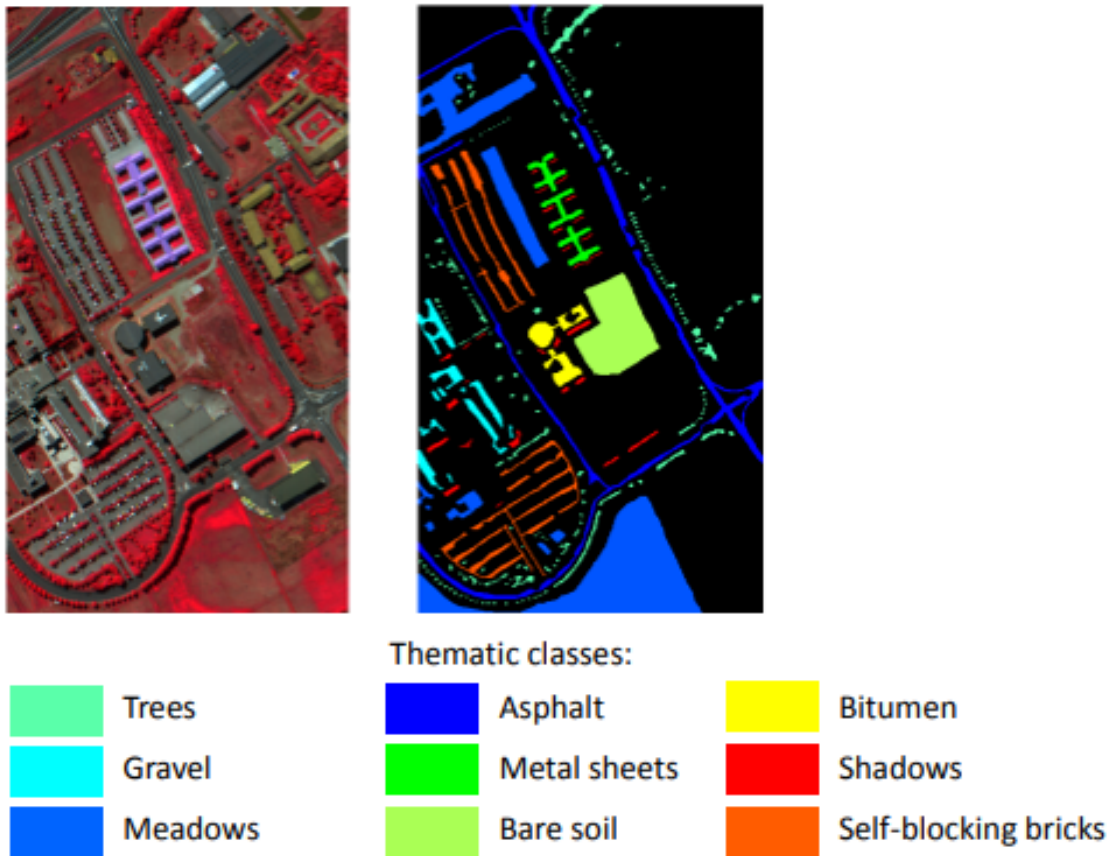


Figure 3-4: False color composition and ground truth representation of Pavia University. The false color composite image highlights various land cover types in different colors. The corresponding ground truth map of Pavia University delineates 9 different classes of land cover from its ground truth.

alization, the false color composition and corresponding ground truth data are shown in Fig.3-5.

### 3.5.2 Result Analysis

As illustrated in Fig.3-1, the main aspect that differentiates dilation distance-based band selection from other approaches is

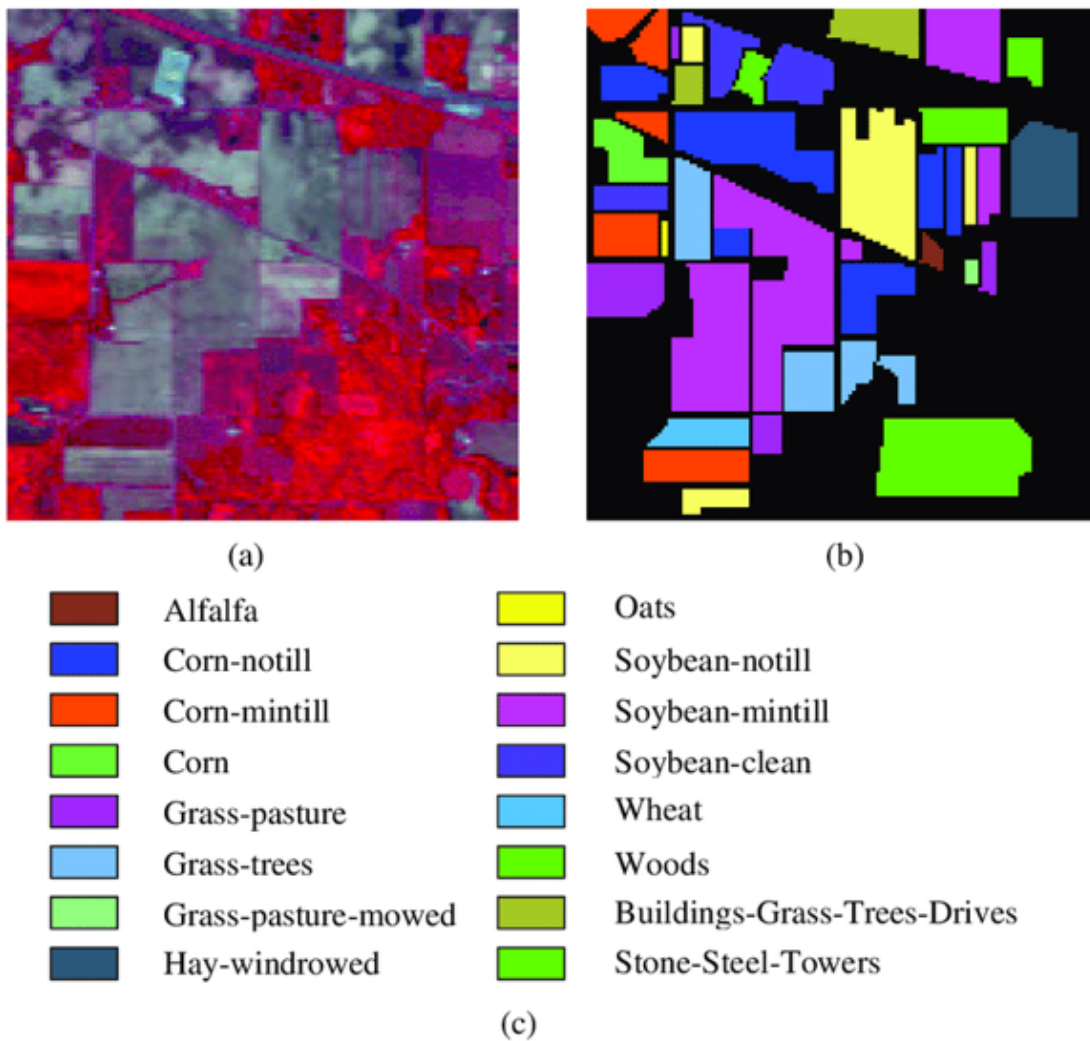


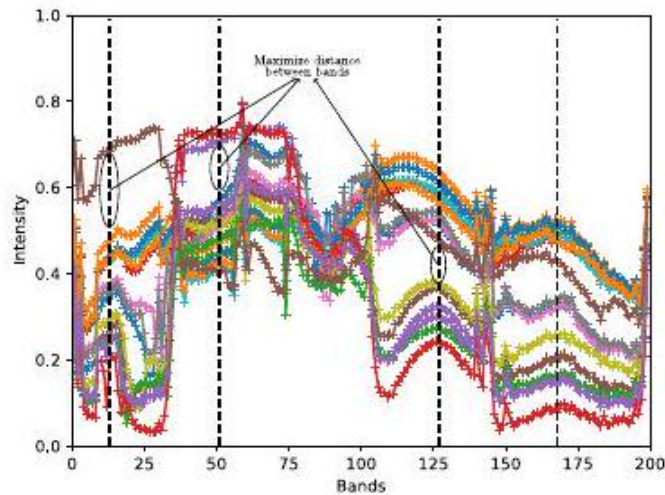
Figure 3-5: False color composition and ground truth representation of Indian Pine Dataset. The false color composite image highlights various land cover types in different colors. The corresponding ground truth map of the Indian Pine dataset delineates 16 different classes of land cover from its ground truth.

the fact that it selects the bands such that each band represents a unique spatial object in the image.

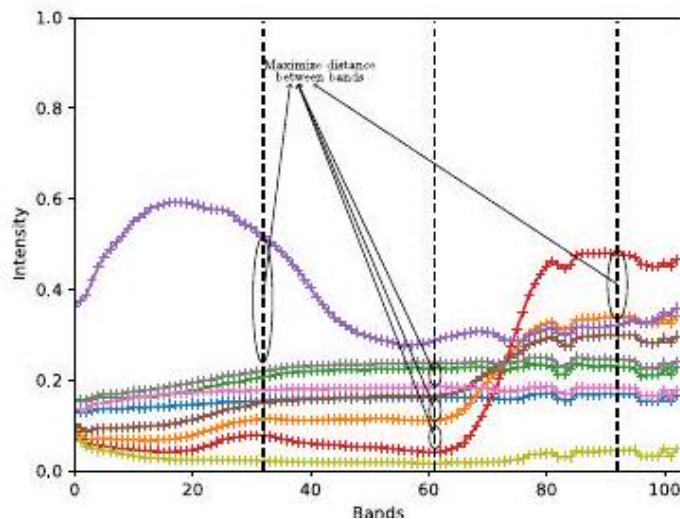
In this section, we use the real-world data sets Indian Pines data and the University of Pavia data to illustrate this aspect. We discuss cases where dilation distances are optimal as well as cases where they would not be optimal. The selected bands for both datasets are shown in Fig.3-6a and Fig.3-6b.

First, we answer: what are the bands selected using dilation distance? To answer this, we perform the following experiment: consider the average of pixels for each class in the ground truth and for each available band. These plots are shown in Fig.3-6. The bands selected are shown by vertical dashed lines. To understand this particular selection, recall that dilation distance selects those bands that highlight a single object. This implies bands where a single object/class gets highlighted the most. In practice, this translates to identifying the bands that maximize the encircled regions in Fig.3-6. In other words, it identifies those bands that can differentiate between the classes. This justifies the superior performance of dilation distance-based band selection.

For a quantitative evaluation of the method, we consider us-

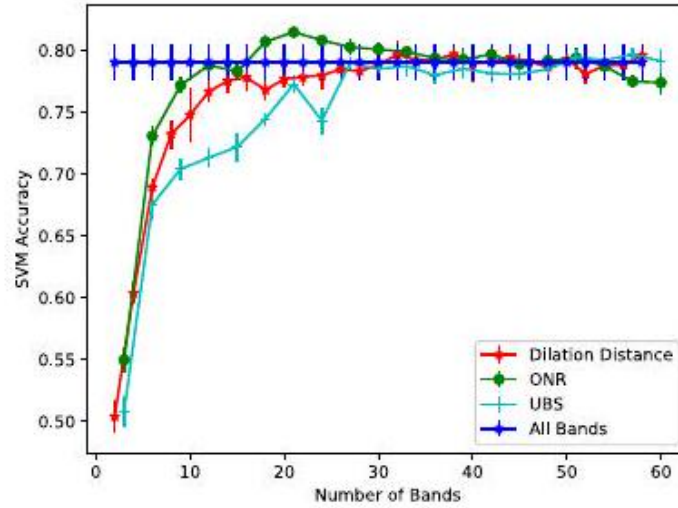


(a)

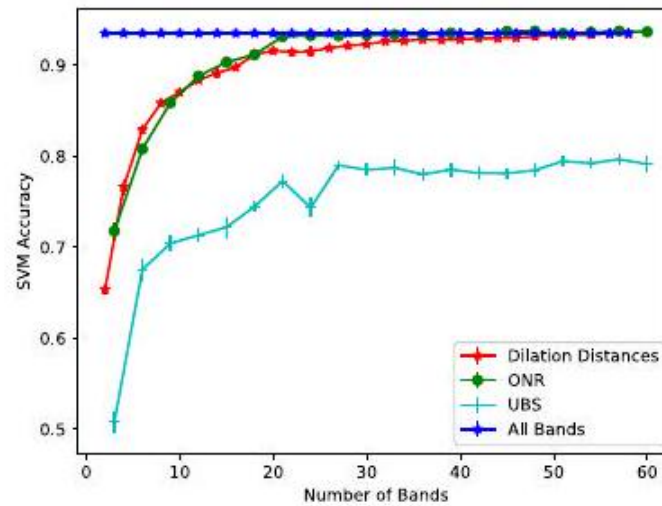


(b)

Figure 3-6: Figure illustrating the band selection by dilation distance. In (a), using the Indian Pines data set, we plot the average intensity of all pixels for each class for each band and obtain the plot as shown. The dashed vertical lines represent the bands selected using the dilation distances. Observe that the bands selected are such that the classes can easily be differentiated. This is because of the fact that dilation distance selects the bands such that spatial objects can easily be differentiated. A similar phenomenon is seen in (b), where the University of Pavia data set is used. (a) Indian Pines. (b) University of Pavia.



(a)



(b)

Figure 3-7: Accuracy versus the number of bands. For the evaluation of a subset of bands, we use the accuracies obtained by SVM. We split the data set into train (10%) and test (90%) and trained the SVM classifier on the training set with the given subset of bands. The testing accuracy is plotted versus the number of bands. The hyperparameters are selected using fivefold cross-validation. Baseline comparison with two other methods, ONR and uniform band selection (UBS), described in [128], is included. The number of bands for the dilation-distance approach is taken from 2 to 60 using a step size of 2. The number of bands for ONR and UBS is taken from 3 to 60 using a step size of 3.

ing the evaluation based on support vector machines (SVM) [135]. We split the data into train (10%) and test (90%) data sets. To evaluate a given subset of bands, we perform the SVM classification using only this subset of bands. Optimal hyperparameters are chosen using a fivefold cross-validation scheme. Here, the test accuracy would indicate how well the subset of bands represents the original set. Test accuracy is referred to as SVM accuracy or simply accuracy, depending on the context. Fig.3-7 shows the plots of accuracies versus the number of bands for Indian pines and the University of Pavia data sets. As a baseline, the accuracies when all bands are taken are also shown. Observe, from Fig.3-7a, that we reach the baseline very quickly at around 30 bands. However, from Fig.3-7b, the convergence to the baseline is slow. This is attributed to the fact that objects within the same class in the University of Pavia data set are disconnected. Hence, dilation distance-based band selection does not perform the best in this case. Table 3.1 compiles the results for 30 bands and compares them with existing approaches- Ward's Linkage strategy using Divergence (WaluDI) [136], Minimum-variance PCA (MVPCA) [137], Improved Sparse Subspace Clustering (ISSC)

[138], Adaptive Distance-Based Band Hierarchy (ADHB) [139], Optimal neighborhood reconstruction (ONR) [128], and Fast and Latent Low-Rank Subspace Clustering (FLLRSC) [140]. As per [138], ISSC obtains the current state-of-art results. We use three metrics- overall classification accuracy (OCA), average classification accuracy (ACA), and Kappa coefficient (KC).

		OCA	ACA	KC
Indian Pines	Dilation Distances	79.28	73.84	76.49
	All Bands	79.24	70.93	76.34
	WaluDI	77.15	69.35	73.86
	MVPCA	70.18	65.99	65.83
	ISSC	81.61	76.85	78.98
	ADBH	78.52	77.75	76.5
	ONR	79.00	76.45	77.27
	FLLRSC	82.31	***	***
University	Dilation-Distance	92.14	91.29	89.63
	All Bands	93.39	92.09	91.26
	WaluDI	86.04	83.69	81.11
	MVPCA	92.70	90.51	90.27
	ISSC	94.14	92.00	92.20
	ADBH	91.63	89.30	89
	ONR	92.28	92.24	89.84
	FLLRSC	94.41	***	***

Table 3.1: Evaluation Using SVM for 30 Bands. Note: OCA is considered \*\*\* indicated the results are not available.

The all-band accuracies are also provided as a baseline. Observe that dilation distance-based band selection performs compara-

bly with other approaches on the Indian pines data set. For the University of Pavia data set, it is comparable with other approaches except for ISSC, and FLLRSC. This, to reiterate, is due to the fact that dilation distance is not designed to capture objects that are disconnected, as is the case in the University of Pavia data set. Suitable preprocessing for dilation distance-based band selection would improve the results and is considered for future work.

### **3.6 Conclusion and Future Work**

To summarize, in this chapter, we use the dilation operator from MM to define dilation distance, which is in turn used for band selection. We show that dilation distance can capture spatial distances. Hence, we show that dilation distance-based band selection selects bands that identify a unique spatial object. We illustrate this property using both toy as well as real data sets. We empirically prove that dilation distance provides a competitive approach for band selection.

However, there are several avenues to improve this approach further. First, selecting suitable preprocessing steps to allow for objects that are spatially disconnected will improve the perfor-



mance of this approach. Also, other approaches to selecting the subset of bands based on dilation distance may be experimented with. We believe the main advantage of the current approach is that it can be used along with other approaches, such as ISSC. This is considered for future work. Also, one may ask a related question: identify the "signature" band of a given object, i.e., the band that differentiates it from the rest of the objects. Dilation distance is uniquely positioned to answer this question, and this is also considered for future work.



## Chapter 4

# Terrain Surface Generation via Hierarchical Median Set Based Interpolation

### 4.1 Introduction

Understanding Earth's topography is crucial for studying changes in shape, texture, and patterns resulting from natural or human alterations. Qualitative and quantitative topographic information is essential for analyzing climate, vegetation distribution, and surface processes. Traditionally, topographic maps have been used for quantitative analysis. A topographic map is a two-dimensional representation of a region's surface features, depicting elevation changes through the use of contour lines. Elevation refers to the height of a point on the Earth's surface

relative to the mean sea level. Contour lines on these maps connect points of equal elevation, effectively illustrating the three-dimensional landscape on a flat surface. Contour maps provide reliable elevation measurements, which is especially useful for studying historical landscapes. They are also cost-effective for covering larger areas with sparse data, making them an invaluable tool for modern topographic analysis.

Digital Elevation Models (DEMs), on the other hand, further enhance our understanding of topography by providing a 3-D digital representation of the terrain's surface. A DEM is a digital model that depicts elevation or the ground height above sea level, typically using a grid where each cell represents an elevation value. DEMs can be generated from both contour maps and remote sensing data. Despite advancements in remote sensing technologies, contour maps remain a preferred source for creating DEMs [141–143] or terrain surface. This is due to the accuracy of contour maps in representing true terrain elevations, whereas satellite data might mistakenly record object heights, like buildings or trees, as ground elevation [144]. Additionally, topographic maps remain a vital source of elevation data globally and offer unique insights into historical

landscapes where remote sensing can be cost-prohibitive. The simplicity and cost-effectiveness of storing and presenting large area DEMs using sparse data like contours, is another advantage. Thus, reconstructing terrain surfaces from contour maps is crucial for creating accurate DEMs, which are invaluable for further analyzing and visualizing surface properties.

In recent times, terrain surface reconstruction through interpolation methods, particularly using contour maps, has gained popularity. Reconstructing a topographic or terrain surface starts with the basic principle and assumption that it is continuous and smooth [145–147]. A topographic surface is often described as "continuous" and "smooth" for cartographic representation and modeling. "Continuous" suggests that the surface doesn't have any breaks or gaps, allowing for theoretical movement from any point to any other point without leaving the surface. "Smooth" refers to the absence of abrupt changes in gradient or direction, like cliffs or overhangs. Another primary assumption is that the gradient between the two contour lines is relatively linear. This means that the elevation change between the two contour lines is steady and consistent, not abrupt and drastic. It implies that the neighboring contours

carry a lot of information about the spatial location closed within those contours. Thus, most of the topographic surface reconstruction algorithms interpolate to create a terrain surface from the known existing elevation points [148]. The two most common methods for generating a terrain surface using contour lines are constructing triangulation of points (TIN) [149] on contours or interpolating onto a grid of contours. Grid of contours are represented as raster data, where raster data provides a structured method for storing, processing, and displaying spatial information. In this format, each area of interest is partitioned into rows and columns, forming a grid where each cell represents a specific location on the map. Within this grid, attributes such as elevation values are assigned to each cell, allowing for the representation of terrain features. For processing raster data, this grid can be treated as a pixel grid of 4N or 8N connectivity. In this chapter, our primary focus is on the methods for reconstructing the terrain surface from grid-based contour lines, which involves interpolating each pixel's elevation value from existing contour pixels [150]. In this thesis, we are considering an 8N-connectivity grid to represent contours and henceforth, it will be simply referred to as the grid for

the rest of this chapter. An in-depth discussion of various existing interpolation methods for terrain surface reconstruction is done [151–153]. However, many of them cannot show satisfactory outcomes in situations such as small ridges, valleys, modeling slopes, etc. Some are prone to smoothening or some are not able to provide the terrain trends or generate peaks that are not present in the input sample [154].

This chapter adopts a mathematical morphology-based approach to interpolate a terrain surface by generating intermediate contours from existing contour lines. This method utilizes a non-parametric binary morphological operator and morphological interpolation methods to interpolate the median contours in hierarchical order. In the study [155–157], it has been established that mathematical morphology (MM) operators are well suited for visualizing the geometry of terrain surfaces. Although the articles mentioned above, initially attempted to generate a smooth surface by generating intermediate contours using MM, in this chapter, we adopted the idea of hierarchically generating a median element set to determine the median contours between the source and target contours. Hausdorff’s Median Set calculation is conducted along with the Threshold Decomposition of

the raster form of the input contour map. The major contribution of this chapter includes the following: 1) for the first time, this binary morphological median set concept is utilized in generating terrain surface from contours using source and target sets extracted from contours, which give a morphing-like progression of how the source contour changes to the target contour, 2) the idea of threshold decomposition makes it less expensive to extract the contour boundary to decide the position of the median contour, 3) simplification of the intermediate contour generation problem to find the median elevation region from the binary set, 4) description of the contour region properties using a spatial and logical relationship in different scenarios. This approach of hierarchical recursive generation of intermediate contours to create a smooth and continuous terrain surface also preserves the geometric structure of existing contours and the newly generated intermediate contours. Here we also took care of the flat hilltop and saddle areas whose information is not available in the input contours.



## 4.2 Some Background Concept

### 4.2.1 Contour Lines

Contour lines, or isolines, connect points of equal elevation on a map, providing a clear representation of the terrain's elevation variations. As already mentioned, elevation refers to the height of a point or location on the earth's surface above a reference level, commonly measured from the mean sea level, providing crucial information about the vertical position of terrain features.

Contour lines, or isolines, are connected points having the same elevation values throughout the connected points. We assume that all the contours in the contour map are well-sampled and well-connected segments. Contour lines possess some inherent properties. Some of the contour properties include:

1. Two contours of different elevation values never intersect each other [158].
2. It always follows the child-parent or inside-outside relationship, e.g. if  $C_i$  and  $C_j$  are two contours and if their spatial relationship can be described as  $C_i$  is inside  $C_j$  or  $C_j$  is outside  $C_i$ , then it is always maintained an ordered rela-

tionship for their corresponding elevation values  $e(C_i)$  and  $e(C_j)$  such that,  $e(C_i) \geq e(C_j)$  or  $e(C_j) \geq e(C_i)$  [159].

3. Contour Region – An area surrounded by a closed contour is known as the Contour Region [159].
4. Any point  $p$  in the neighborhood of a contour point on the terrain surface, can have only two values, either greater than or equal to the contour elevation value or less than the contour elevation value. If all the points in a contour region are assumed to have the same elevation value, then it means that the region is assumed to be flat.

All these properties mentioned above carry important information for generating intermediate contours between two adjacent contours, which are essential for reconstructing the terrain surface.

#### **4.2.2 Hausdorff Erosion Distance and Hausdorff Dilation Distance**

Let  $E$  be a metric space, of distance  $d$ . So, for each non-empty subset  $X \subset E$  and  $Y \subset E$ , the classical Hausdorff distance is

defined as,

$$d_H = \max \left\{ \sup_{x \in X} d(x, Y); \sup_{y \in Y} d(y, X) \right\}$$

where,  $d(x, Y) = \inf\{d(x, y), y \in Y\}$ , which gives the distance from a point  $x \in X$  to  $y \in Y$ . In mathematical morphology, as mentioned in [160], the above-mentioned Hausdorff distance can be rewritten in terms of dilation ( $\delta_n$ ) and erosion ( $\varepsilon_n$ ) by SE  $B$  of size  $n$  in  $E$  [160]. These derived distances are called Hausdorff dilation distance ( $\rho(X, Y)$ ) and Hausdorff erosion distance ( $\sigma(X, Y)$ ) between non-empty compact set  $X$  and  $Y$  respectively.

$$\rho(X, Y) = \inf \{n : Y \subseteq \delta_n(X), X \subseteq \delta_n(Y)\} \quad (4.1)$$

$$\sigma(X, Y) = \inf \{n : \varepsilon_n(Y) \subseteq X, \varepsilon_n(X) \subseteq Y\} \quad (4.2)$$

where  $\delta_n(X)$  and  $\delta_n(Y)$  is dilation of  $X$  and  $Y$  by SE of size  $n$  and similarly  $\varepsilon_n(X)$ ,  $\varepsilon_n(Y)$  is erosion of  $X$  and  $Y$  by SE of size  $n$ . For instance, the Hausdorff erosion distance ( $\sigma(X, Y)$ ) between  $X$  and  $Y$  is defined as the smallest  $n$  such that  $X$  is contained within the erosion of  $Y$  by  $n$ -sized SE ( $B$ ), and vice

versa. Similarly, the Hausdorff dilation distance ( $\rho(X, Y)$ ) between  $X$  and  $Y$  is determined using dilation operations. Algebraically, these two distances are dual to each other and follow all the properties of a distance metric. For further properties and proofs, the reader can refer to [160].

The SE of size  $n$  mentioned in Eq.4.1 and Eq.4.2 can also be explained in their multi-scale version as a sequence of repetitive operation with SE of smaller size. For example, dilation ( $\delta$ ) and erosion ( $\varepsilon$ ) with a SE of size  $n$  are equivalent to dilation and erosion  $n$ -times with the same SE of size 1 (in case of disk SE). As mentioned in [60], formally, we can write it as:

$$\delta_n(B) = \delta_B(n)$$

This relation means that dilating the structuring element  $B$ ,  $n$  times is equivalent to considering a single dilation operation with a structuring element that has been scaled or expanded to size  $n$ .

### **4.2.3 Median Set Computation**

Jean Serra introduced a method to compute the median set in [160] using the Hausdorff dilation distance ( $\rho$ ) and Hausdorff

erosion distance ( $\sigma$ ) in Eq.(4.1) and Eq.(4.2). It is also known as Serra's median. Given two non-empty and ordered nested sets,  $X$  and  $Y$ , such that  $X$  is completely contained in  $Y$ , i.e.  $X \subseteq Y$ , the median ( $M$ ) between these two sets can be computed as:

$$M(X, Y) = \bigcup (X \oplus nB) \cap (Y \ominus nB) \mid \forall n \geq 0 \quad (4.3)$$

The concept of multi-scale erosion and dilation ( $nB$  denotes a structuring element obtained by  $B \oplus B \oplus B \dots$  (n times)  $\dots \oplus B$ ) is used during the computation of the median set. We can say that  $M$  is midway between  $X$  and  $Y$  and call it a median, as for every point  $m' \in M$ ,  $\exists n \geq 0$  such that  $d(m', X) \leq n$  and  $d(m', Y^c) \geq n$ , where  $d$  is the distance between two sets as discussed in section 4.2.2,  $Y^c$  is the complement of set  $Y$  and  $\bigcup$  denotes union operation. From this observation, it can be implied that this median set follows a symmetrical property. It is shown in [160] that the median set  $M(X, Y)$  is at  $\mu$  Hausdorff dilation distance from  $X$  and  $\mu$  Hausdorff erosion distance from  $Y$ .  $\mu$  is defined as:

$$\mu = \inf \{n : n \geq 0, (X \oplus nB) \supseteq (Y \ominus nB)\}$$

From the above-mentioned relation, it can be claimed that if  $X$  and  $Y$  are ordered and non-empty sets and  $X \subseteq Y$ , then also  $X \subseteq M(X, Y) \subseteq Y$ . For further proof and properties, readers can refer to [160].

#### 4.2.4 Threshold Decomposition

A digital gray-scale image signal  $f(x, y)$  at pixel location  $(x, y)$  is assumed to be a non-negative 2D sequence, with intensity values  $q = 0, 1, 2, \dots, Q$ . This signal can be thresholded at all possible intensity values  $0 < q < Q$  to obtain  $Q + 1$  threshold binary images denoted as  $f_q(x, y)$ , where,

$$f_q(x, y) = \begin{cases} 1, & \text{if } f(x, y) \geq q \\ 0, & \text{if } f(x, y) < q \end{cases} \quad (4.4)$$

The reconstruction of the original image  $f$  from its thresholded binary images can be expressed as :

$$\begin{aligned} f(x, y) &= \sum_{q=1}^Q f_q(x, y), \quad \forall x, y \\ &= \max\{q : f_q(x, y) = 1\} \end{aligned} \quad (4.5)$$

Thus, applying an discrete space image transformation  $\Omega$  to the threshold image and original image  $f$  gives [161] the following:

$$\Omega[t_q(f)] = t_q[\Omega(f)] \quad \text{where } t_q(f) = f_q \quad (4.6)$$

This relationship holds true for all  $q$  and for the entire image domain  $x, y$ . For further details, readers can refer to the article [161].

### 4.3 Methodology

The primary objective of this work is to reconstruct the terrain surface by generating intermediate contours from existing contour lines within a given contour map. The task involves recursively determining intermediate contours between two successive pairs of contours termed as source and target contours. This problem of terrain surface reconstruction from a contour map can be formally stated as follows:

Given a pair of adjacent contours denoted as  $C_i$  and  $C_j$  with their respective elevation values denoted as  $e_i = e(C_i)$  and  $e_j = e(C_j)$  (for simplicity,  $e(C_i)$  will be referenced as  $e_i$  henceforth). Defining an enclosed inter-contour space as  $\varphi$ , the ob-

jective is to generate all possible intermediate contours  $C_m \in \varphi$  such that  $e_i < e(C_m) = e_m < e_j$ . The aim is to reconstruct a terrain surface  $\Psi$  across the image space such that  $\forall p \in \varphi, \quad e(p) = e_i, \text{ if } p \in C_i \text{ and } e(p) = e_j, \text{ if } p \in C_j \text{ and } e(p) = [e_i, e_j], \text{ if } p \in \varphi$ , where,  $e(p)$  or  $e_p$  is elevation value of any point  $p$  in the intercontour space( $\varphi$ ) between  $C_i$  and  $C_j$ . This statement can be extended to the scenario where  $n > 2$  involves more than two contours  $C_i$  with corresponding elevations  $e_i$ . The special cases of extrapolating summits, which are the highest points of elevated terrain, where  $C_j = \phi$ , or pits, representing depressions or low points in the terrain, where  $C_i = \phi$ , are also discussed here. Contour morphology and contour line properties are vital in producing intermediate contours between any successive contours. The proposed approach is also based on some given contour properties and assumptions that have already been discussed. Further, a series of simplifications of the problem of intermediate contour generation to median set computation is also to be discussed.



### **4.3.1 Intermediate Contour Generation**

Based on the properties of the contour lines discussed in the above sections, the objective of reconstructing the terrain surface by generating intermediate contours between two successive contours can be achieved by the sequential steps as follows:

1. As we propose a grid-based approach, we convert available contour maps (if they are not already a grid of contours) into a regular grid-based (8N-connectivity) contour (raster format using GIS tools), where each grid point represents a location on the map. Converting shapefiles to raster data is a common preprocessing step in geographic information systems (GIS) and spatial analysis workflows, especially when working with spatial data for tasks such as terrain analysis. This conversion represents contour lines in terms of the grid, rendering them suitable for subsequent grid-based interpolation techniques.
2. Using Threshold Decomposition, the contour map is decomposed into a set of binary images at each contour elevation level present, termed as Threshold Elevation regions (TERs).

3. Establishing a spatial relationship between TERs extracted and their categorization.
4. Computation of Median Elevation Region (MERs) recursively using the Median Set computation method between two successive TERs.
5. Generation of a sequence of intermediate contours, based on the produced MERs for every pair of input successive TERs, achieved through computing the Morphological Gradient of MERs.
6. Assigning the computed elevation values to the obtained intermediate contours.
7. Repeat the steps from 2 to 6, for all the successive input contours, until no other contour can be generated or the inter-contour space is completely exhausted. Complete exhaustion of the inter-contour space is indicated when all the pixels of the inter-contour space have values greater than 0 (0 belongs to the background and 1 belongs to the foreground pixels). The number of intermediate contours that can be generated depends on the width between two successive contours.

For a better understanding, Fig.4-1 illustrates a flow diagram, providing a sequential representation of the steps required to compute intermediate contours between successive contours, which in turn produce a smooth terrain surface (DEM) from a contour map. A complete algorithm to generate intermediate contours and a terrain surface (DEM) from a given contour map is given in Algorithm 1.

---

**Algorithm 1** COMPUTE INTERMEDIATE CONTOURS
 

---

**Input:** Contour map with a set of contours  $C_i$   
**Output:** Grid of Interpolated heights/digital elevation model

- 1:  $W \leftarrow$  Input image
- 2: **Elv\_Reg**  $\leftarrow$  total number of contours in  $W$
- 3: **for** each  $i$  in **Elv\_Reg** **do**
- 4:  $e_i \leftarrow$  elevation of contour  $C_i$
- 5:  $e_{i+1} \leftarrow$  elevation of contour  $C_{i+1}$
- 6: Initialize an empty queue  $Q$
- 7:  $S \leftarrow$  Intercontour Space between  $C_i$  and  $C_{i+1}$
- 8:  $T_i \leftarrow$  compute TER for contour  $C_i$  using Eq.4.7-Eq.4.9
- 9:  $T_{i+1} \leftarrow$  compute TER for contour  $C_{i+1}$  using Eq.4.7 - Eq.4.9
- 10:  $Q.enqueue((T_i, T_{i+1}))$   $\triangleright$  refer to [162] for enqueue operations
- 11: **while**  $S.any() < 0$  **do**  $\triangleright S$  is pixels in inter-contour space  $S$
- 12:  $P \leftarrow Q.dequeue(0)$   $\triangleright$  refer to [162] for dequeue operations
- 13:  $T_i \leftarrow P[0], T_{i+1} \leftarrow P[1]$
- 14:  $M \leftarrow$  compute MER for  $(T_i$  and  $T_{i+1})$  using Eq.4.10-Eq.4.13
- 15:  $C_m \leftarrow$  compute morphological gradient of  $M$  using Eq.4.14
- 16:  $e_m \leftarrow 1/2(e_i + e_j)$  -Eq.4.15
- 17: Update  $W$  with the contour  $C_m$
- 18:  $Q.enqueue((T_i, M), (M, T_{i+1}))$
- 19: **end while**
- 20: **end for**

---

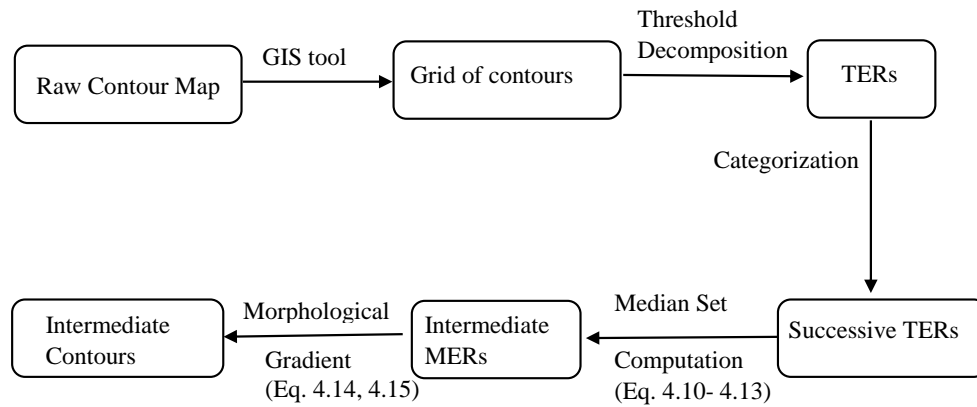


Figure 4-1: A Sequential Representation of the Methodology to generate intermediate contours from successive contours from a contour map.

### 4.3.2 Extraction of Threshold Elevation Regions

The objective of this method is to generate a surface of higher spatial resolution from the available sparse contours, in other words, low spatial resolution elevation contours. The properties of isolines or contour lines ensure that two contour lines are always approximately parallel, creating a constant contour interval. Moreover, the elevations rarely deviate from the slope defined by the contours [159]. As mentioned in earlier literature, the terrain surface can be generated by inserting new contours midway between the successive contours. Our proposed algorithm computes these new intermediate contours by computing recursively the sequence of the Median Elevation Re-

gions (MERs) using the median set computation between two successive contour lines. Since the new intermediate contour we generate is approximately midway between two successive contours, the new intermediate contour is assigned an elevation of the mean of the considered two successive contours.

The methodology mentioned here is applied to a grid of contour lines. All the topographic maps are available as a shape file. In the very first step, all the shape files are converted to raster data. The set of contour lines is then presented as a grid of data.

The raster image of contours obtained from processing the topographic map can be considered a greyscale image with intensity values of the elevation of the contour lines. Instead of processing the grid of the contour map as a grayscale image, a procedure is proposed here for generating binary input images of contour regions from a limited set of layers, i.e. the input set of contours. For example, if we have a grid representing a terrain with various contour lines indicating different elevation levels, a binary input set of contour regions could be generated by assigning a value of 1 to pixels within each contour region and a value of 0 to pixels outside those regions.

The contour information presented in a given contour map can be considered as spatially layered information about an object or event. This information can be ordered, semi-ordered, or disordered. For example, if we have two contours  $C_i$  and  $C_j$ , let us denote their extracted binary contour regions at each contour elevation level as  $X_i$  and  $X_j$ , respectively. For notational simplicity, we denote  $X_i$  and  $X_j$  as sets, and we term them as source set and target set, respectively. let  $k$  and  $l$  represent the respective numbers of subsets present in  $X_i$  and  $X_j$  (an example is given in Fig.4-2 to give an idea of how these subsets are considered), where  $k$  is the number of subsets in  $X_i$  and  $l$  is the number of subsets in  $X_j$ . Consequently, all the subsets present in the sets  $X_i$  and  $X_j$  are denoted as  $X_i^1, X_i^2, \dots, X_i^k$  and  $X_j^1, X_j^2, \dots, X_j^l, \forall i, j, k, l \in \mathbb{N}$ .

A simple method is suggested here for extracting these sets ( $X_i$  and  $X_j$ ) from the input contour map. In terms of elevation levels, we call them threshold elevation regions (TERs). Based on Eq: 4.4- 4.6, we generate TERs for each available elevation value. Let us consider the input contour map as a 2-D sequence  $f(x, y)$ , which assumes all the elevation levels of contours as intensity values:  $e_i$ , for  $i \in \{1, 2, \dots, nc\}$ , where

$e_i$  is the elevation levels or intensity level for all contours  $C_i$  in  $f(x, y)$ . At all possible intensity levels (elevation levels)  $\forall i, e_i$ , we threshold the image  $f(x, y)$  such that we obtain the set of thresholded binary images.

$$\forall e_i \quad f_{e_i}(x, y) = \begin{cases} 1 & \text{if } f(x, y) = e_i, \\ 0 & \text{if } f(x, y) \neq e_i. \end{cases} \quad (4.7)$$

In simpler terms, this equation denotes that for each contour level, we create a binary image where the pixels are either 1 (representing points on the contour) or 0 (representing points not on the contour) based on whether their elevation matches the current contour level. This process is repeated for each contour level to obtain a set of threshold binary images. The set of binary images obtained using Eq.4.7 gives us all the contours at each elevation level. We convert them to threshold elevation regions (TERs) by considering the regions under the contours as flat regions, i.e. with the same elevation value as the contour. Let us assume that  $C_i$  and  $C_{i+1}$  are two consecutive contours, and  $e_i$  and  $e_{i+1}$  are their respective elevation values. Thus, two cases are discussed to obtain their corresponding TERs.

**Case 1:**  $e_i > e_{i+1}$

$$TER_i = T_i = f_{e_i}(x, y) = \begin{cases} 1 & \text{if } f(x, y) \leq e_i, \\ 0 & \text{otherwise.} \end{cases} \quad (4.8)$$

**Case 2:**  $e_i < e_{i+1}$

$$TER_i = T_i = f_{e_i}(x, y) = \begin{cases} 1 & \text{if } f(x, y) > e_i, \\ 0 & \text{otherwise.} \end{cases} \quad (4.9)$$

In these equations,  $T_i$  represents the binary image (TER) obtained from  $f_{e_i}(x, y)$  by considering all the points within the contoured region where  $f(x, y) \leq e_i$  or  $f(x, y) > e_i$  for contour  $C_i$ . These equations outline the method for generating TERs representing contours from an input contour map based on elevation values. The purpose of these equations is to generate threshold elevation regions (TERs) that segment the contour map based on elevation values. They create binary images highlighting specific regions either below or above a given contour elevation, helping in the identification of different elevation levels (see Fig.4-3). It simplifies the interpolation of intermediate contours between consecutive contour levels. The



obtained TERs,  $T_i$ , follow some property that either  $T_i \subseteq T_{i+1}$  or  $T_{i+1} \subseteq T_i$ . We simplify the process of finding intermediate contours between two successive contours by interpolating between two successive thresholded elevation regions (TER) ( $T_i$  and  $T_{i+1}$ ) corresponding to the contours  $C_i$  and  $C_{i+1}$  respectively, instead of directly interpolating between the contours themselves ( $C_i$  and  $C_{i+1}$ ).

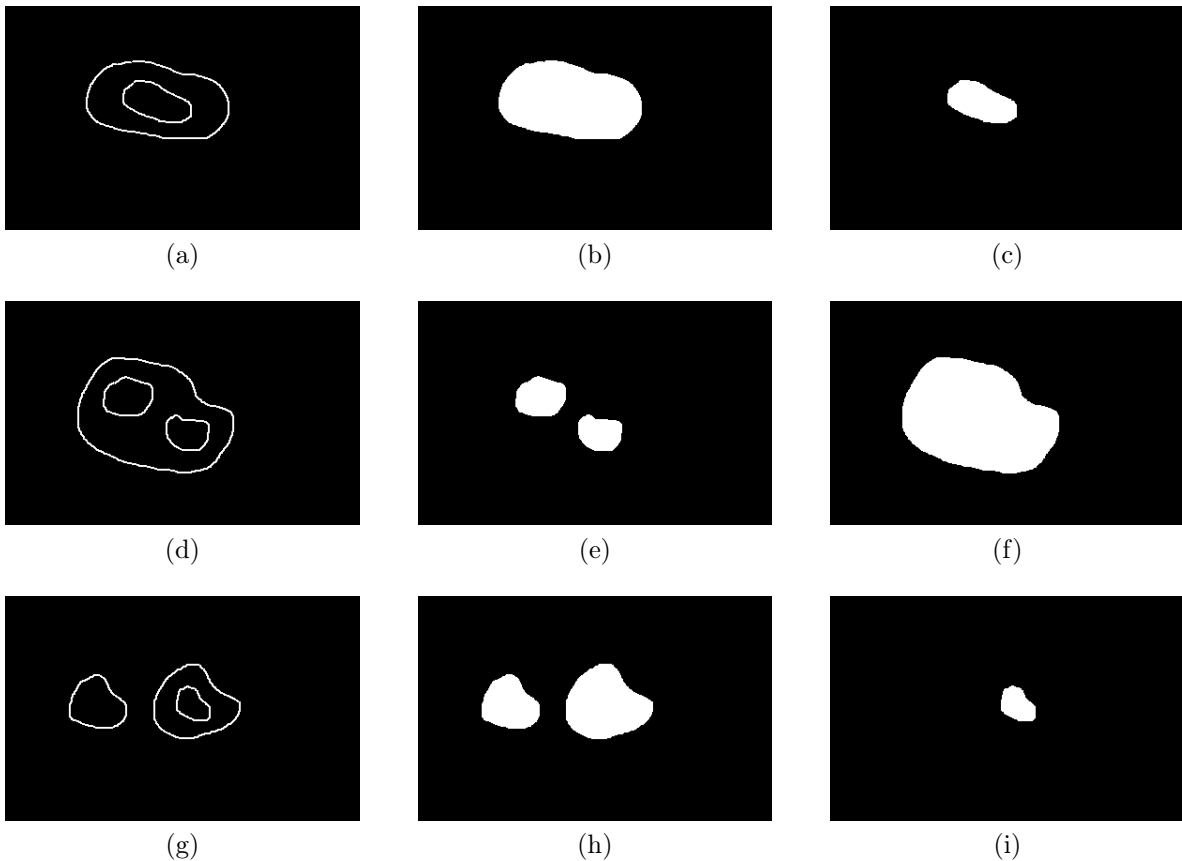


Figure 4-2: (a), (d), (g) Represent different possible cases of nested contours; (b), (c) represents corresponding TERs of (a); (e), (f) represents that of (d) and (h),(i) represents that of (g).

Fig.4-2a, Fig.4-2d, Fig.4-2g shows three different examples of possible nested contours, Fig.4-2b, Fig.4-2c are two TERs obtained from Fig.4-2a, similarly Fig.4-2e, Fig.4-2f are obtained from Fig.4-2d, and Fig.4-2h and Fig.4-2i are corresponding TERs of Fig.4-2g. All the TERs extracted are nothing but binary images. Two adjacent TERs  $T_i$  and  $T_{i+1}$  can be further assumed as two sets  $X_i$  and  $X_j$  along with their  $k$  and  $l$  numbers of subsets in each set, respectively, as discussed earlier.

### 4.3.3 Spatial Relationship between TERs

Let  $T_1, T_2, \dots, T_{nc}$  be the TERs corresponding to the contours  $C_1, C_2, \dots, C_{nc}$ . As we can recall, all the TERs ( $T_i$ ) derived are nothing but binary images. These TERs are represented as sets. If  $T_i \subseteq T_{i+1}$  or  $T_{i+1} \subseteq T_i$ , then  $T_i$  and  $T_{i+1}$  are ordered sets. If  $T_i$  and  $T_{i+1}$  are partially contained in each other, then it is semi-ordered. If there is no intersection between  $T_i$  and  $T_{i+1}$ , then sets are disordered. Here, we only discuss the ordered and disordered TERs, as we know that contours do not intersect each other.

Intuitively, the sets  $T_i$ ,  $i = 0, 1, \dots, nc$  represent the elevation profile of the cross-section of the area at a specific spa-

tial position. The profile evolves based on its slope to the next elevation profile,  $T_j$ , where  $j = i + 1$ . Let us consider  $\{T_i^1, T_i^2, \dots, T_i^k\}$  and  $\{T_j^1, T_j^2, \dots, T_j^l\}$ ,  $\forall k, l \in \mathbb{N}$  are the corresponding subsets/connected components in each set  $T_i$  and  $T_j$ . We can study every possible spatial relationship between consecutive TERs  $T_i$  and  $T_j$ , where  $j = i + 1$ . Based on the different spatial relationships, TERs can be grouped into some categories based on their corresponding subsets/connected components ( $k$  or  $l$ ) as follows:

- **Category 1:** This category satisfies simple conditions of a spatial relationship between  $T_i$  and  $T_j$ , where  $T_i \subseteq T_j$  or  $T_j \subseteq T_i$  and  $T_i^k \cap T_j^l \neq \phi$ , where  $T_i^k \in T_i$  and  $T_j^l \in T_j$ . This category includes the criteria for its corresponding subsets or connected components, a)  $\forall k, l$ ,  $T_i^k \subseteq T_j^l$  or  $T_j^l \subseteq T_i^k$ , where  $k = l$ , b) when  $k \neq l$ , for each  $T_i^k \in T_i$  there exist  $T_j^l \in T_j$  such that  $T_i^k \subset T_j^l$  or for each  $T_j^l \in T_j$  there exist  $T_i^k \in T_i$  such that  $T_j^l \subseteq T_i^k$ . The criteria mentioned in b) can arise as shown in examples Fig.4-2d and Fig.4-2g.
- **Category 2:** In some nested cases, where  $k \neq l$  and there exist some  $k$  and  $l$  such that  $T_i^k \cap T_j^l = \phi$ . An example of such a case is the hilltop area as shown in Fig.4-2h, where

the left-side TER is a probable case of a hilltop or the ultimate TER consists of the hilltop contoured area or the saddle point area which does not have the corresponding TER to interpolate with.

The above-mentioned category 1 globally belongs to the set category  $T_i \cap T_j \neq \phi$ , whereas category 2 belongs to  $T_i \cap T_j = \phi$ , assuming that some of the subsets or connecting components are empty sets.

#### **4.3.4 Intermediate Contour Computation using Median Set**

Serra's median, mentioned in Eq.4.3, considers the input sets  $X$  and  $Y$  globally, instead of focusing on local or individual elements, regions, or connected components within these sets. But, as we can see from the spatial relationships between TERs, the interpolation of subset layers from the input contour sets is category-dependent. To better visualize the spatial transition of a subset from one elevation profile to another, we compute the median sets termed as median elevation regions (MERs) between successive TERs ( $T_i, T_{i+1}$ ) in a category-wise manner, as described in Section 4.3.3. The generation of MERs and its corresponding intermediate contours on synthetic data are

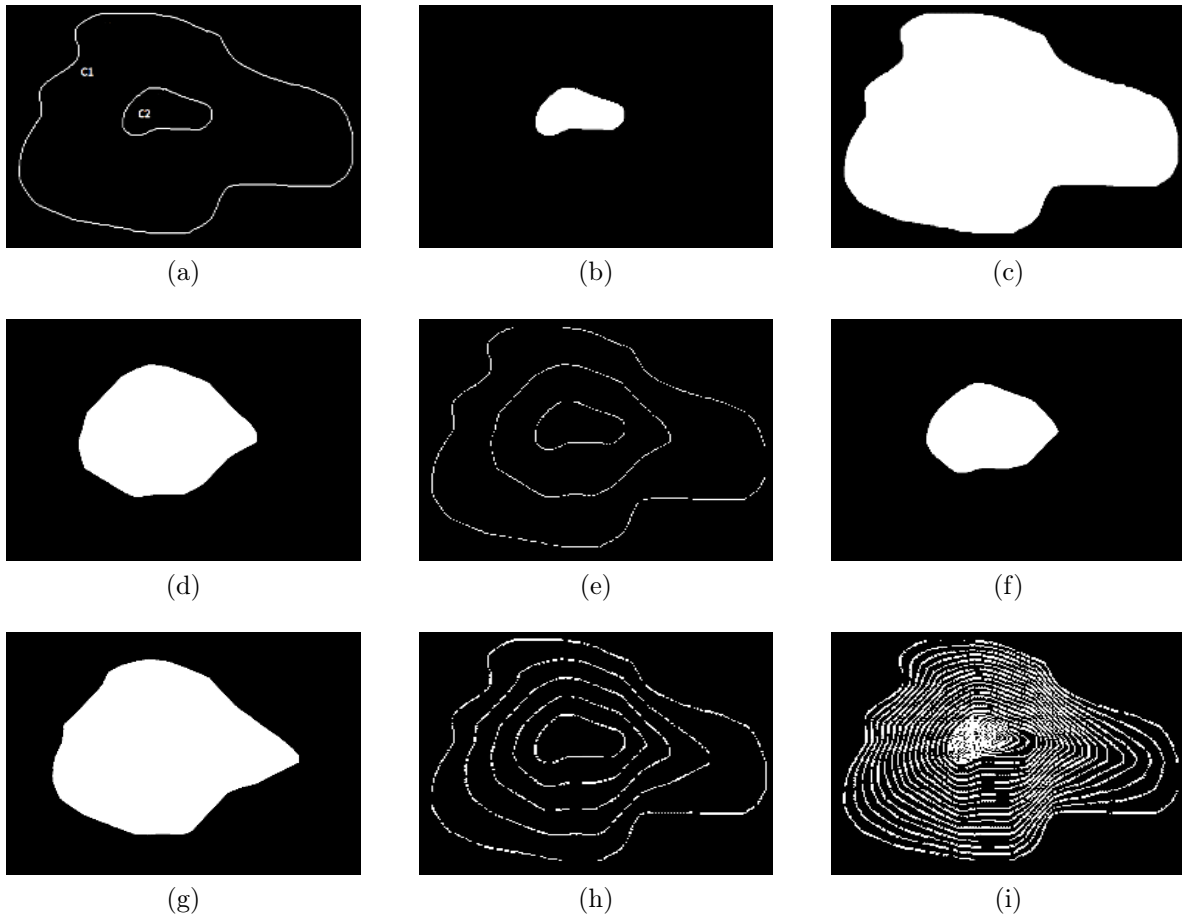


Figure 4-3: (a) A pair of contours  $C_1$  and  $C_2$  such that  $e_1 < e_2$  where  $e_1$  and  $e_2$  are their respective elevation; (b) and (c) are corresponding TERs extracted from (a); (d) computed MER of (b) and (c), denoted as  $M$ , obtained after 1st iteration by using the proposed method; (e) intermediate contour computed using morphological gradient on obtained  $M$ ; (f) and (g) are 2nd level MERs between  $C_1, M$  and  $M, C_2$ ; (h) contours generated after 2nd iteration; and (i) intermediate contours generated after 3rd iterations.

shown in Fig.4-3. The computation of MERs from two successive TERs are represented as follows:

Case 1:

a)  $T_i^k \subseteq T_{i+1}^l$

$$MER(T_i^k, T_{i+1}^l) = \bigcup_{n=1}^{\mathbb{N}} ((T_i^k \oplus nB) \cap (T_{i+1}^l \ominus nB)) \quad (4.10)$$

b)  $T_{i+1}^l \subseteq T_i^k$

$$MER(T_{i+1}^l, T_i^k) = \bigcup_{n=1}^{\mathbb{N}} ((T_i^k \ominus nB) \cap (T_{i+1}^l \oplus nB)) \quad (4.11)$$

Since  $T_i^k$  and  $T_{i+1}^l$  are subsets of  $T_i$  and  $T_{i+1}$  respectively, the  $MER(T_i, T_{i+1})$  can be computed based on the categories they fall into, as follows:

$$MER(T_i, T_{i+1}) = \bigcup_{\forall k,l} MER(T_i^k, T_{i+1}^l) \quad (4.12)$$

Case 2:

Under unique situations as explained in Category 2, the MER can be computed as:

$$MER(T_{i+1}^l, T_i^k) = \bigcup_{n=1}^N ((UT_i^l \oplus nB) \cap (T_i^l \ominus nB)) \quad (4.13)$$

Where  $UT_i^l$  is the ultimate eroded version of  $T_i^l$ .

Eq.4.13 can be used to compute MERs for hill-top regions. In category 2 cases, where there are no successive TERs ( $T_{i+1}$ ) or corresponding successive subsets, the MERs are computed as follows: the MERs are calculated by taking the ultimate erosion of the TER ( $T_i$ ) or any subset ( $T_i^l$ ) whose corresponding successive subset is empty. We treat the ultimate erosion of such TERs as  $T_{i+1}$ . The elevation level of this ultimate eroded version  $T_{i+1}$  is assumed to be  $e_{i+1} = (e_i + \text{contour interval})$ , where  $e_i$  is the initial elevation of  $T_i$  and the contour interval is the vertical distance or difference in elevation between adjacent contour lines in a contour map. For instance, if the elevation level of the TER  $T_i$  is  $e_i$ , say 100 meters, and the contour interval is 10 meters, then the elevation level after ultimate erosion  $e_{i+1}$  assumed to be 110 meters.

Finally, the intermediate contours are computed from the MERs obtained with Eq.4.10 to Eq.4.13, by applying the Morphological Gradient (MG). The morphological gradient (MG)

can be defined as the difference between the dilation and erosion of two images or sets. Therefore, the intermediate contour (IC) between two contours  $C_i$  and  $C_{i+1}$  is derived from the computed MERs as follows:

$$\begin{aligned} IC(C_i, C_{i+1}) &= C_m = MG(MER(T_i, T_{i+1})) \\ &= (MER(T_i, T_{i+1}) \oplus B) - (MER(T_i, T_{i+1}) \ominus B) \end{aligned} \quad (4.14)$$

where  $B$  is 3x3 square flat structuring element and  $IC(C_i, C_{i+1})$  is the intermediate contour between  $C_i$  and  $C_{i+1}$  and denoted as  $C_m$ . Also as we already know,  $\oplus$  and  $\ominus$  are the dilation and erosion operator respectively

After computing the intermediate contours, we assign the elevation values of the intermediate contours  $C_m$  as:

$$e(C_m) = e_m = 1/2\{e_i + e_{i+1}\} \quad (4.15)$$

where  $e_i$  and  $e_{i+1}$  are the elevation values of  $C_i$  and  $C_{i+1}$  respectively.



---

### 4.3.5 Complexity Analysis

This method, as presented through Eq.4.7 to Eq.4.15, provides a systematic way of computing intermediate contours in the context of successive TERs and subsequently the intermediate contour computation from its successive input TERs. Let's consider the case where we have a sequence of input contours, denoted as  $C_i$  and  $C_{i+1}$ . In this scenario, we can assume that the first contour in this sequence,  $C_i$ , is denoted as  $C_0$ , and the successive contour  $C_{i+1}$ , is denoted as  $C_1$ . With these assumptions, we can now discuss the computation of the intermediate contour, which serves as a transition between the contours  $C_0$  and  $C_1$ . So the first intermediate contour can be considered as  $C_{0.5} = IC(C_0, C_1)$ , where  $C_{0.5}$  is approximately midway between  $C_1$  and  $C_0$  and it breaks down the inter-contour space into two subspace. Next, we can compute the intermediate contours between  $C_{0.5}, C_1$  and  $C_0, C_{0.5}$  which are again approximately midway between  $C_0, C_{0.5}$  and  $C_{0.5}, C_1$ . The maximum number of intermediate contours that can be generated in between two successive contours depends on the width of the contour space. Thus, the recursive computation of the intermediate contours divides each time the inter-contoure space into two subspaces.

Since the inter-contour space is independent of each other and can be processed in parallel. So we can say the process takes  $\log_2 \varphi$ , where  $\varphi$  is the inter-contour space.

## 4.4 Results and Discussion

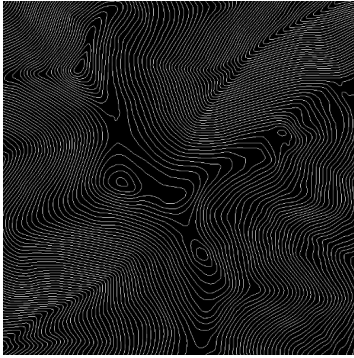
The proposed method mentioned is applied to real contour data to demonstrate its applicability. An overview of how the method works in synthetic data and its result is already shown in Fig.4-3. In Fig.4-3a, it is given as input contours  $C_1$  and  $C_2$ ; Fig.4-3b and Fig.4-3c are its respective TERs; Fig.4-3d is first level MER between Fig.4-3b and Fig.4-3c denoted as  $M$  using the proposed method; Fig.4-3e is the intermediate contour between  $C_1$  and  $C_2$  at first iteration; Fig.4-3f, Fig.4-3g are the corresponding second level MERs between  $C_1, M$  (MERs between Fig.4-3c and Fig.4-3d) and  $M, C_2$  (MERs between Fig.4-3d and Fig.4-3b); Fig.4-3h shows the intermediate contours computed from Fig.4-3f and Fig.4-3g at 2nd iteration; Fig.4-3i is showing the contours generated after 3rd iteration. This method also interpolates intermediate contours of hilltop regions using Eq.4.13 as shown in Fig.4-3i. For the best applicability, we consider some sparse contour data and examine how they

can produce dense spatial distribution or a continuous grid of interpolated elevation values. We consider demonstrating the proposed method to a set of contours extracted from a portion of the topographic map from the United States Geological Survey (USGS) [163] in the form of a Digital Line Graph (DLG). The procedure is applied to a grid of contours only. Since the proposed method works only on grid of contours, at first the obtained contours are preprocessed to a raster format (raster data are presented in terms of grid ) using QGIS and ArcGIS software. During vector conversion to a raster format, there might be some errors, which is inevitable. Because of these errors, some undesired artifacts and errors may have been formed on occasion.

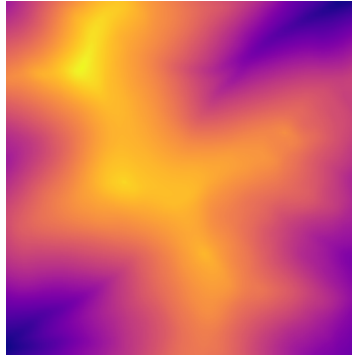
#### **4.4.1 Case study on Mt. Washington, NH**

Two sets of contours named “Zone A” (800x800 grid, Fig.4-4a) and “Zone B” (500x500 grid, Fig.4-4d) from the topographic map of Mt. Washington [163], are chosen to demonstrate the proposed method mentioned above. The contour interval is 20 meters in both cases and the elevations range from 2300-3540 meters in Zone A and 1140-1920 meters in Zone B re-

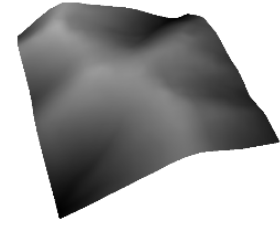
spectively. In both Category 1 and Category 2, the spatial relation of TERs can be observed in Zone A, whereas in Zone B, the TERs obtained can be classified as Category 1 only. The topographic surface is computed in both zones by computing the maximum possible intermediate contours between successive TERs using Eq.4.7 to Eq.4.15. Fig.4-4b and Fig.4-4e are the topographic surfaces computed using the proposed method from Figs.4-4a and Fig.4-4d, respectively. For better visualization, 3D-rendering of the obtained surfaces using QGIS software [164] is also shown in Fig.4-4c, Fig.4-4f. It can be seen that the topographic surface generated using the method is rather smooth and without any contour ghosting or artifacts.



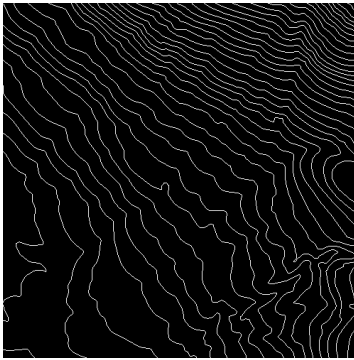
(a)



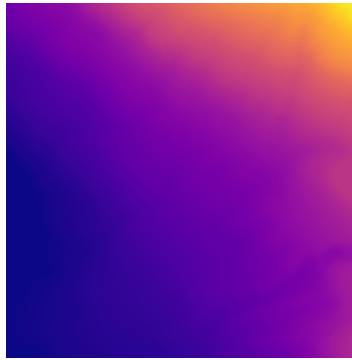
(b)



(c)



(d)



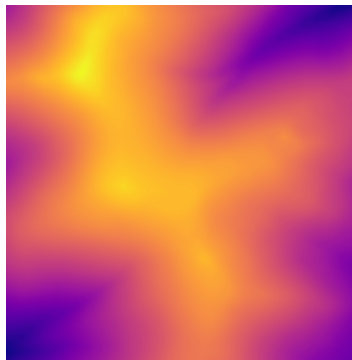
(e)



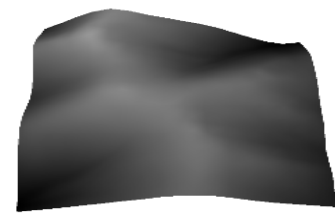
(f)



(g)



(h)



(i)

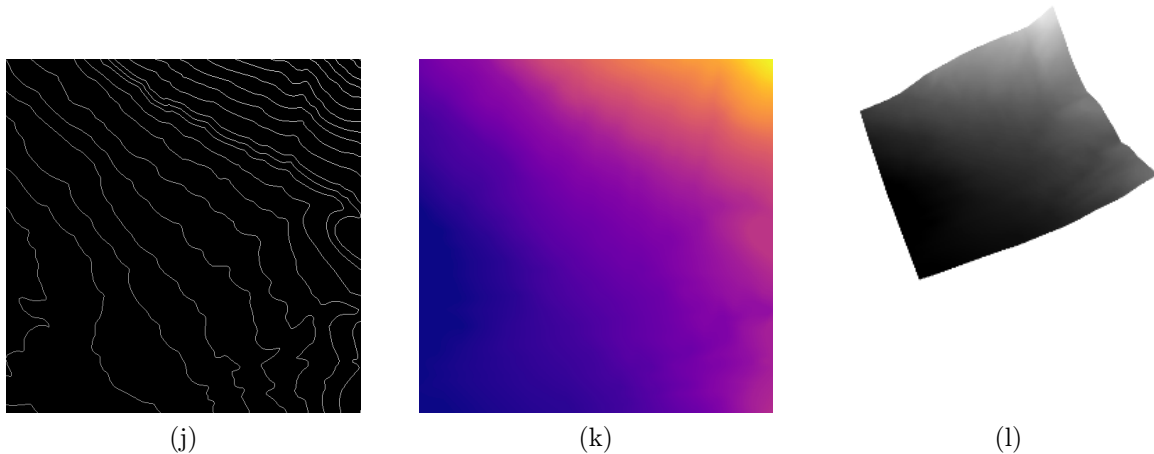


Figure 4-4: (a) Given input set of contours “Zone A”; (b) computed topographic surface from (a) using the proposed method; (c) 3D rendering of the surface in (b); (d) given input set of contours “Zone B”; (e) computed topographic surface from (b) using the proposed method; (f) 3D rendering of the surface obtained in (d); (g) the set of test contours of contour interval 40 meters obtained from (a) by skipping alternate contours  $C_i$  from input contours; (h) and (i) are corresponding computed topographic surface and 3D rendering of the surface respectively using the proposed method; (j) the set of test contours by skipping alternate contours  $C_i$  from input contours “Zone B” (b); (k),(l) are respective interpolated topographic surface and it’s the 3D view from (j).

#### 4.4.2 Validation of the Method

Since the available contour maps do not have any ground truth data to validate with, for validation of the quality of generated intermediate contours, we created some test instances by skipping random alternate contours from the original contours (Figs.4-4a, Fig.4-4d), resulting in a contour map with 40-meter contour intervals in some areas (see Fig.4-4g, Fig.4-4j). The test

instances where we have the ground truth value, comprise the skipped set of contours and their elevation values. Then, to assess the quality of the interpolated contours using the proposed method, we compare the available ground-truth value of the set of contours with the interpolated contours at the test points using some of the error measures (Fig.4-5). To check the quality of the proposed method, we compute  $IC(C_i, C_{i+2})$  (interpolated contours) with ground truth  $C_{i+1}$  for all possible  $i$  values of available contours. If the comparison yields an acceptable degree of match, in that case, we can conclude that the generation of further levels of intermediate contours will undoubtedly provide a better quality terrain surface from available contours. To compare the original  $C_{i+1}$  with the computed  $C_{i+1}$  obtained from  $IC(C_i, C_{i+2})$ , we generated test cases for Zone A (Fig. 4-4g) and Zone B (Fig. 4-4j) by randomly skipping alternate contours ( $C_{i+1}$ ). This resulted in a contour interval of 40 meters. For instance, if we have three contours  $C_1, C_2, C_3$  with a contour interval of 20 meters, we skip  $C_2$  in the input contour map and take  $C_2$  with its elevation value as the test set. This adjustment makes the input contour map have a 40-meter contour interval, which is then used for testing the accuracy of the

predicted values at the test contours.

From each of the test sets, by comparing the given  $C_{i+1}$  and  $IC(C_i, C_{i+2})$ , using the proposed method, we discovered a significant resemblance for the interpolated intermediate contours. Fig.4-6a and Fig.4-6b depict a portion of the test set of contours that illustrates the visual representation of interpolated 1st-level intermediate contours by superimposing the computed intermediate contours ( $IC(C_i, C_{i+2})$ ), blue in color with the ground truth contour  $C_{i+1}$ , red in color. From the superimposition of computed and original contours (refer to Fig.4-6a,4-6b), it can be observed that there is a small difference between the actual and interpolated contours because of the changes in the shape of the contours and the absence of corresponding contours in the test cases. From the visualization, one can assume that the proposed method interpolated a quality of intermediate contours.

Further, the Root Mean Square Error (RMSE) and Mean Absolute Percentage Error (MAPE) were computed for the terrain surface generated from the test set of contours (Figs.4-4h, 4-4k) for both “Zone A” and “Zone B” with the terrain surface



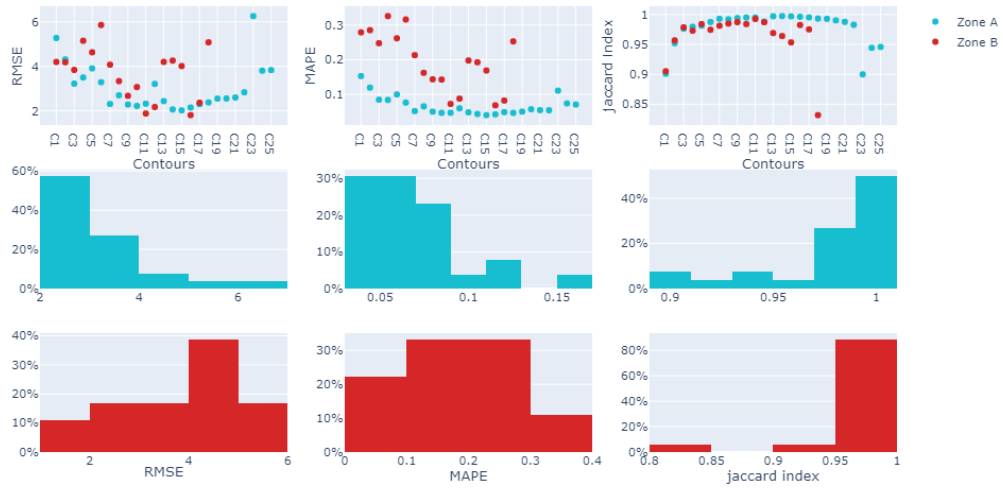


Figure 4-5: The figure depicts the RMSE, MAPE, and Jaccard Index value for each test contour for both case studies “Zone A” and “Zone B”; 2nd and 3rd row plots the percentage-wise distribution of interpolated test contours for RMSE, MAPE, and Jaccard Index values of “Zone A” and “Zone B” respectively, red color represents “Zone A” and blue represents “Zone B”.

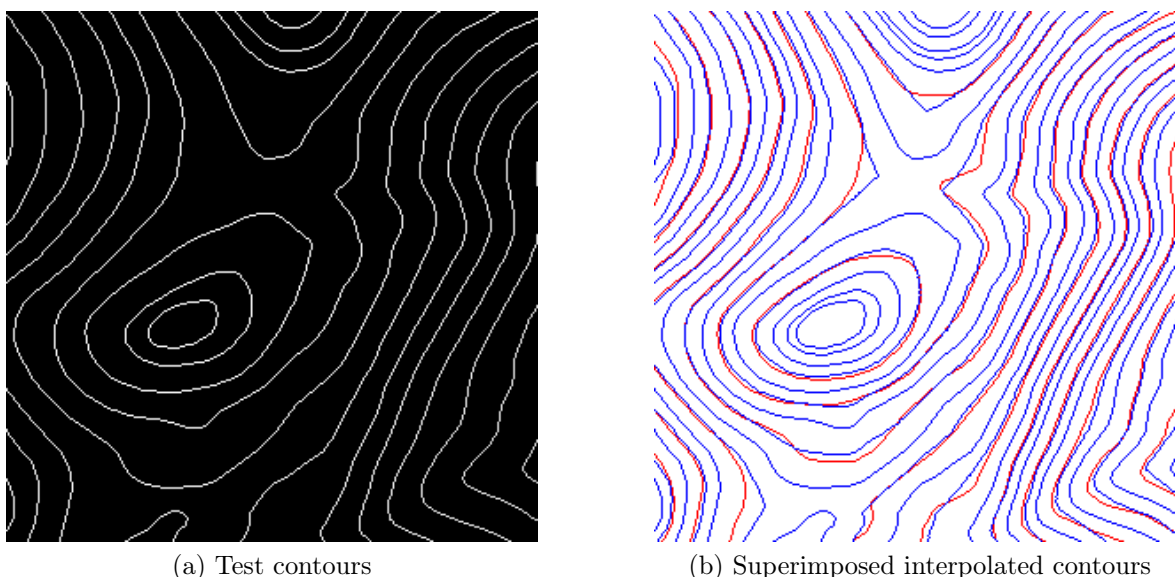


Figure 4-6: (a) Set of test contours of contour interval 40 meters obtained from Zone A; (b) overlapping of interpolated 1st level intermediate contours (blue color) and original contours (red color)

generated from given input set of contours (Figs.4-4b, 4-4e). These error metrics are discussed in detail in Chapter 2. The test case consists of 25 contours for “Zone A” and 18 contours for “Zone B”. The RMSE and MAPE compute the accuracy of the interpolated intermediate contour values at the set of test contours for every set of  $IC(C_i, C_{i+2})$  and  $C_{i+1}$  (see Fig.4-5). The interpolated elevation values that intersect the original contours must have values equal to or approximately equal to the contour labels when measured by RMSE and MAPE. The lesser the RMSE and MAPE value between the actual contour and interpolated contour, the more they are similar and the

more valid the interpolation is. The computed RMSE for all the test contours lies between 2 to 7 for “Zone A” and 1 to 6 for “Zone B” ( refer to Fig4-5). The average RMSE obtained for "Zone A" is 3.04 and for "Zone B" is 3.49 and the maximum MAPE obtained for “Zone A” and “Zone B” are 0.152 and 0.326 respectively. Also, the minimum MAPE is 0.039 and 0.072 respectively for “Zone A” and “Zone B” (Fig.4-5 for RMSE and MAPE for both cases). The maximum and average values for both RMSE and MAPE are reasonably acceptable. We also have analyzed that, for “Zone A” more than 80% of the interpolated contours have RMSE values from 2 to 4 and MAPE is less than 0.1%, which is definitely within an acceptable range. Similarly, for “Zone B”, 80% of interpolated contours have RMSE values less than 5 and 90% have MAPE values less than 0.3% as described in Fig.4-5. It indicates that the interpolated set of test contours ( $IC(C_i, C_{i+2})$ ) matches the original set of contours to a high degree and the error of the proposed interpolation method is within an acceptable range.

This method computes all feasible intermediate contours between two given contours, so the geometric shape of the contours is also essential. Therefore, to validate the quality of

the computed intermediate contours, Hausdorff Distance and Jaccard Index (discussed in Chapter 2) were also computed between  $IC(C_i, C_{i+2})$  and  $C_{i+1}$  for all  $i$  in Table.4.1, Fig.4-5 and Fig.4-7. The interpolation result is considered to be better when the difference between the Hausdorff Distance (HD) of computed contour  $IC(C_i, C_{i+2})$  and  $C_i$  and the Hausdorff Distance (HD) of  $C_i$  and  $C_{i+1}$  is minimal. Furthermore, a Jaccard index value close to 1 between  $IC(C_i, C_{i+2})$  and  $C_{i+1}$  suggests a superior quality of interpolation. Table.4.1 displays HD values of some contours for both case studies “Zone A” and “Zone B”. Fig.4-7 displays HD values for  $IC(C_i, C_{i+2})$  and  $C_i$  as HD interpolated vs. HD values for  $(C_i, C_{i+1})$  as HD actual for all the contours with their elevation values. The degree of matching in "Zone A" is seen to be higher than it is for "Zone B" (Fig.4-7). In Table 4.1, some of the rows  $C_1, C_3, C_{33}, C_{34}$  and  $C_{36}$  show an exact match between Hausdorff Distance values, however, there are exceptions also.

The Jaccard Index, often referred to as a similarity coefficient, measures the similarity between two sample sets. In our scenario, we gauge the resemblance between a given contour ( $C_{i+1}$ ) and the interpolated contour  $IC(C_i, C_{i+2})$  by treating

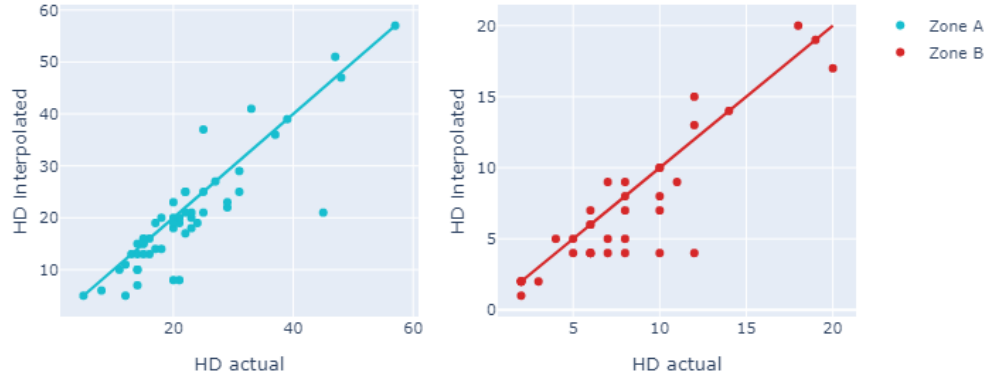


Figure 4-7: The scatter plot of Hausdorff Distance values for  $IC(C_i, C_{i+2})$  and  $C_i$  as HD interpolated vs. Hausdorff Distance values for  $(C_i, C_{i+1})$  as HD actual for all the contours, blue points indicating Zone A contours and red point indicate Zone B contours.

each contour, along with its enclosed contour region pixels, as a set. This approach helps in justifying the shape similarity between the two contours. Jaccard index value ranges from 0 to 1, with 0 denoting no similarity and 1 denoting an exact set. A Jaccard similarity coefficient closer to 1 indicates a higher degree of similarity between two sets. Both case studies have Jaccard index values greater than 0.9 (Fig.4-5). It indicates a high similarity between the interpolated contours and actual input contours. However, in the case of “Zone B”, some of the contours are showing a Jaccard Index value of approximately 0.8, indicating a slight mismatch with the actual contour set.

$C_i$ , Elevation (meter)	HD ( $IC(C_i, C_{i+2}), C_i$ )	HD ( $C_i, C_{i+1}$ )
$C_1$ , 2340	15	15
$C_2$ , 2360	7	14
$C_3$ , 2380	16	16
⋮	⋮	⋮
$C_{49}$ , 3460	13	14
$C_{50}$ , 3480	13	15
$C_{51}$ , 3500	6	8
$C_{52}$ , 3520	5	5
$C_1$ , 1160	6	6
$C_2$ , 1180	4	6
$C_3$ , 1200	6	6
$C_4$ , 1220	5	7
⋮	⋮	⋮
$C_{33}$ , 1840	2	2
$C_{34}$ , 1860	2	2
$C_{35}$ , 1880	1	2
$C_{36}$ , 1900	2	2

Table 4.1: Hausdorff Distance values for “Zone A” and “Zone B”

Except for a few contours, the comprehensive analysis results indicate a high degree of validation for the proposed interpolation method. The overall acceptable range of RMSE, MAPE, and Jaccard Similarity Coefficient, along with the matching HD values of the actual or predicted contours for both case studies, affirm the credibility of the interpolation technique. Some of the discrepancies are caused by the high degree of crenulation in the contours. Additionally, some of the contours contain information about abrupt changes in slope, and when we use those contours as test contours, the method is unable to predict

those changes.

We also conducted a thorough quantitative comparison against existing spatial interpolation techniques. We focused on a segment of “Zone A”, as depicted in Fig.4-4a, to perform this analysis. Using this data, the Digital Elevation Model (DEM) was generated using three methods: Ordinary Kriging [165, 166], Inverse Distance Weighting (IDW) [167], and the TOPOGRID [168, 169] method. Both Root Mean Square Error (RMSE) and Mean Absolute Percentage Error (MAPE) were determined for each method. As mentioned earlier a set of contours, 50% of the contours (selecting every alternate contour), we made the contour map of 40 meters contour interval, and the remaining set of contour pixels are used for validation to compute RMSE and MAPE. Subsequently, the result obtained is compared to the interpolated pixel values produced by each method. The results were then compared to those of our proposed method. For a detailed comparison, please refer to Table 4.2.

Table 4.2 provides a comparison of the performance of four different interpolation methods: Ordinary Kriging [165, 166], Inverse Distance Weighting (IDW) [167], TOPOGRID [168, 169], and the Proposed Method. The performance of each

Table 4.2: Result of Applying Different Methods

Method	RMSE	MAPE
Ordinary Kriging [165, 166]	3.61	0.09
IDW [167]	8.71	0.24
TOPOGRID [168, 169]	3.40*	–
Proposed Method	<b>3.33</b>	<b>0.08</b>

**Remark:** \* indicates data not available.

method is evaluated using two metrics: the Root Mean Square Error (RMSE) and the Mean Absolute Percentage Error (MAPE). The obtained RMSE and MAPE of the IDW method, indicate the lower accuracy of the interpolated values among the other methods presented. Table 4.2 also highlights that the Proposed Method has the lowest RMSE of 3.33 and a MAPE of 0.08 indicating its compelling performance. Although the Ordinary Kriging and TOPOGRID methods have similar accuracy, both methods are complicated and require a lot of computation. Ordinary Kriging faces challenges with larger datasets due to its need to store extensive distance pairings for each grid value. This requirement can sometimes strain computational resources. In contrast, the proposed method strategically confines the computation of intermediate contours to the region between two specified contours (inter-contour space), deliberately omitting the elevation values of pixels from alternate contours. While capturing all available contour information, this com-



putational approach effectively simplifies the process, thereby making it notably beneficial for efficient parallel computation due to its intrinsically localized focus. This entire approach can be extended to other contexts of geosciences that include the generation of high spatial resolution stratigraphic sequences, tree-ring structures, gravity, magnetic, seismological, and resistivity profiles, and contours. This list also includes all those contours such as isotherms, isohyets, etc.

## **4.5 Conclusion**

Interpolation of intermediate contours from existing sparse contour maps is a challenging task in the field of geospatial visualization. Maximum possible recursive intermediate contour interpolation via computing the median elevation region is a way to achieve visualization of the continuous surface from a contour map. Our proposed method describes the spatial relationship between the contour regions and gives a simplification of the original problem in terms of sets interpolation based on different categories. The categorization is also done between different TERs and their subsets as source-set and target-set based on the logical relationship.

From the result section, it can be seen how the transition takes place from the source elevation region to target elevations and ends up creating an intermediate contour using the mathematical morphological gradient. Results have been shown in synthetic data of contours at the different spatial locations, and also in contour maps taken from a real topographic map of Mt. Washington, NH. Further, the method is evaluated quantitatively by calculating the RMSE (Root Mean Square Error) and MAPE (Mean Absolute Percentage Error) using a set of test contours of a 40-meter contour interval derived from input contours. To validate how the proposed approach retains the morphological attributes of a contour, we also analyzed by computing the Jaccard Similarity coefficient and Hausdorff Distance between interpolated test contours and given original contours as ground truth data. The proposed method has also been compared to existing methods such as ordinary Kriging, IDW, and TOPOGRID. The results highlight that the proposed method delivers improved accuracy over these other methods while maintaining simpler computation and offering a new way compared to point-wise traditional interpolation algorithms that sometimes fail to preserve the spatial accuracy of

the contours or to preserve that computation becomes expensive. The proposed framework provides valuable insight into the spatial visualization of discrete contour maps. However, in this chapter, we only consider this framework on contour maps, assuming that all contours run roughly parallel to each other. As a result, the errors appear to be high in some cases, and because we skipped alternate contours for testing the method, the slope information is also altered. However, the result is an acceptable smooth and artifact-free surface. Future work will explore how this framework can be applied to other logical relationships and situations involving spatial interpolation, as well as the parallelization of intermediate contour computations.



# Chapter 5

## Adapting Morphological Operators for Multivariate Data Processing

### 5.1 Introduction

As the need to handle multivariate images continues to grow, efforts to expand the capabilities of Mathematical Morphology (MM) to support these types of data have become increasingly active. The success of using univariate morphological operators in various fields of image processing and sometimes in multivariate data also is the motivation behind this. The original mathematical morphology (MM) framework introduced by Matheron [58] and Serra [60, 63] was designed primarily for binary image processing, employing fundamental operations like dilation and erosion rooted in the geometric measure theory of Minkowski and Hadwiger [61, 62]. As the need arose

to handle gray-scale images, various extensions of binary MM emerged. One notable extension, spearheaded by Serra and Sternberg [63, 64], utilized the principles of complete lattice to form a robust mathematical foundation for understanding morphological operations in the gray-scale domain. Additionally, the introduction of fuzzy set theory [69] led to the development of fuzzy MM [67, 68, 70–74, 170], offering another avenue for extending gray-scale MM. The generalized fuzzy MM, known as L-fuzzy MM where L can be any value set of an image as long as it can be equipped with a complete lattice structure [75]. Nachtegael et al. discussed the application of L-fuzzy MM to interval-valued images in [67, 75], demonstrating how morphological operators such as dilations and erosions can be defined using structuring elements (SEs). Detailed foundational principles, such as those based on complete lattices and also based on fuzzy sets, providing a solid mathematical basis for understanding morphological operations are discussed and compared in these articles [67, 68].

MM, primarily defined for single-band images, e.g. binary and gray-scale, uses infimum and supremum operators to detect pixel extremes within the SE window (as discussed in Chapter

2). Thus, expanding MM operators to multiband images such as multi-spectral and hyperspectral images, in which each pixel is represented as a pixel vector, mainly depends on the scheme for ordering the pixel vectors and finding the extrema of pixel vectors within the neighborhood of the SE window. In this chapter, we propose a novel weighted vector ordering scheme. This scheme considers both the spectral signature and the spatial correlation between pixel vector elements using dilation distance during the ranking process. Additionally, the ranking of pixel vectors is used to define the supremum and infimum. The proposed vector ordering scheme defines the ordering scheme of pixel vectors to extend scalar mathematical morphology (MM) operators to multiband images (the MM operators on multiband images are termed as multi-channel MM operators). The motivation behind this work is to introduce a vector ordering scheme that can identify the infimum and supremum among pixel vectors within the neighborhood of the structuring element (SE). These enhanced multivariate MM operators are then used to compute morphological profiles for feature extraction, which are subsequently validated by the accuracy obtained in classifying hyperspectral datasets using Support Vector Ma-

chines (SVMs) [135]. Experiments demonstrate improved classification rates with this proposed multi-channel MM approach.

## 5.2 Mathematical Morphology in Multivariate Data

Morphological operators, a powerful image analysis tool, has been fully developed for binary and grayscale images in the present day. To make it compatible with multiband images, it is crucial to establish a method for determining the extrema of pixel vectors. However, creating an unambiguous ordering process for vectors remains a challenge, unlike the straightforward case with the scalars. If a suitable vector ordering scheme can be given, then the MM operator Dilation ( $\delta_B$ ) and Erosion ( $\varepsilon_B$ ), easily can be defined in multivariate data. According to Brannet [171], the existing vector ordering schemes are Marginal Ordering (M-Order), Conditional Ordering (C-ordering), Partial Ordering (P-ordering) and Reduced Ordering (R-ordering). Given two vectors  $v = (v_1, v_2, \dots, v_{nv})$  and  $v' = (v'_1, v'_2, \dots, v'_{nv})$ , different ordering strategy are discussed below:

- Marginal Ordering: Also known as univariate ordering or



component-wise ordering where each component of the vector is considered independently. Given two vector  $v = (v_1, v_2, \dots, v_{nv})$  and  $v' = (v'_1, v'_2, \dots, v'_{nv})$ , marginal ordering is defined as:

$$\forall v, v' \in \mathbb{R}^n, v \leq v' \Leftrightarrow \forall z \in \{1, \dots, nv\}, v_z \leq v'_z$$

In the context of multiband image analysis, each component of a pixel vector corresponds to a band in the image.

- **Conditional Ordering:** In this ordering, vectors are ordered by marginal components selected sequentially under different conditions, while components of the vector that are not actively involved or considered during the ordering process are listed based on their ranked counterparts. Lexicographical order is an example of C-ordering, using all available components. C-orderings work best when it is possible to determine the priority of the image channels/bands. It can be defined as:

$$\forall v, v' \in \mathbb{R}^n, v \leq_L v' \Leftrightarrow \exists z \in \{1, \dots, nv\},$$

$$(\forall z' < z, v_{z'} = v'_{z'}) \wedge (v_z \leq v'_z)$$

- **P-ordering:** This method essentially utilizes pre-orderings

to divide the given vectors into equivalent groups, based on criteria such as order, rank, or extremity [172]. These are typically geometric in approach and effectively account for the interrelationships among the components.

- **R-Ordering:** In this approach, vectors are initially transformed into scalar values and subsequently ranked based on their scalar order. Further examples of R-orderings involve categorizing them as distance or projection orderings [26]. For instance, in an R-ordering on  $\mathbb{R}^n$  the process begins by defining a transformation  $g : \mathbb{R}^n \rightarrow \mathbb{R}$  then ordered according to the scalar order of their projection onto  $\mathbb{R}$  by  $g$ :

$$\forall v, v' \in \mathbb{R}^n, v \leq v' \Leftrightarrow g(v) \leq g(v')$$

### 5.3 Related Work

In existing works, MM is often extended to multiband image data by decomposing multiband images into mono-band images. It is applied independently on each band of multiband images. The outcomes are then assembled into a single dataset [101]. Although this marginal strategy is simple and straightforward due to its inherent nature, creates new pixel

vectors not found in the original image and loses band correlations, which are major drawbacks [171]. To circumvent the issue of losing band correlation, a dimensionality reduction transformation like Principal Component Analysis (PCA) [100, 173] is often applied to the original multiband image before undergoing the marginal treatment. This process aims to de-correlate the image bands and mitigate the first problem inherent in the M-ordering strategy. To mitigate this drawback, non-scalar morphological approaches are used, processing the multiband image as a single, cohesive data unit simultaneously. To view the multiband image as a single entity and to implement the MM operators, conditional ordering is also used as mentioned before, where some bands are given higher priority than others [174]. Thus using C-ordering, two vectors are compared based on their prioritized band. Two vectors are equal in C-ordering if every component's value is equal. The Lexicographic Ordering Strategy (L-ordering strategy), a well-known variation of the C-ordering strategy, adopts a principle similar to how words are alphabetically ordered. Lexicographic Ordering Strategy (L-ordering) is one of the most commonly used approaches in multi-channel Mathematical Morphology (MM)

due to its capability of preserving vectors and enabling them to follow a total order relation between compared vectors [174]. This means there are no indecisive cases between two vectors, with the only situation of equality occurring when all the components of compared vectors are equal. The primary sorting of vectors is based on the first image band, and subsequent bands are used to resolve any indecisive cases from the previous sorting [174]. Consequently, it is best suited for cases where the first image bands contain the most critical information [175]. Such situations might not naturally occur in multiband images. Still, they can be achieved through projection techniques, such as Principal Component Analysis (PCA), which concentrates image information into the first bands. Angulo [176,177] proposed distance-based and lexicographical-based approaches for extending morphological operators to color images. The L-ordering strategy and its variants have been extensively studied and utilized, as documented in various research papers, including [178–182]. This ordering can be reversed, starting with the last image band and moving gradually to the first band to resolve unresolved cases. The Partial Ordering Strategy (P-ordering) operates by classifying vectors into equivalence groups

based on a certain criterion. This strategy can compare vectors from different groups, but can not compare those that are in the same group [183]. Thus, using the P-ordering strategy a total order relation between vectors cannot be achieved, meaning that some vectors are incomparable [184, 185]. Despite this limitation, P-ordering has been employed in various methods to extend Mathematical Morphology to multiband images, as discussed in the works of Valesco et al. and Aptoula et al. [185–188]. The Reduced Ordering Strategy (R-ordering strategy) involves simplifying vectors into scalar values for easy comparison. This could involve projecting multi-dimensional data onto a one-dimensional plane or measuring the distance from a predefined reference [189, 190]. Once vectors are replaced by associated scalar values, grayscale images are created, which can be directly processed by univariate morphological transformations. However, projection techniques such as PCA often lead to information loss and do not guarantee unique scalar values for each vector. To address this, Velasco et al. [185] introduced a supervised learning framework for reduced vector ordering using kriging and support vector machines, aimed at extending mathematical morphology to hyperspectral images.

However, it can be seen that distance measurement is a more preferred approach, as explored by Plaza et al. [191, 192], Al-Otum et al. and Angulo [176, 193].

## 5.4 Proposed Vector Ordering

This work introduces an approach aimed at enhancing multi-channel mathematical morphology (MM) operators for analyzing multiband images. After gaining insight into the current methods for extending MM operators to multiband images, in this chapter, we propose a vector ordering algorithm that is adapted from both reduced ordering and lexicographic ordering to determine the infimum and supremum of the pixel vectors. The primary objective is to develop a robust vector ordering scheme capable of accurately identifying the minimum and maximum among pixel vectors in the neighborhood within the SE window. Using this infimum and supremum of pixel vectors, we can define the multi-channel dilation and erosion, which are then used to compute the multi-channel morphological profile (MP) for feature extraction of multiband image.

Let  $H$  denote the hyperspectral image with  $nz$  bands. The bands of  $H$  are represented by  $\{f_1, f_2, \dots, f_{nz}\}$  where each  $f_i$  is

a gray-scale image. Let,  $f(x, y)$  and  $f(x', y')$  are two-pixel vectors at pixel coordinate  $(x, y)$  and  $(x', y')$  respectively, where each vector component corresponds to the bands of the image. In the initial phase of our proposed algorithm, we compare,  $f(x, y)$  and  $f(x', y')$  in terms of the weight associated with their respective bands. To define the fundamental morphological operations for such an image, we need to compare the pixel vector  $f(x, y)$  with all other pixel vectors within the window of a given structuring element (SE) based on their modified weighted vectors. This comparison is based on their modified weighted vectors, which provides more understanding of the vector's relationships and differences.

Let's consider,

$$f(x, y) = [f_1(x, y), f_2(x, y), \dots, f_{nz}(x, y)]$$

$$f(x', y') = [f_1(x', y'), f_2(x', y'), \dots, f_{nz}(x', y')]$$

are two pixel vectors at  $(x, y)$  and  $(x', y')$  spatial location.

To compare pixel vectors in multiband images along the  $nz$  bands, we first introduce a weight factor  $W$  for each band  $f_i$  of the image. The weight of a band  $f_i$  is calculated as the cumulative sum of dilation distances between  $f_i$  and all other bands  $f_j$

in the image. The dilation distance is extensively discussed in Chapter 3. Therefore using the definition of dilation distance that is discussed in Chapter 3, the proposed weight ( $W$ ) for  $i^{th}$  band of image  $f$  can be defined as:

$$W(f_i) = w_i = \sum_{j=1}^{nz} \widehat{\Delta}(f_i, f_j) \quad (5.1)$$

where,  $f_i$  represents the  $i^{th}$  band for which the weight is being calculated,  $f_j$  represents all other bands in the image,  $j \in \{1, \dots, nz\}$ ,  $w_i$  is the weight of the  $i^{th}$  Band and  $\widehat{\Delta}$  represents dilation distance as reported in previous Chapter 3.

Thus,  $W(f_i)$  is obtained by the sum of dilation distance scores between  $f_i$  and all other bands  $f_j$  for  $j \in \{1, 2, \dots, nz\}$ .

The weight  $W$  in Eq.5.1 represents the weight of each band present in the pixel vector. Thus using  $W$ , we define a weighted pixel vector  $f'(x, y)$  and  $f'(x', y')$  at  $(x, y)$  and  $(x', y')$  by element-wise multiplication of the weight vector  $W = [w_1, w_2, \dots, w_{nz}]$  with the pixel vector  $f(x, y) = [f_1(x, y), f_2(x, y), \dots, f_{nz}(x, y)]$  and  $f(x', y') = [f_1(x', y'), f_2(x', y'), \dots, f_{nz}(x', y')]$  as follows:



$$\begin{aligned}
f'(x, y) &= [w_1 \cdot f_1(x, y), w_2 \cdot f_2(x, y), \dots, w_n \cdot f_{nz}(x, y)] \\
f'(x', y') &= [w_1 \cdot f_1(x', y'), w_2 \cdot f_2(x', y'), \dots, w_n \cdot f_{nz}(x', y')]
\end{aligned} \tag{5.2}$$

The comparison between two pixel vectors  $f(x, y)$  and  $f(x', y')$  can now be expressed in terms of the weighted pixel vectors  $f'(x, y)$  and  $f'(x', y')$  as follows:

$$f(x, y) > f(x', y'), \quad \text{if} \quad \sum_{i=1}^{nz} f'_i(x, y) > \sum_{i=1}^{nz} f'_i(x', y') \tag{5.3}$$

Thus, we can compare each vector within the neighborhood lying under the SE (throughout this chapter we are considering a flat square structuring element). However, even with this ordering, there is no guarantee that two pixel vectors  $f(x, y)$  and  $f(x', y')$  are equal if  $\sum_{i=1}^{nz} f'_i(x, y) = \sum_{i=1}^{nz} f'_i(x', y')$  (discussed in Eq.5.1 and Eq.5.3). For instance, consider two vectors  $v_1 = [6, 5, 1]$  and  $v_2 = [2, 1, 5]$ , along with their corresponding band weights  $W = [2, 3, 5]$ . Consequently, the weighted vectors become  $v'_1 = [12, 15, 5]$  and  $v'_2 = [4, 3, 25]$ . Interestingly, despite having the equal sum of the elements in the weighted vectors  $v'_1$  and  $v'_2$ , this example illustrates that both vectors are inher-

ently distinct. So to handle this kind of situation, an additional ordering strategy is employed. In this approach, a conditional ordering scheme is recommended, where a band prioritization factor is utilized to assign priority values to every band of the N-dimensional image. In this approach, The ranking of the bands is based on the weights assigned to them according to the Eq.5.1. The bands with high weight values are more prioritized in this process. We can express the priority of the band as:

$$f_p = \operatorname{argmax}(W)$$

where  $f_p$  denotes the band with the highest priority based on the maximum weight.

By employing this supplementary conditional ordering strategy, pixel vectors that are initially incomparable are now arranged according to the scalar value of their highest weighted component. If two vectors have identical values for the highest weighted component, they are subsequently ordered based on the next highest weighted component. This process continues for successive components. This approach ensures a complete ordering structure to resolve the incomparability between two vectors. For instance, consider the above mentioned example

vectors  $v_1 = [6, 5, 1]$  and  $v_2 = [2, 1, 5]$ , along with their corresponding band weights  $W = [2, 3, 5]$ . To compare  $v_1$  and  $v_2$ , we Compare the third components: 5 (from  $v_1'$ ) and 25 (from  $v_2'$ ). Since  $5 < 25$ , we conclude  $v_1 < v_2$ . For example, if the third components were both 5, we would compare 15 (from  $v_1'$ ) and 3 (from  $v_2'$ ). If we order the bands according to their assigned weights, where the highest weight signifies the highest priority, We can define a priority vector  $W'$  which is in decreasing order of the weights in  $W$ . It is denoted as:

$$W' = [w'_1, w'_2, \dots, w'_{nz}]$$

$W'$  is in decreasing order of of weights in  $W$ , i.e.  $w'_1 \geq w'_2, \geq \dots, \geq w'_{nz}$ , also  $w'_k = w_j$ , where  $w'_k \in W'$  and  $w_j \in W$ .  $w'_k = w_j$  means that the  $j^{th}$  band has  $k^{th}$  highest weight.

With the priority vector  $W'$ , the ordering strategy can be formulated as:

$$\begin{aligned}
 f(x, y) > f(x', y'), \quad \text{if } \exists k \in \{1, 2, \dots, nz\} \text{ such that,} \\
 (w'_k = w_j) \wedge (f'_i(x, y) = f'_i(x', y')) \wedge (f'_j(x, y) > f'_j(x', y')) \\
 \forall i < k
 \end{aligned}
 \tag{5.4}$$

Similarly, if  $f(x, y) < f(x', y')$  can be decided:

$$\begin{aligned}
 & f(x, y) < f(x', y'), \quad \text{if } \exists k \in \{1, 2, \dots, nz\} \text{ such that} \\
 & (w'_k = w_j) \wedge (f'_i(x, y) = f'_i(x', y')) \wedge (f'_j(x, y) < f'_j(x', y')) \\
 & \forall i < k
 \end{aligned} \tag{5.5}$$

If, at all the components of  $f'(x, y)$  and  $f'(x', y')$  has equal value, then  $f(x, y) = f(x', y')$ .  $f'(x, y)$  and  $f'(x', y')$  are already defined in Eq.5.2.

This equation gives a tie-breaking conditional strategy that helps to decide the order between two pixel vectors when it is equal according to the Eq.5.3. This equation signifies that, the  $k^{th}$  priority band is actually the  $j^{th}$  band in pixel vector according to its weight. So, if the  $j^{th}$  component of  $f'(x, y) > f'(x', y')$ , and all the other components of higher priority than  $k$  are equal, then  $f(x, y) > f(x', y')$ . Otherwise, if the  $j^{th}$  component of  $f'(x, y) < f'(x', y')$ , and all the other components of higher priority than  $k$  are equal, then  $f(x, y) < f(x', y')$ . On the other hand, if all the components of  $f'(x, y)$  and  $f'(x', y')$  has equal value, then  $f(x, y) = f(x', y')$ .

According to the vector ordering strategy proposed, we can

now define the supremum and infimum of an arbitrary set of vectors. Given a set of vectors  $S = \{s_1, s_2, \dots, s_{ns}\}$ , where  $ns$  is the number of vectors in the set. So the infimum and supremum are the vectors that are lesser than and greater than all other vectors in the set respectively according to the vector ordering strategy proposed.

$$\text{Sup}(S) = s_i \text{ such that } s_j \leq_h s_i, \quad \forall j \neq i \text{ and } s_j \in S \quad (5.6)$$

$$\text{Inf}(S) = s_i \text{ such that } s_i \leq_h s_j, \quad \forall j \neq i \text{ and } s_j \in S \quad (5.7)$$

In the above equations,  $S$  represents the set of vectors, and  $s_i$  represents a vector in the set  $S$ .  $\leq_h$  denotes the proposed vector ordering strategy. These equations define the supremum ( $\text{Sup}(S)$ ) and infimum ( $\text{Inf}(S)$ ) of the set  $S$  based on the proposed vector ordering strategy. The supremum of  $S$  is the smallest upper bound of  $S$  and the infimum of  $S$  is the largest lower bound of  $S$ . Thus using the proposed vector ordering strategy ( $\leq_h$ ), the basic MM operator dilation and erosion can be expanded to multivariate data.

Based on the definition given in Eq.2.4, Eq.2.3, and our proposed supremum and infimum, the extended multivariate dilation and erosion on discrete space  $\mathbb{Z}^2$  can be defined as:

$$\delta'_B(f) = (f \oplus B)(x, y) = \text{Sup}_{c,d \in B} \{f(x + c, y + d)\}, (x, y) \in \mathbb{Z}^2$$

where  $\delta'_B(f)$  is the extended dilation on multivariate image  $f$  by flat structuring element  $B$ . The  $B \subset \mathbb{Z}^2$  denotes the set of discrete spatial coordinates associated with pixels lying within the neighborhood defined by a flat structuring element (SE)  $B$ . Also, in this case, we are considering a symmetric structuring element. Similarly, the extended erosion  $\varepsilon'_B(f)$  can be defined as:

$$\varepsilon'_B(f) = (f \ominus B)(x, y) = \text{Inf}_{c,d \in B} \{f(x + c, y + d)\}, (x, y) \in \mathbb{Z}^2$$

Based on the simple definitions above, the flat extended dilation and erosion of  $f$  by  $B$  is based on the selection of the B-neighborhood pixel vector which is supremum and infimum within the pixel vectors of B-neighborhood respectively.

Since we already know that the MM operator can be ap-

plied only to gray-scale images. Thus, by employing this framework, the extension of MM to multiband images especially in hyperspectral images is achieved, which can directly be used to compute features of hyperspectral images for further processing. Using the definitions of supremum and infimum given in Eq.5.6 and Eq.5.7, the multi-channel morphological profiles (Morphological profile is explained in Chapter 2) are computed, which are used as feature vectors for support vector machines for supervised classification of hyperspectral data. Since the extended dilation and erosion for multivariate data are defined using the above equations, the multi-channel morphological profiles(MMP) can be computed by simply replacing the classic gray-scale dilation and erosion in Eq.2.9 to Eq.2.14 by the defined extended dilation and erosion on multivariate data.

## 5.5 Result and Analysis

The application of our proposed weighted vector ordering strategy on the Pavia University hyperspectral image dataset, as detailed in Chapter 3, provided detailed significant insights. This dataset, consisting of nine classes and 115 bands, served as an ideal real test case for our method. For analysis purposes, we

computed a multi-channel morphological profile (MMP) that was subsequently used for land cover classification. We used the Support Vector Machine (SVM) [52] method for the classification task. Notably, the utilization of the MMP-based features in the SVM classifier exhibited a promising performance. To further evaluate our proposed method, we compared the classification results obtained using our strategy against two other widely accepted vector ordering strategies 1) Lexicographic ordering with increasing priority, 2) Lexicographic ordering with decreasing priority with Multi-channel Morphological Profile. A detailed qualitative and quantitative analysis is provided in this section.

A unique aspect of our approach was assigning a priority to each of the bands based on the dilation distance( explained in Chapter 3) computed for each band to compare with other pixel vectors as mentioned in Eq.5.1 and Eq.5.3. Using the dilation distance value as a priority, how the available bands are prioritized, is explored in this experiment. We have computed the average intensity values of pixels for each class available in the ground truth data and the priority values of each band. We have selected some of the priority values and their correspond-



ing bands for better visibility. The plot of the priority of bands vs. the average intensity of pixels for each class is shown in Fig.5-1. The priority of the bands is written on the dotted line as P: value. As we can recall from Chapter 3, dilation distance can capture the spatial distance and it is useful to separate the class objects. This concept helped us to assign the priority value of each band. As we can see in Fig.5-1, those bands are set higher priority with significant separability from each class. Those bands, in which even though one class is quite separable from other classes, the others are not following that property are assigned a medium level of priority as we can see one band in between the 80th and 100th band. This experiment strengthens our intuition that the dilation distance-based priority value is a good choice for priority-based vector ordering.

To visualize and analyze the distinction between multi-channel morphological operations and univariate morphological operations, we also implemented the proposed vector ordering-based multi-channel dilation and erosion on the dataset. Also, we have selected the 5th band of the image cube to perform the mono-channel grayscale dilation and erosion, due to its specific spectral characteristics.

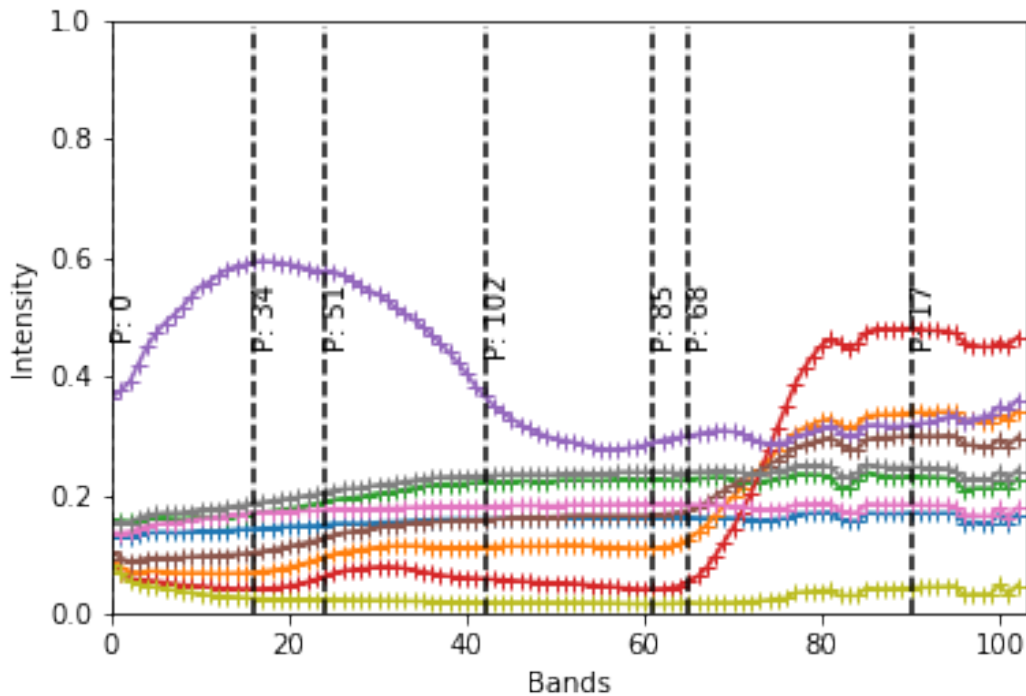


Figure 5-1: Plot of band priority versus average intensity for each class, demonstrating the efficiency of band priority assignment. The plot illustrates how the prioritization of bands effectively captures the divergence of class information contained within each band. The priority of bands is shown in the dotted line and as P: value, e.g. P:51 is the 51st priority band. Each curve represents a unique class, showing the relationship between the assigned band priority and its corresponding average intensity. This indicates how successfully the band priority assignment discerns the different classes based on their spectral properties.

For visual analysis, of how these multi-channel Morphological operation results are different from univariate morphological operations, we applied the proposed vector ordering strategy to compute multi-channel dilation and erosion on the dataset. Also, we have selected the 5th band of the image cube to perform the mono-channel grayscale dilation and erosion on that band. The obtained dilated and eroded images are shown in Fig.5-2a to Fig.5-2e with the base image at the 5th band. To demonstrate the proposed approach, we consider 3x3 flat Structuring element  $B$  throughout the process. The result of applying multi-channel dilation and erosion on the image using structuring element  $B$  is an image cube with the same dimension as the original data. In the resultant data cube, every pixel vector is replaced by its neighboring supremum or infimum pixel vector as defined in Eq.5.6 and Eq.5.7. Fig.5-2c the base image at 5th band of the image dataset, Fig.5-2a and Fig.5-2b shows the 5th resultant band obtained after applying multi-channel erosion and dilation using the proposed method at the whole image cube and Fig.5-2d and Fig.5-2e are resultant image obtained after applying mono-channel grayscale dilation ( $\delta_B$ ) and erosion ( $\varepsilon_B$ ). It can be seen in Fig.5-2a and Fig.5-2b that multi-

channel dilation ( $\delta'_B$ ) and erosion ( $\varepsilon'_B$ ) expand and shrink particular classes in that bands, especially the "metal-sheet" class (that is more visible), whereas, the mono-channel dilation erosion (Fig.5-2d, Fig.5-2e) tends to expand the brighter objects and shrink the darker objects available only in that band irrespective of the spectral purity of that band. For a quantitative evaluation of the proposed method, we consider the evaluation using a classification based on Support Vector Machine(SVM) by computing mult-channel MP. We split the data into the train(70%) and test(30%) data sets. To evaluate the proposed vector ordering method, we computed the multi-channel MP on the dataset and performed SVM classification on that. As we have already discussed in Chapter 2 using Eq.2.14 that morphological profile (MP) is dependent on the number of opening and number closing cycles we use. Therefore we have experimented to show how SVM classification accuracy changes according to the number of opening and closing cycles we use for computing MP, which eventually generates the feature vectors for SVM. Fig.5-3, shows the accuracy plot vs. the number of opening and closing cycles used to compute MP in the Pavia University dataset. Observation is drawn from this experiment that the

optimal accuracy is coming from the number of opening and closing cycles around 15 to 20.

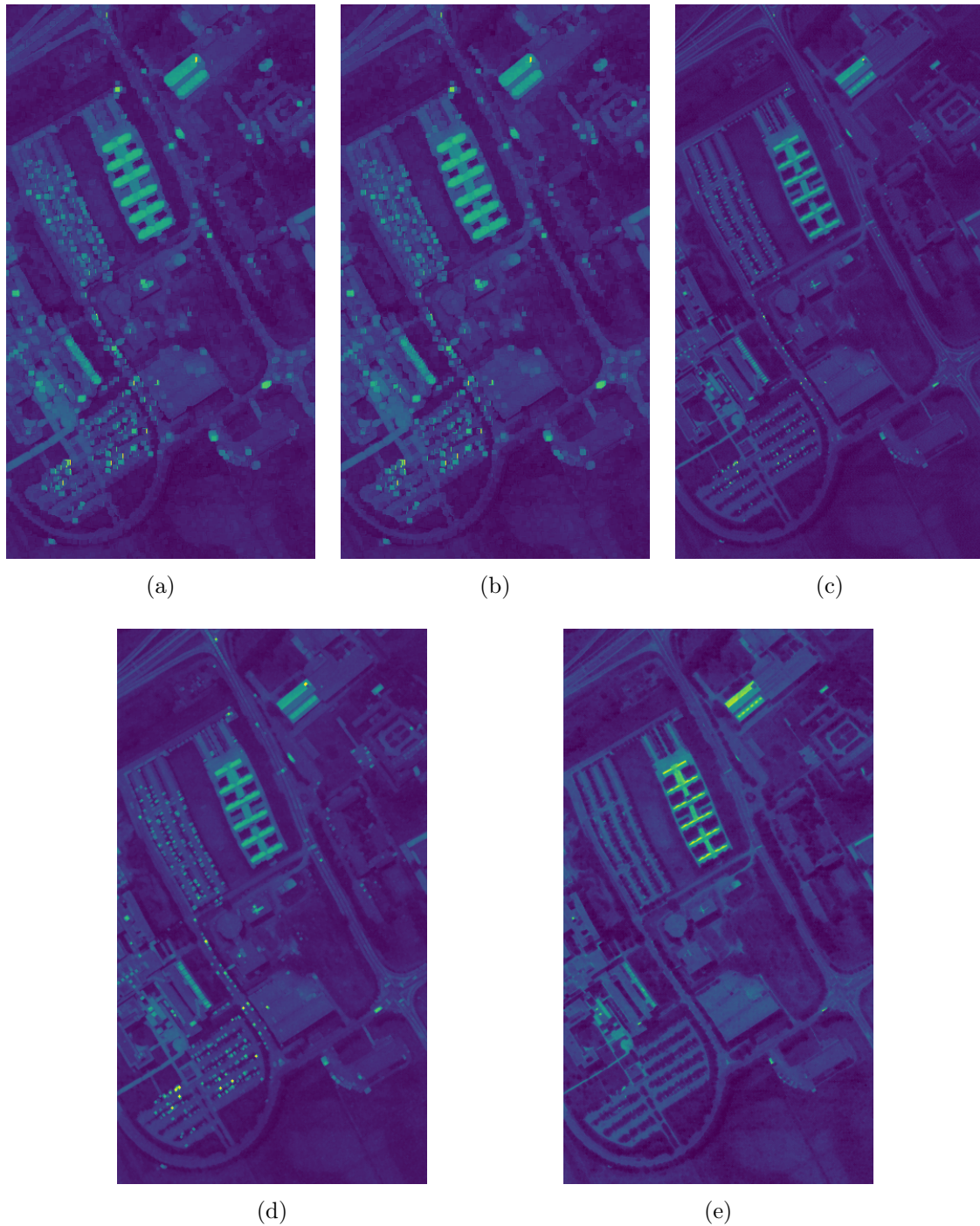


Figure 5-2: Comparative effects of dilation and erosion operations on multi-channel and mono channel data. (a) Result of the erosion operation on the multi-channel data. (b) Result of the dilation operation on the multi-channel data. (c) The base image represents the original data at the 5th band. (d) Result of the dilation operation on the mono channel data. (e) Result of the erosion operation on the mono channel data.

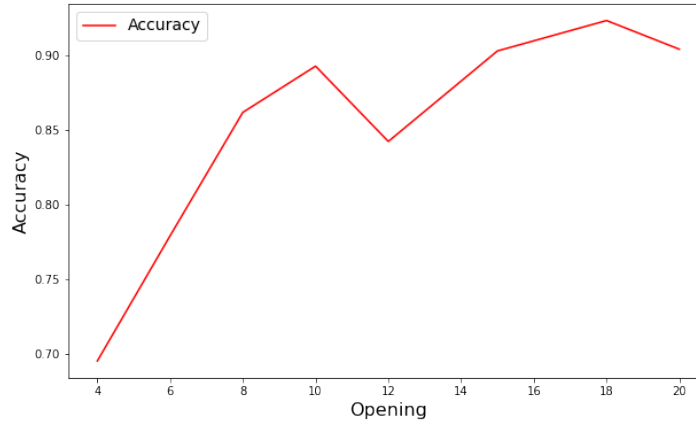


Figure 5-3: Classification accuracy vs. the number of opening and closing cycles (as discussed in Eq.2.14) used to compute MP.

Therefore we have chosen 18 numbers of cycles to use for further experiments. This slightly gives the idea about the shape and size of the spatial objects present in the Pavia University data. Other optimal hyperparameters for SVM are chosen using a five-fold cross-validation method. The classification accuracy(SVM accuracy) would indicate how well the vector ordering method is working. A detailed SVM classification accuracy in terms of precision, Recall, F1-score and accuracy of each class and Overall Accuracy(OA) of Pavia University using the proposed vector ordering method to compute Multi-channel MP is given in Table.5.1. The OA obtained is 92.30 which indicates a significant classification capacity.

SVM accuracy is chosen using a five-fold cross-validation

Class	Precision	Recall	F1-Score	Accuracy
1	81.67	89.12	85.23	89.20
2	92.47	80.66	86.16	81.14
3	89.18	93.47	91.28	93.47
4	93.73	86.39	89.91	86.41
5	100.00	99.65	99.82	99.46
6	92.50	93.17	92.83	93.20
7	92.43	98.65	95.44	98.7
8	90.75	89.47	90.11	89.51
9	99.63	100.00	99.82	100.00
OA	-	-	-	92.30

Table 5.1: Classification metrics for proposed method

method. The classification accuracy(SVM accuracy) would indicate how well the vector ordering method is working. A detailed SVM classification accuracy in terms of precision, Recall, F1-score, and accuracy of each class and Overall Accuracy(OA) of Pavia University using the proposed vector ordering method to compute multi-channel MP is given in Table.5.1. The OA obtained is 92.30% which indicates a significant classification capacity.

For a comparative analysis, we computed the classification result using two other widely used vector ordering methods, Lexicographic Ordering with decreasing priority(L-ordering (ascending priority)) and Lexicographic ordering with increasing priority (L-ordering (descending priority)). These two methods are used to compute the multi-channel MP in the Pavia



University multiband image. For comparison, we have used two metrics Overall Accuracy(OA) and Kappa coefficient(KC). A summary of results for all three vector ordering methods in terms of OA and KC is given in Table. 5.2. The corresponding classification map for all three methods along with the given ground truth map is also shown in Fig.5-4 for visual comparison. In Fig.5-4, Fig.5-4a shows the ground truth of the dataset, Fig.5-4b is the classification map obtained by computing multi-channel MP using the proposed vector ordering strategy, Fig.5-4c is the classification map obtained by computing multi-channel MP using Lexicographic- with increasing priority vector ordering strategy and Fig.5-4d is the classification map obtained by computing multi-channel MP using Lexicographic-with decreasing priority vector ordering strategy.

Observe that the classification accuracy obtained using the proposed vector ordering strategy to compute multi-channel MP outperforms the classification accuracy, where we used Lexicographic ordering to compute multi-channel MP. This summary of results can be comprehended as our selection of priority and weight for each band is relevant towards the computing of multi-channel Morphological operation.

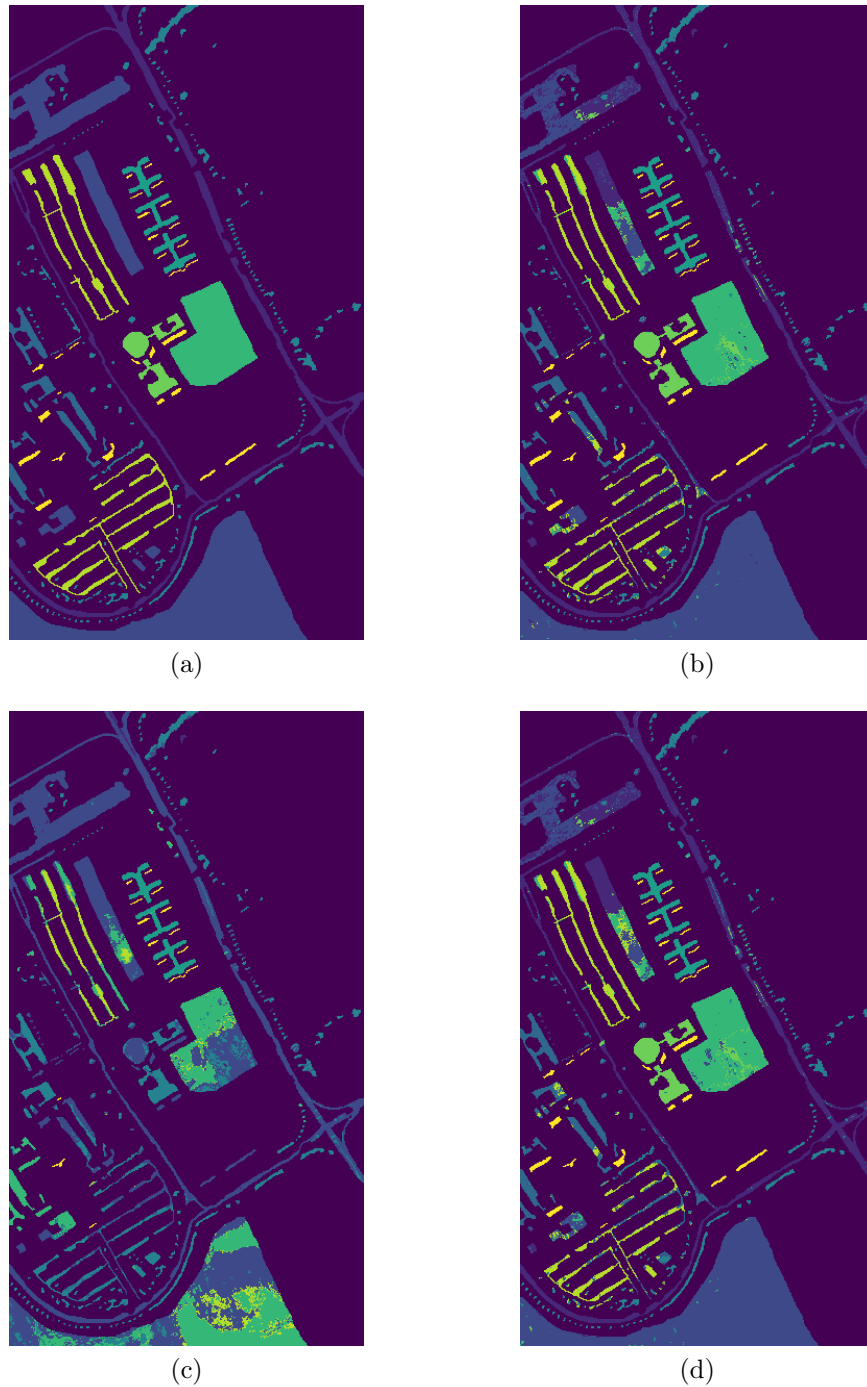


Figure 5-4: (a) Ground-truth of the dataset (b) classification map obtained by computing multi-channel MP using the proposed vector ordering strategy (c) classification map obtained by computing multi-channel MP using Lexicographic- with increasing priority vector ordering strategy,(d) classification map obtained by computing multi-channel MP using Lexicographic- with decreasing priority vector ordering strategy.

---

Method	OA	KC(%)
Proposed vector-ordering method	92.29	91.33
L-ordering(ascending priority)	85.34	81.04
L-ordering (descending priority)	90.52	87.58

Table 5.2: Evaluation using SVM for classification on multi-channel MP

## 5.6 Conclusion

Mathematical morphology (MM) is a crucial non-linear image analysis tool used in object and pattern recognition. Standard MM operators, defined on 2D binary and gray-scale images, based on local minimum or infimum and maximum or supremum. Because of their proven effectiveness in shape-based feature analysis on single-band images, extending these operators to multiband images is an area of significance. However, this task is challenging due to the absence of a predetermined vector ordering. To address this, we propose a new vector ordering method, based on defining a dilation distance weight for each band in multiband images.

Our method has empirically performed better than the existing lexicographic ordering method providing 92.29% SVM classification accuracy. This method is vector preserving while providing a total order relation between compared vectors, making

the results reasonable and justifiable. Moreover, the versatility of the proposed algorithm suggests its potential for usage in other multi-channel morphological operations for multi-channel images. It offers a new, practical approach to image analysis, promising to extend the reach and impact of MM techniques.

# Chapter 6

## Conclusions and Future Work

In conclusion, this thesis focuses on exploring Mathematical Morphology(MM) based nonlinear operator methods and analyzing the spatial features of remote-sensing images, with an emphasis on Hyperspectral images and Digital Elevation Models (DEMs). The research investigated morphological-based interpolation techniques for ordered sets and explored the spatial relationship using MM-based methods. The application of Morphological interpolation to DEMs provided different prospects for its utilization. Also, the proposed methods for extending the MM operator open a new path of exploration. Overall, the findings and methodologies presented in this study provide valuable insights into enhancing the analysis and processing of remotely sensed data.

Having revisited the purpose and goal of this research work,

the following summary of the main findings in this thesis.

- It is demonstrated that the Dilation Distance-based method for band selection can capture spatial distances and identify unique spatial objects. It adds a new viewpoint to Hyperspectral Image analysis using MM-based methods.
- We provide empirical evidence that the MM-based method presents a better strategy for analyzing remote sensing images, especially in dimension reduction.
- Morphological interpolation method proposed in Chapter 4 effectively addresses the challenges in spatial visualization of a continuous surface.
- Further, a spatial relationship and logical relationship are also analyzed between source-target sets.
- Apart from using binary and grayscale MM operators, chapter 5 provides an insight to effectively extend these operators to multiband remotely sensed images directly all at once.
- The obtained empirical results in this research work have proven the capability of Mathematical Morphology in terms of spatial feature analysis of remote sensing data.

---

However, based on the results obtained, it is believed that further research in this area can not only improve the methods but also provide new insights into Mathematical Morphology based tools in image analysis. Some of the future scopes and ideas are briefly mentioned below.

- Selection of suitable preprocessing steps for objects which are spatially disconnected, can improve further these approaches.
- Incorporating MM-based methods into state-of-the-art methods and learning-based methods is one of the important future scopes.
- Using more complex data and an unordered set for median set-based interpolation can provide significant insight and is considered for future work.
- Improvising the weight and priority for vector order is left as future research.
- Also, MM-based methods can be applied to other remotely sensed data for mineral mapping, crater detection, glacier study, etc.





# Bibliography

- [1] B. Tso and P. M. Mather, *Classification methods for remotely sensed data*. Boca Raton: CRC Press, 2009.
- [2] C.-I. Chang, *Hyperspectral data exploitation: theory and applications*. John Wiley & Sons, 2007.
- [3] B. S. D. Sagar, *Mathematical morphology in geomorphology and GISci*. CRC Press, 2013.
- [4] B. Szypuła, “Digital elevation models in geomorphology,” *Hydro-Geomorphology-Models and Trends. InTechOpen, 2017b*, pp. 81–112, 2017.
- [5] J. Campbell and R. Wynne, *Introduction to Remote Sensing, Fifth Edition*. Guilford Publications, 2011.
- [6] P. Gibson and C. Power, *Introductory Remote Sensing: Principles and Concepts*. Routledge, 2000.
- [7] G. Rees, *The Remote Sensing Data Book*. Cambridge University Press, 1999.
- [8] Z. Li, J. Chen, and E. Baltsavias, *Advances in Photogrammetry, Remote Sensing and Spatial Information Sciences: 2008 ISPRS Congress Book*, ser. ISPRS Book Series. CRC Press, 2008.

- [9] F. F. Sabins, Jr, “Remote sensing: Principles and interpretation,” 1 1986.
- [10] G. A. Shaw and H. K. Burke, “Spectral imaging for remote sensing,” *Lincoln laboratory journal*, vol. 14, no. 1, pp. 3–28, 2003.
- [11] A. F. Goetz, B. N. Rock, and L. C. Rowan, “Remote sensing for exploration; an overview,” *Economic Geology*, vol. 78, no. 4, pp. 573–590, 1983.
- [12] S. M. Davis, D. A. Landgrebe, T. L. Phillips, P. H. Swain, R. M. Hoffer, J. C. Lindenlaub, and L. F. Silva, “Remote sensing: the quantitative approach,” *New York*, 1978.
- [13] C. Elachi and J. J. Van Zyl, *Introduction to the physics and techniques of remote sensing*. John Wiley & Sons, 2021.
- [14] J. M. Bioucas-Dias, A. Plaza, G. Camps-Valls, P. Scheunders, N. Nasrabadi, and J. Chanussot, “Hyperspectral remote sensing data analysis and future challenges,” *IEEE Geoscience and Remote Sensing Magazine*, vol. 1, no. 2, pp. 6–36, 2013.
- [15] H. Zhou, J. Sun, G. Turk, and J. M. Rehg, “Terrain synthesis from digital elevation models,” *IEEE transactions on visualization and computer graphics*, vol. 13, no. 4, pp. 834–848, 2007.
- [16] M. J. Khan, H. S. Khan, A. Yousaf, K. Khurshid, and A. Abbas, “Modern trends in hyperspectral image anal-

- 
- ysis: A review,” *IEEE Access*, vol. 6, pp. 14 118–14 129, 2018.
- [17] A. Almansa, F. Cao, Y. Gousseau, and B. Rougé, “Interpolation of digital elevation models using amle and related methods,” *IEEE transactions on geoscience and remote sensing*, vol. 40, no. 2, pp. 314–325, 2002.
- [18] J.-D. Génevaux, É. Galin, E. Guérin, A. Peytavie, and B. Benes, “Terrain generation using procedural models based on hydrology,” *ACM Transactions on Graphics (TOG)*, vol. 32, no. 4, pp. 1–13, 2013.
- [19] E. Galin, E. Guérin, A. Peytavie, G. Cordonnier, M.-P. Cani, B. Benes, and J. Gain, “A review of digital terrain modeling,” in *Computer Graphics Forum*, vol. 38, no. 2. Wiley Online Library, 2019, pp. 553–577.
- [20] S. Liu, D. Marinelli, L. Bruzzone, and F. Bovolo, “A review of change detection in multitemporal hyperspectral images: Current techniques, applications, and challenges,” *IEEE Geoscience and Remote Sensing Magazine*, vol. 7, no. 2, pp. 140–158, 2019.
- [21] P. Ghamisi, N. Yokoya, J. Li, W. Liao, S. Liu, J. Plaza, B. Rasti, and A. Plaza, “Advances in hyperspectral image and signal processing: A comprehensive overview of the state of the art,” *IEEE Geoscience and Remote Sensing Magazine*, vol. 5, no. 4, pp. 37–78, 2017.

- [22] P. C. Pandey, H. Balzter, P. K. Srivastava, G. P. Petropoulos, and B. Bhattacharya, “Future perspectives and challenges in hyperspectral remote sensing,” *Hyperspectral Remote Sensing*, pp. 429–439, 2020.
- [23] V. Chaplot, F. Darboux, H. Bourennane, S. Legu edois, N. Silvera, and K. Phachomphon, “Accuracy of interpolation techniques for the derivation of digital elevation models in relation to landform types and data density,” *Geomorphology*, vol. 77, no. 1-2, pp. 126–141, 2006.
- [24] D. Shen and Y. Sheng, “Area partitioning for channel network extraction using digital elevation models and remote sensing,” *IEEE Geoscience and Remote Sensing Letters*, vol. 9, no. 2, pp. 194–198, 2011.
- [25] J. A. Richards and J. A. Richards, *Remote Sensing Digital Image Analysis*. Berlin/Heidelberg, Germany: Springer, 2022, vol. 5.
- [26] P. Gamba, F. Tupin, and Q. Weng, “Introduction to the issue on remote sensing of human settlements: Status and challenges,” *IEEE Journal of Selected Topics in Applied Earth Observations and Remote Sensing*, vol. 1, no. 2, pp. 82–86, 2008.
- [27] F. Dell’Acqua, P. Gamba, A. Ferrari, J. Palmason, J. Benediktsson, and K. Arnason, “Exploiting spectral and spatial information in hyperspectral urban data with high resolution,” *IEEE Geoscience and Remote Sensing Letters*, vol. 1, no. 4, pp. 322–326, 2004.

- 
- [28] J. Li and R. Narayanan, “Integrated spectral and spatial information mining in remote sensing imagery,” *IEEE Transactions on Geoscience and Remote Sensing*, vol. 42, no. 3, pp. 673–685, 2004.
- [29] M. Datcu, K. Seidel, and M. Walessa, “Spatial information retrieval from remote-sensing images. i. information theoretical perspective,” *IEEE Transactions on Geoscience and Remote Sensing*, vol. 36, no. 5, pp. 1431–1445, 1998.
- [30] P. Duan, P. Ghamisi, X. Kang, B. Rasti, S. Li, and R. Gloaguen, “Fusion of dual spatial information for hyperspectral image classification,” *IEEE Transactions on Geoscience and Remote Sensing*, vol. 59, no. 9, pp. 7726–7738, 2021.
- [31] B. S. Daya Sagar, “Visualization of spatiotemporal behavior of discrete maps via generation of recursive median elements,” *IEEE Transactions on Pattern Analysis and Machine Intelligence*, vol. 32, no. 2, pp. 378–384, 2010.
- [32] B. Daya Sagar and J. Serra, “Spatial information retrieval, analysis, reasoning and modelling,” *International Journal of Remote Sensing*, vol. 31, no. 22, pp. 5747–5750, 2010.
- [33] T. Blaschke, “Object-based image analysis for remote sensing,” *ISPRS journal of photogrammetry and remote sensing*, vol. 65, no. 1, pp. 2–16, 2010.
- [34] G. Cheng, J. Han, and X. Lu, “Remote sensing image scene classification: Benchmark and state of the art,” *Pro-*

- ceedings of the IEEE*, vol. 105, no. 10, pp. 1865–1883, 2017.
- [35] B. C. Tso and P. M. Mather, “Classification of multisource remote sensing imagery using a genetic algorithm and markov random fields,” *IEEE Transactions on Geoscience and Remote Sensing*, vol. 37, no. 3, pp. 1255–1260, 1999.
- [36] J. Stuckens, P. Coppin, and M. Bauer, “Integrating contextual information with per-pixel classification for improved land cover classification,” *Remote Sensing of Environment*, vol. 71, no. 3, pp. 282–296, 2000.
- [37] “Accuracy assessment of contextual classification results for vegetation mapping,” *International Journal of Applied Earth Observation and Geoinformation*, vol. 15, pp. 7–15, 2012, special Issue on Geographic Object-based Image Analysis: GEOBIA.
- [38] R. M. Haralick, K. Shanmugam, and I. H. Dinstein, “Textural features for image classification,” *IEEE Transactions on systems, man, and cybernetics*, no. 6, pp. 610–621, 1973.
- [39] R. M. Haralick, “Statistical and structural approaches to texture,” *Proceedings of the IEEE*, vol. 67, no. 5, pp. 786–804, 1979.
- [40] A. Carleer and E. Wolff, “Urban land cover multi-level region-based classification of vhr data by selecting rele-

- 
- vant features,” *International Journal of Remote Sensing*, vol. 27, no. 6, pp. 1035–1051, 2006.
- [41] M. Tuceryan and A. K. Jain, “Texture segmentation using voronoi polygons,” *IEEE transactions on pattern analysis and machine intelligence*, vol. 12, no. 2, pp. 211–216, 1990.
- [42] A. Materka and M. Strzelecki, “Texture analysis methods a review, technical university of lodz, institute of electronics,” *COST, Brussels*, p. B11, 1998.
- [43] C. Coburn and A. C. Roberts, “A multiscale texture analysis procedure for improved forest stand classification,” *International journal of remote sensing*, vol. 25, no. 20, pp. 4287–4308, 2004.
- [44] N. Lam, “Description and measurement of landsat tm images using fractals,” *Photogrammetric engineering and remote sensing*, vol. 56, no. 2, pp. 187–195, 1990.
- [45] P. de Souza, “Texture recognition via autoregression,” *Pattern Recognition*, vol. 15, no. 6, pp. 471–475, 1982.
- [46] G. R. Cross and A. K. Jain, “Markov random field texture models,” *IEEE Transactions on Pattern Analysis and Machine Intelligence*, no. 1, pp. 25–39, 1983.
- [47] S. G. Mallat, “A theory for multiresolution signal decomposition: the wavelet representation,” *IEEE transactions on pattern analysis and machine intelligence*, vol. 11, no. 7, pp. 674–693, 1989.

- [48] J. Stuckens, P. Coppin, and M. Bauer, “Integrating contextual information with per-pixel classification for improved land cover classification,” *Remote sensing of environment*, vol. 71, no. 3, pp. 282–296, 2000.
- [49] G. Moser, S. B. Serpico, and J. A. Benediktsson, “Land-cover mapping by markov modeling of spatial–contextual information in very-high-resolution remote sensing images,” *Proceedings of the IEEE*, vol. 101, no. 3, pp. 631–651, 2012.
- [50] H. Shekarforoush, M. Berthod, J. Zerubia, and M. Werman, “Sub-pixel bayesian estimation of albedo and height,” *International Journal of Computer Vision*, vol. 19, pp. 289–300, 1996.
- [51] X. Jia and J. A. Richards, “Managing the spectral-spatial mix in context classification using markov random fields,” *IEEE Geoscience and Remote Sensing Letters*, vol. 5, no. 2, pp. 311–314, 2008.
- [52] M. Fauvel, J. A. Benediktsson, J. Chanussot, and J. R. Sveinsson, “Spectral and spatial classification of hyperspectral data using svms and morphological profiles,” *IEEE Transactions on Geoscience and Remote Sensing*, vol. 46, no. 11, pp. 3804–3814, 2008.
- [53] R. L. Kettig and D. Landgrebe, “Classification of multispectral image data by extraction and classification of homogeneous objects,” *IEEE Transactions on geoscience Electronics*, vol. 14, no. 1, pp. 19–26, 1976.



- 
- [54] B. Mannan and A. Ray, “Crisp and fuzzy competitive learning networks for supervised classification of multispectral IRS scenes,” *International Journal of Remote Sensing*, vol. 24, no. 17, pp. 3491–3502, 2003.
- [55] Q. Jackson and D. A. Landgrebe, “Adaptive bayesian contextual classification based on markov random fields,” *IEEE Transactions on Geoscience and Remote Sensing*, vol. 40, no. 11, pp. 2454–2463, 2002.
- [56] P. Salembier, A. Oliveras, and L. Garrido, “Antiextensive connected operators for image and sequence processing,” *IEEE Transactions on Image Processing*, vol. 7, no. 4, pp. 555–570, 1998.
- [57] M. Dalla Mura, A. Villa, J. A. Benediktsson, J. Chanussot, and L. Bruzzone, “Classification of hyperspectral images by using extended morphological attribute profiles and independent component analysis,” *IEEE Geoscience and Remote Sensing Letters*, vol. 8, no. 3, pp. 542–546, 2010.
- [58] G. Matheron, *Random Sets and Integral Geometry*. New York: Wiley, 1975.
- [59] J. Serra and P. Soille, *Mathematical morphology and its applications to image processing*. Springer Science & Business Media, 2012, vol. 2.
- [60] J. Serra, *Image Analysis and Mathematical Morphology*. London: Academic Press, 1982.

- [61] H. Hadwiger, *Vorlesungen Über Inhalt, Oberfläche und Isoperimetrie*. Berlin: Springer, 1957.
- [62] H. Minkowski, *Gesammelte Abhandlungen*. Leipzig: Teubner, 1911.
- [63] J. Serra, *Image Analysis and Mathematical Morphology: Vol.: 2: Theoretical Advances*. Academic Press, 1988.
- [64] S. R. Sternberg, “Grayscale morphology,” *Computer Vision, Graphics, and Image Processing*, vol. 35, no. 3, pp. 333–355, 1986.
- [65] C. Ronse, “Why mathematical morphology needs complete lattices,” *Signal Processing*, vol. 21, no. 2, pp. 129–154, 1990.
- [66] H. J. A. M. Heijmans, *Morphological Image Operators*. United Kingdom: Academic Press, 1994.
- [67] M. Nachtgael, P. Sussner, T. Mélangé, and E. Kerre, “On the role of complete lattices in mathematical morphology: From tool to uncertainty model,” *Information Sciences*, vol. 181, no. 10, pp. 1971–1988, 2011, special Issue on Information Engineering Applications Based on Lattices.
- [68] P. Sussner and M. Valle, “Classification of fuzzy mathematical morphologies based on concepts of inclusion measure and duality,” *Journal of Mathematical Imaging and Vision*, vol. 32, pp. 139–159, 10 2008.

- 
- [69] L. A. Zadeh, “Fuzzy sets,” *Information Control*, vol. 8, pp. 338–353, 1965.
- [70] E. K. Bernard DE Baets and M. Gupta, “The fundamentals of fuzzy mathematical morphology part 1: Basic concepts,” *International Journal of General Systems*, vol. 23, no. 2, pp. 155–171, 1995.
- [71] B. De Baets, E. E. Kerre, and M. M. Gupta, “Foundations of fuzzy mathematical morphology: Part 2: Idempotence, convexity, and decomposition,” *International Journal of General Systems*, vol. 23, pp. 307–322, 1995.
- [72] D. Sinha and E. R. Dougherty, “Fuzzy mathematical morphology,” *Journal of Visual Communication and Image Representation*, vol. 3, no. 3, pp. 286–302, 1992.
- [73] I. Bloch and H. Maitre, “Fuzzy mathematical morphologies: A comparative study,” *Pattern Recognition*, vol. 28, no. 9, pp. 1341–1387, 1995.
- [74] T.-Q. Deng and H. J. A. M. Heijmans, “Grey-scale morphology based on fuzzy logic,” *Journal of Mathematical Imaging and Vision*, vol. 16, 01 2002.
- [75] P. Sussner, M. Nachtegael, T. Mélange, J. Cousty, and D. Vandermeulen, “Interval-valued and intuitionistic fuzzy mathematical morphologies as special cases of l-fuzzy mathematical morphology,” *Journal of Mathematical Imaging and Vision*, vol. 43, no. 1, pp. 50–71, 2012.

- [76] I. Destival, “Mathematical morphology applied to remote sensing,” *Acta Astronautica*, vol. 13, no. 6-7, pp. 371–385, 1986.
- [77] G. J. Banon and J. Barrera, “Morphological filtering for stripping correction of spot images,” *Photogrammetria*, vol. 43, no. 3-4, pp. 195–205, 1989.
- [78] C. Martel, G. Flouzat, A. Souriau, and F. Safa, “A morphological method of geometric analysis of images: Application to the gravity anomalies in the indian ocean,” *Journal of Geophysical Research: Solid Earth*, vol. 94, no. B2, pp. 1715–1726, 1989.
- [79] J. J. Simpson, “Image masking using polygon fills and morphological transformations,” *Remote sensing of environment*, vol. 40, no. 3, pp. 161–183, 1992.
- [80] M. Pesaresi, A. Gerhardinger, and F. Kayitakire, “A robust built-up area presence index by anisotropic rotation-invariant textural measure,” *IEEE Journal of selected topics in applied earth observations and remote sensing*, vol. 1, no. 3, pp. 180–192, 2008.
- [81] J. Chou, R. Weger, J. Ligtenberg, K.-S. Kuo, R. Welch, and P. Breeden, “Segmentation of polar scenes using multi-spectral texture measures and morphological filtering,” *Remote Sensing*, vol. 15, no. 5, pp. 1019–1036, 1994.
- [82] S. M. Lea and M. Lybanon, “Automated boundary delineation in infrared ocean images,” *IEEE transactions on*

- 
- geoscience and remote sensing*, vol. 31, no. 6, pp. 1256–1260, 1993.
- [83] Y. Callot, C. Mering, and A. Simonin, “Image-analysis and cartography of sand hill massifs on high resolution images: application to the great western (nw of algerian sahara),” *International Journal of Remote Sensing*, vol. 15, no. 18, pp. 3799–3822, 1994.
- [84] C. Mering, Y. Callot, and A. Kemmouche, “Analysis and mapping of natural landscapes from satellite images using morphological filters,” *Microscopy Microanalysis Microstructures*, vol. 7, no. 5-6, pp. 323–330, 1996.
- [85] A. Watson, R. Vaughan, and M. Powell, “Classification using the watershed method,” *International Journal of Remote Sensing*, vol. 13, no. 10, pp. 1881–1890, 1992.
- [86] A. Watson, “A new method of classification for landsat data using the ‘watershed’ algorithm,” *Pattern Recognition Letters*, vol. 6, no. 1, pp. 15–19, 1987.
- [87] P. Soille, “Morphological partitioning of multispectral images,” *Journal of Electronic Imaging*, vol. 5, no. 3, pp. 252–265, 1996.
- [88] P. J. Soille and M. M. Ansault, “Automated basin delineation from digital elevation models using mathematical morphology,” *Signal Processing*, vol. 20, no. 2, pp. 171–182, 1990.

- [89] L. Vincent and P. Soille, “Watersheds in digital spaces: an efficient algorithm based on immersion simulations,” *IEEE Transactions on Pattern Analysis & Machine Intelligence*, vol. 13, no. 06, pp. 583–598, 1991.
- [90] P. Soille and L. M. Vincent, “Determining watersheds in digital pictures via flooding simulations,” in *Visual Communications and Image Processing’90: Fifth in a Series*, vol. 1360. SPIE, 1990, pp. 240–250.
- [91] P. Soille, “Spatial distributions from contour lines: an efficient methodology based on distance transformations,” *Journal of Visual Communication and Image Representation*, vol. 2, no. 2, pp. 138–150, 1991.
- [92] ———, “Generalized geodesy via geodesic time,” *Pattern Recognition Letters*, vol. 15, no. 12, pp. 1235–1240, 1994.
- [93] P. Soille and C. Gratin, “An efficient algorithm for drainage network extraction on dems,” *Journal of Visual Communication and Image Representation*, vol. 5, no. 2, pp. 181–189, 1994.
- [94] P. Soille, “Processing of digital elevation maps,” *Handbook of Computer Vision and Applications*, vol. 3, pp. 411–428, 1999.
- [95] P. Soille and M. Pesaresi, “Advances in mathematical morphology applied to geoscience and remote sensing,” *IEEE Transactions on Geoscience and Remote Sensing*, vol. 40, no. 9, pp. 2042–2055, 2002.

- 
- [96] L. Najman and H. Talbot, *Mathematical morphology: from theory to applications*. Hoboken, NJ: John Wiley & Sons, 2013.
- [97] J. Serra, “Mathematical morphology,” in *Encyclopedia of Mathematical Geosciences*. Springer, 2022, pp. 1–16.
- [98] R. M. Haralick, S. R. Sternberg, and X. Zhuang, “Image analysis using mathematical morphology,” *IEEE transactions on pattern analysis and machine intelligence*, no. 4, pp. 532–550, 1987.
- [99] P. Soille, *Morphological Image Analysis: Principles and Applications*. Berlin: Springer, 1999, vol. 2, no. 3.
- [100] M. Dalla Mura, J. A. Benediktsson, J. Chanussot, and L. Bruzzone, “The evolution of the morphological profile: From panchromatic to hyperspectral images,” *Optical remote sensing: advances in signal processing and exploitation techniques*, pp. 123–146, 2011.
- [101] M. Pesaresi and J. A. Benediktsson, “A new approach for the morphological segmentation of high-resolution satellite imagery,” *IEEE transactions on Geoscience and Remote Sensing*, vol. 39, no. 2, pp. 309–320, 2001.
- [102] S. V. Stehman, “Selecting and interpreting measures of thematic classification accuracy,” *Remote sensing of Environment*, vol. 62, no. 1, pp. 77–89, 1997.
- [103] F. Luo, L. Zhang, B. Du, and L. Zhang, “Dimensionality reduction with enhanced hybrid-graph discriminant learn-

- ing for hyperspectral image classification,” *IEEE Transactions on Geoscience and Remote Sensing*, vol. 58, no. 8, pp. 5336–5353, 2020.
- [104] A. A. Taha, A. Hanbury, and O. A. J. del Toro, “A formal method for selecting evaluation metrics for image segmentation,” in *2014 IEEE international conference on image processing (ICIP)*. IEEE, 2014, pp. 932–936.
- [105] H. Deborah, N. Richard, and J. Y. Hardeberg, “A comprehensive evaluation of spectral distance functions and metrics for hyperspectral image processing,” *IEEE Journal of Selected Topics in Applied Earth Observations and Remote Sensing*, vol. 8, no. 6, pp. 3224–3234, 2015.
- [106] S. Aronoff *et al.*, “Classification accuracy: a user approach,” *Photogrammetric Engineering and Remote Sensing*, vol. 48, no. 8, pp. 1299–1307, 1982.
- [107] S. M. Vieira, U. Kaymak, and J. M. C. Sousa, “Cohen’s kappa coefficient as a performance measure for feature selection,” in *International Conference on Fuzzy Systems*, 2010, pp. 1–8.
- [108] J. Cohen, “A coefficient of agreement for nominal scales,” *Educational and psychological measurement*, vol. 20, no. 1, pp. 37–46, 1960.
- [109] M. Hu, C. Wu, B. Du, and L. Zhang, “Binary change guided hyperspectral multiclass change detection,” *IEEE*



---

*Transactions on Image Processing*, vol. 32, pp. 791–806, 2023.

- [110] N. A. Mahmon, N. Ya’acob, and A. L. Yusof, “Differences of image classification techniques for land use and land cover classification,” in *2015 IEEE 11th International Colloquium on Signal Processing & Its Applications (CSPA)*. IEEE, 2015, pp. 90–94.
- [111] S. Jog and M. Dixit, “Supervised classification of satellite images,” in *2016 Conference on Advances in Signal Processing (CASP)*. IEEE, 2016, pp. 93–98.
- [112] C. N. Kroll and J. R. Stedinger, “Estimation of moments and quantiles using censored data,” *Water Resources Research*, vol. 32, no. 4, pp. 1005–1012, 1996.
- [113] R. Rinehart and E. J. Coleman, “Digital elevation models produced from digital line graphs,” in *Proceedings of the ACSM-ASPRS Annual Convention*, vol. 2, 1988, pp. 291–299.
- [114] B. L. Bowerman, R. T. O’Connell, and A. B. Koehler, *Forecasting, Time Series, and Regression: An Applied Approach*. Belmont, CA: Thomson Brooks/Cole, 2005.
- [115] Y. Gyasi-Agyei, G. Willgoose, and F. P. De Troch, “Effects of vertical resolution and map scale of digital elevation models on geomorphological parameters used in hydrology,” *Hydrological Processes*, vol. 9, no. 3-4, pp. 363–382, 1995.

- [116] K. Mackay, D. Bernstein, B. Glocker, K. Kamnitsas, and A. Taylor, “A review of the metrics used to assess auto-contouring systems in radiotherapy,” *Clinical Oncology*, 2023.
- [117] A. F. Goetz, “Three decades of hyperspectral remote sensing of the earth: A personal view,” *Remote sensing of environment*, vol. 113, pp. S5–S16, 2009.
- [118] D. Manolakis and G. Shaw, “Detection algorithms for hyperspectral imaging applications,” *IEEE signal processing magazine*, vol. 19, no. 1, pp. 29–43, 2002.
- [119] K. Turpie, S. Veraverbeke, R. Wright, M. Anderson, A. Prakash, and D. Quattrochi, “Nasa 2014 the hyperspectral infrared imager (hyspirci)-science impact of deploying instruments on separate platforms,” Tech. Rep., 2014.
- [120] J. Richards and X. Jia, “Remote sensing digital image analysis. berlin,” *Springer*, vol. 78, p. 193, 2006.
- [121] A. A. Green, M. Berman, P. Switzer, and M. D. Craig, “A transformation for ordering multispectral data in terms of image quality with implications for noise removal,” *IEEE Transactions on geoscience and remote sensing*, vol. 26, no. 1, pp. 65–74, 1988.
- [122] S. K. Roy, S. Das, T. Song, and B. Chanda, “Darecnet-bs: Unsupervised dual-attention reconstruction network for hyperspectral band selection,” *IEEE Geoscience and*

---

*Remote Sensing Letters*, vol. 18, no. 12, pp. 2152–2156, 2020.

- [123] Z. Dou, K. Gao, X. Zhang, H. Wang, and L. Han, “Band selection of hyperspectral images using attention-based autoencoders,” *IEEE Geoscience and Remote Sensing Letters*, vol. 18, no. 1, pp. 147–151, 2020.
- [124] L. Ji, L. Zhu, L. Wang, Y. Xi, K. Yu, and X. Geng, “Fastvgbs: A fast version of the volume-gradient-based band selection method for hyperspectral imagery,” *IEEE Geoscience and Remote Sensing Letters*, vol. 18, no. 3, pp. 514–517, 2020.
- [125] M. Song, C. Yu, H. Xie, and C.-I. Chang, “Progressive band selection processing of hyperspectral image classification,” *IEEE Geoscience and Remote Sensing Letters*, vol. 17, no. 10, pp. 1762–1766, 2019.
- [126] L. Zhao, Y. Zeng, P. Liu, and X. Su, “Band selection with the explanatory gradient saliency maps of convolutional neural networks,” *IEEE Geoscience and Remote Sensing Letters*, vol. 17, no. 12, pp. 2105–2109, 2020.
- [127] W. Sun and Q. Du, “Hyperspectral band selection: A review,” *IEEE Geoscience and Remote Sensing Magazine*, vol. 7, no. 2, pp. 118–139, 2019.
- [128] Q. Wang, F. Zhang, and X. Li, “Hyperspectral band selection via optimal neighborhood reconstruction,” *IEEE*

- Transactions on Geoscience and Remote Sensing*, vol. 58, no. 12, pp. 8465–8476, 2020.
- [129] B. D. Sagar and S. L. Lim, “Ranks for pairs of spatial fields via metric based on grayscale morphological distances,” *IEEE Transactions on Image Processing*, vol. 24, no. 3, pp. 908–918, 2015.
- [130] M. J. Thurley and V. Danell, “Fast morphological image processing open-source extensions for gpu processing with cuda,” *IEEE journal of selected topics in signal processing*, vol. 6, no. 7, pp. 849–855, 2012.
- [131] J. Shi and J. Malik, “Normalized cuts and image segmentation,” *IEEE Transactions on Pattern Analysis and Machine Intelligence*, vol. 22, no. 8, pp. 888–905, 2000.
- [132] A. Y. Ng, M. I. Jordan, and Y. Weiss, “On spectral clustering: analysis and an algorithm,” in *Proceedings of the 14th International Conference on Neural Information Processing Systems: Natural and Synthetic*, ser. NIPS’01. Cambridge, MA, USA: MIT Press, 2001, p. 849–856.
- [133] U. von Luxburg, “A tutorial on spectral clustering,” *Statistics and Computing*, vol. 17, pp. 395–416, 2007.
- [134] “Hyperspectral remote sensing scenes,” [https://www.ehu.eus/ccwintco/index.php/Hyperspectral\\_Remote\\_Sensing\\_Scenes](https://www.ehu.eus/ccwintco/index.php/Hyperspectral_Remote_Sensing_Scenes).
- [135] C. Cortes and V. Vapnik, “Support-vector networks,” *Machine learning*, vol. 20, pp. 273–297, 1995.

- 
- [136] C.-I. Chang, Q. Du, T.-L. Sun, and M. L. Althouse, “A joint band prioritization and band-decorrelation approach to band selection for hyperspectral image classification,” *IEEE transactions on geoscience and remote sensing*, vol. 37, no. 6, pp. 2631–2641, 1999.
- [137] A. Martínez-Usó Martínez-Usó, F. Pla, J. M. Sotoca, and P. García-Sevilla, “Clustering-based hyperspectral band selection using information measures,” *IEEE Transactions on Geoscience and Remote Sensing*, vol. 45, no. 12, pp. 4158–4171, 2007.
- [138] W. Sun, L. Zhang, B. Du, W. Li, and Y. M. Lai, “Band selection using improved sparse subspace clustering for hyperspectral imagery classification,” *IEEE Journal of Selected Topics in Applied Earth Observations and Remote Sensing*, vol. 8, no. 6, pp. 2784–2797, 2015.
- [139] H. Sun, J. Ren, H. Zhao, G. Sun, W. Liao, Z. Fang, and J. Zabalza, “Adaptive distance-based band hierarchy (adbh) for effective hyperspectral band selection,” *IEEE transactions on cybernetics*, vol. 52, no. 1, pp. 215–227, 2020.
- [140] W. Sun, J. Peng, G. Yang, and Q. Du, “Fast and latent low-rank subspace clustering for hyperspectral band selection,” *IEEE Transactions on Geoscience and Remote Sensing*, vol. 58, no. 6, pp. 3906–3915, 2020.

- [141] B. Daya Sagar, “Digital elevation models: An important source of data for geoscientists,” *IEEE Geoscience and Remote Sensing Magazine*, vol. 8, no. 4, pp. 138–142, 2020.
- [142] R. A. Hind Taud, Jean-François Parrot, “Dem generation by contour line dilation,” *Computers Geosciences*, vol. 25, no. 7, pp. 775–783, 1999.
- [143] A. Nelson, H. Reuter, and P. Gessler, “Dem production methods and sources,” *Developments in soil science*, vol. 33, pp. 65–85, 2009.
- [144] A. Cuartero, A. Felicísimo, and F. Ariza, “Accuracy, reliability, and depuration of spot hrv and terra aster digital elevation models,” *IEEE Transactions on Geoscience and Remote Sensing*, vol. 43, no. 2, pp. 404–407, 2005.
- [145] J. Chai, T. Miyoshi, and E. Nakamae, “Contour interpolation and surface reconstruction of smooth terrain models,” in *Proceedings Visualization’98*. IEEE, 1998, pp. 27–33.
- [146] P. V. Arun, “A comparative analysis of different dem interpolation methods,” *The Egyptian Journal of Remote Sensing and Space Science*, vol. 16, no. 2, pp. 133–139, 2013.
- [147] I. Florinsky, “Digital terrain modeling: A brief historical overview,” *Digital Terrain Analysis in Soil Science and Geology*, Elsevier, Amsterdam, vol. 14, 2012.
- [148] S. Erdogan, “A comparison of interpolation methods for producing digital elevation models at the field scale,”

---

*Earth surface processes and landforms*, vol. 34, no. 3, pp. 366–376, 2009.

- [149] A. Carrara, G. Bitelli, and R. Carla, “Comparison of techniques for generating digital terrain models from contour lines,” *International Journal of Geographical Information Science*, vol. 11, no. 5, pp. 451–473, 1997.
- [150] C. M. Gold, “Surface interpolation, spatial adjacency and gis,” in *Three dimensional applications in GIS*. CRC Press, 2020, pp. 21–35.
- [151] D. Watson, *Contouring: a guide to the analysis and display of spatial data*. UK: Elsevier, 2013.
- [152] S. Aronoff, “Geographic information systems: a management perspective,” *Geocarto International*, vol. 4, no. 4, pp. 58–58, 1989.
- [153] Z. Li, “A comparative study of the accuracy of digital terrain models (dtms) based on various data models,” *ISPRS Journal of Photogrammetry and Remote Sensing*, vol. 49, no. 1, pp. 2–11, 1994.
- [154] P. J. Pizor, “Principles of geographical information systems for land resources assessment.” *Soil Science*, vol. 144, no. 4, p. 306, 1987.
- [155] H. Taud, J.-F. Parrot, and R. Alvarez, “Dem generation by contour line dilation,” *Computers & geosciences*, vol. 25, no. 7, pp. 775–783, 1999.

- [156] B. D. Sagar and S. L. Lim, “Morphing of grayscale dems via morphological interpolations,” *IEEE Journal of Selected Topics in Applied Earth Observations and Remote Sensing*, vol. 8, no. 11, pp. 5190–5198, 2015.
- [157] J. Grazzini and P. Soille, “Improved morphological interpolation of elevation contour data with generalised geodesic propagations,” in *International Conference on Computer Analysis of Images and Patterns*. Springer, 2007, pp. 742–750.
- [158] S. P. Morse, “A mathematical model for the analysis of contour-line data,” *Journal of the ACM (JACM)*, vol. 15, no. 2, pp. 205–220, 1968.
- [159] T. Hahmann and E. L. Uesry, “What is in a contour map? a region-based logical formalization of contour semantics,” in *Spatial Information Theory: 12th International Conference, COSIT 2015, Santa Fe, NM, USA, October 12-16, 2015, Proceedings 12*. Springer, 2015, pp. 375–399.
- [160] J. Serra, “Hausdorff distances and interpolations,” *Computational Imaging and Vision*, vol. 12, pp. 107–114, 1998.
- [161] P. Maragos and R. D. Ziff, “Threshold superposition in morphological image analysis systems,” *IEEE Transactions on Pattern Analysis and Machine Intelligence*, vol. 12, no. 5, pp. 498–504, 1990.
- [162] T. H. Cormen, C. E. Leiserson, R. L. Rivest, and C. Stein, *Introduction to Algorithms*, 3rd ed. The MIT Press, 2009.



- 
- [163] “Earth explorer interface and product documentation and explorer,” <https://earthexplorer.usgs.gov/>.
- [164] QGIS Development Team, “Qgis geographic information system,” <http://qgis.osgeo.org>, 2009.
- [165] M. A. OLIVER and R. WEBSTER, “Kriging: a method of interpolation for geographical information systems,” *International journal of geographical information systems*, vol. 4, no. 3, pp. 313–332, 1990.
- [166] N. Cressie, “The origins of kriging,” *Mathematical Geology*, vol. 22, pp. 239–252, 1990.
- [167] A. S. Fotheringham and M. E. O’Kelly, *Spatial interaction models: formulations and applications*. Kluwer Academic Publishers Dordrecht, 1989, vol. 1.
- [168] M. Hutchinson, “Calculation of hydrologically sound digital elevation models,” *Third International Symposium on Spatial Data Handling*, pp. 117–133, 01 1988.
- [169] M. F. Hutchinson, “A new procedure for gridding elevation and stream line data with automatic removal of spurious pits,” *Journal of Hydrology*, vol. 106, no. 3-4, pp. 211–232, 1989.
- [170] P. Maragos, “Lattice image processing: A unification of morphological and fuzzy algebraic systems,” *Journal of Mathematical Imaging and Vision*, vol. 22, pp. 333–353, 05 2005.

- [171] V. Barnett, “The ordering of multivariate data,” *Journal of the Royal Statistical Society: Series A (General)*, vol. 139, no. 3, pp. 318–344, 1976.
- [172] D. Titterton, “Estimation of correlation coefficients by ellipsoidal trimming,” *Journal of the Royal Statistical Society: Series C (Applied Statistics)*, vol. 27, no. 3, pp. 227–234, 1978.
- [173] J. Li and Y. Li, “Multivariate mathematical morphology based on principal component analysis: initial results in building extraction,” in *Proceedings of the 20th ISPRS*, vol. 35, 2004.
- [174] E. Aptoula and S. Lefèvre, “On lexicographical ordering in multivariate mathematical morphology,” *Pattern Recognition Letters*, vol. 29, no. 2, pp. 109–118, 2008.
- [175] —, “A comparative study on multivariate mathematical morphology,” *Pattern Recognition*, vol. 40, no. 11, pp. 2914–2929, 2007.
- [176] J. Angulo, “Morphological colour operators in totally ordered lattices based on distances: Application to image filtering, enhancement and analysis,” *Computer vision and image understanding*, vol. 107, no. 1-2, pp. 56–73, 2007.
- [177] —, “Morphological color processing based on distances. application to color denoising and enhancement by centre and contrast operators,” in *Proceedings of the VIIP*, September 2005, pp. 314–319.

- 
- [178] E. Aptoula and S. Lefevre, “Pseudo multivariate morphological operators based on  $\alpha$ -trimmed lexicographical extrema,” in *2007 5th International Symposium on Image and Signal Processing and Analysis*. IEEE, 2007, pp. 367–372.
- [179] E. Aptoula and S. Lefèvre, “ $\alpha$ -trimmed lexicographical extrema for pseudo-morphological image analysis,” *Journal of Visual Communication and Image Representation*, vol. 19, no. 3, pp. 165–174, 2008.
- [180] J. Angulo, “Geometric algebra colour image representations and derived total orderings for morphological operators—part i: Colour quaternions,” *Journal of Visual Communication and Image Representation*, vol. 21, no. 1, pp. 33–48, 2010.
- [181] C.-J. Z. X.-H. Gao and X.-Y. Hu, “An adaptive lexicographical ordering of color mathematical morphology,” *Journal of Computers*, vol. 24, no. 3, 2013.
- [182] T. Lei, Y. Fan, C. Zhang, and X. Wang, “Vector mathematical morphological operators based on fuzzy extremum estimation,” in *2013 IEEE International Conference on Image Processing*. IEEE, 2013, pp. 3031–3034.
- [183] G. Franchi and J. Angulo, “Ordering on the probability simplex of endmembers for hyperspectral morphological image processing,” in *Mathematical Morphology and Its Applications to Signal and Image Processing: Proceedings*

- of the 12th International Symposium on Mathematical Morphology (ISMM 2015)*. Reykjavik, Iceland: Springer, 2015, pp. 410–421.
- [184] O. Lezoray, A. Elmoataz, and C. Meurie, “Mathematical morphology in any color space,” in *14th International Conference of Image Analysis and Processing-Workshops (ICIAPW 2007)*. IEEE, 2007, pp. 183–187.
- [185] S. Velasco-Forero and J. Angulo, “Supervised ordering in  $\mathbb{r}^p$ : Application to morphological processing of hyperspectral images,” *IEEE Transactions on Image Processing*, vol. 20, no. 11, pp. 3301–3308, 2011.
- [186] —, “Random projection depth for multivariate mathematical morphology,” *IEEE Journal of Selected Topics in Signal Processing*, vol. 6, no. 7, pp. 753–763, 2012.
- [187] E. Aptoula, N. Courty, and S. Lefèvre, “An end-member based ordering relation for the morphological description of hyperspectral images,” in *2014 IEEE International Conference on Image Processing (ICIP)*. IEEE, 2014, pp. 5097–5101.
- [188] S. Velasco-Forero and J. Angulo, “Vector ordering and multispectral morphological image processing,” *Advances in low-level color image processing*, pp. 223–239, 2014.
- [189] A. Garcia, C. Vachier, and J.-P. Vallée, “Multivariate mathematical morphology and bayesian classifier application to colour and medical images,” in *Image Processing:*

---

*Algorithms and Systems VI*, vol. 6812. SPIE, 2008, pp. 22–32.

- [190] M. Sangalli and M. E. Valle, “Approaches to multivalued mathematical morphology based on uncertain reduced orderings,” in *International Symposium on Mathematical Morphology and Its Applications to Signal and Image Processing*. Springer, 2019, pp. 228–240.
- [191] A. Plaza, P. Martinez, R. Perez, and J. Plaza, “A new approach to mixed pixel classification of hyperspectral imagery based on extended morphological profiles,” *Pattern Recognition*, vol. 37, no. 6, pp. 1097–1116, 2004.
- [192] J. Plaza, A. J. Plaza, and C. Barra, “Multi-channel morphological profiles for classification of hyperspectral images using support vector machines,” *Sensors*, vol. 9, no. 1, pp. 196–218, 2009.
- [193] H. M. Al-Otum, “Morphological operators for color image processing based on mahalanobis distance measure,” *Optical Engineering*, vol. 42, no. 9, pp. 2595–2606, 2003.